

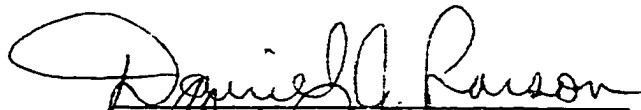

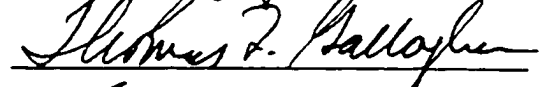
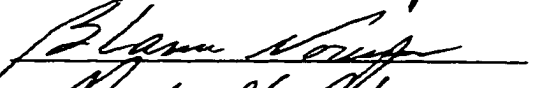
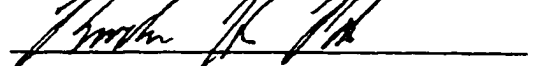
Non-Exponential Decay of Shock-Wavepackets

Jeffrey Edwin Thoma
Springfield, Pennsylvania

H. B. S., University of Delaware, 1991

A Dissertation Presented to the Graduate
Faculty of the University of Virginia
in Candidacy for the Degree of
Doctor of Philosophy

Department of Physics
University of Virginia
May, 1999

UMI Number: 9935069

UMI Microform 9935069
Copyright 1999, by UMI Company. All rights reserved.

**This microform edition is protected against unauthorized
copying under Title 17, United States Code.**

UMI
300 North Zeeb Road
Ann Arbor, MI 48103

Abstract

Short-pulse isolated core excitation (ICE) techniques have been used to create and observe autoionizing *shock-wavepackets*. Their dramatic, non-exponential, stair-step decay has been recorded, and is found to be well described by the formalism of Wang and Cooke [1].

Calcium atoms in a thermal beam are excited from their $4s^2$ ground state to an intermediate $4s\ 4p$ state using a Hansch-style dye laser ($\lambda = 423nm$). A second, similar dye laser ($\lambda = 393nm$) promotes the $4p$ electron to a highly excited Rydberg state ($25 \leq n \leq 32$). Both nsec dye lasers have a sufficiently narrow band-width to ensure that the Rydberg electron is in a single- n eigenstate.

The shock-wavepacket is produced by a short-pulse ICE on resonance with the $4s\ nd \rightarrow 4p\ nd$ transition ($\lambda \cong 393nm$). The short duration of this pulse ($FWHM \leq 0.25ps$) as compared to the Kepler period of the Rydberg electron ($2ps \leq T_K \leq 5ps$ depending on n), results in the creation of a shock wave front within the wavepacket. This shock front is a localized depletion of probability executing cyclical, radial excursions. Starting near the core, the wave front propagates through the radial wavepacket with a period equal to the Kepler period of the initial Rydberg state – “consuming” probability as it goes. After each orbit, the wavepacket resembles its original form, but with its overall amplitude greatly reduced. The periodic nature of this process is

manifested in the decay rate of the shock-wavepacket as a series of *stair-steps*.

A second ICE ($\lambda \cong 318nm$), employed in a pump-probe fashion with the first, is used to measure the survival probability of the shock-wavepacket as a function of time. The observed decay is demonstratively non-exponential, and the predicted *stair-steps* are clearly present in the rate.

[1] Xiao Wang and W. E. Cooke, Phys. Rev. A **67**, 976 (1991).

Acknowledgments

Having finished this chapter of my life, there are many people I wish to thank before turning to the next page. To begin with, I would like to thank my parents, Edwin and Barbara Thoma, for their constant love, encouragement, and support. None of this would have been possible without them.

Next, I would like to thank all of my teachers who encouraged me to think, to dream, and to see how far I could go: Nancy Bergrey, Joe Zumpano, Sharon Taylor, and Maurice Barnhill

Most of my time at Virginia has been spent in the company of Jeff Emmert, Chris Ingram, Karla Hagan-Ingram, Steve Apsel, and Biff Lyons. I'd like to thank them all for their friendship, companionship, and general moral support. This goes especially for Jeff, who also had to put up with me as a roommate, and for Chris, who spent upwards of ten hours a day with me when we were working in the same lab.

There are several people on staff here at the Physics Department who consistently helped to make things go smoothly for me. Suzie Garrett, Sibyl Hale, Bobby Floyd, Teresa Marshall, Tammie Shifflet, Bryan Wright, Jim Shea, Harvey Sugarman, and Faye Safley – thank you all.

The fact that I have managed to graduate with both the lab equipment and my eyesight intact I owe entirely to Matt Campbell. He spent a lot of time getting me up to speed with the general workings and layout of the lab. I am very much in his debt – all the more so for his proofreading of my dissertation.

Laura Wells deserves a lot of thanks for reading my dissertation with an eye towards grammar. Any errors still existing are entirely mine.

I would like to thank Dan Larson for giving me the time and freedom to explore, learn, and grow around the lab. His door was always open, and his suggestions always helpful. He has been an outstanding teacher, mentor, and friend.

Finally, I would like to thank Bob Jones for giving me the opportunity to participate in a very elegant and interesting experiment. Bob is a very talented experimentalist, and it is really amazing to watch him work. He spent a great deal of time teaching me the subtleties of this experiment, and very patiently answered all of my questions.

Table of Contents

Introduction	Shock-Wavepackets and Non-exponential Decay	1
Chapter 1	The Hydrogenic Atom	7
1.1	The Classical Hydrogenic Atom	8
1.1.1	The Equations of Motion	9
1.1.2	Bound State Motion	11
1.2	The Quantum Mechanical Hydrogenic Atom	16
Chapter 2	Rydberg Atoms and Autoionization	28
2.1	Rydberg Atoms – the Physical Framework for MQDT	29
2.2	Interacting Rydberg Series and Autoionizing States	36
2.3	Multi-channel Quantum Defect Theory	41
Chapter 3	Experimental Methods and Apparatus	57
3.1	Vacuum Chamber	65
3.2	Oven	66
3.3	Interaction Region	67
3.4	Data Acquisition	72
3.5	Dye Lasers	73
3.6	Argon-Ion Laser	75
3.7	Ti-sapphire Laser	76
3.8	Pulse Expander/Compressor	78
3.9	Regenerative Amplifier	81
3.10	Multipass Amplifier	82
3.11	Optical Parametric Amplifier	83
3.12	YAG	85
3.13	General Lab Environment	87
3.13.1	Optics Tables	87
3.13.2	Air Temperature	88
3.13.3	Chilled Water Cooling System	89

Chapter 4	Shock-Wavepackets	91
Chapter 5	Results and Analysis	98
5.1	Scaling of SWP Data	111
Chapter 6	Shock-Wavepackets: Another Point of View	121
6.1	The Wavepacket Approach	121
6.2	Stair-step Decay and Overlapping Resonances	132
Chapter 7	Conclusions	138
Appendix 1	Atomic Units and the Scaling of the TDSE	145
Appendix 2	Rydberg Wavefunctions	149
A2.1	Numerov Method -- Numerical Wavefunctions	149
A2.1.1	Numerov Routines	153

Introduction

Shock-Wavepackets and Non-exponential Decay

The 1976 edition of *Webster's New Collegiate Dictionary* defines Physics as "a science that deals with matter and energy and their interactions in the fields of mechanics, acoustics, optics, heat, electricity, magnetism, radiation, atomic structure and nuclear phenomena." At a more fundamental level however, Physics can be thought of as a science that deals with systematic approaches to solving problems. One particular approach which often proves useful is to decompose complex problems into a series of smaller, more manageable components. The relatively new field of quantum control (the application of one or more lasers to influence or generate a specific atomic, chemical, or molecular process more efficiently and/or precisely than would naturally occur [41]) is exactly the type of "complex problem" that benefits from this sort of decomposition. In order for quantum control to be effective, one must first understand the temporal dynamics of multi-electron atoms and

molecules interacting with sequentially applied lasers. The work presented in this thesis is one step towards gaining this understanding.

In our laboratory, we have studied the temporal evolution and decay of electron wavepackets produced from Calcium atoms under the influence of several nanosecond and femtosecond lasers. The experiments were undertaken to test and explore a theoretical proposal by Cooke and Wang that such a wavepacket -- produced from highly excited, two-electron atomic states -- would decay in time through a dramatic series of "stair steps" in its rate.[1]

Although the underlying mathematical description is somewhat complex, their basic argument was encapsulated in a series of illustrations which we have reproduced below in Figure (I.1). Simply put, the temporal evolution of the wave packet would be governed by the Fourier transform of the product of two terms. The individual transforms of these terms were easily computed and understood in the limit of very highly excited (Large- n) atomic states. The convolution theorem could then be applied to complete the calculation.

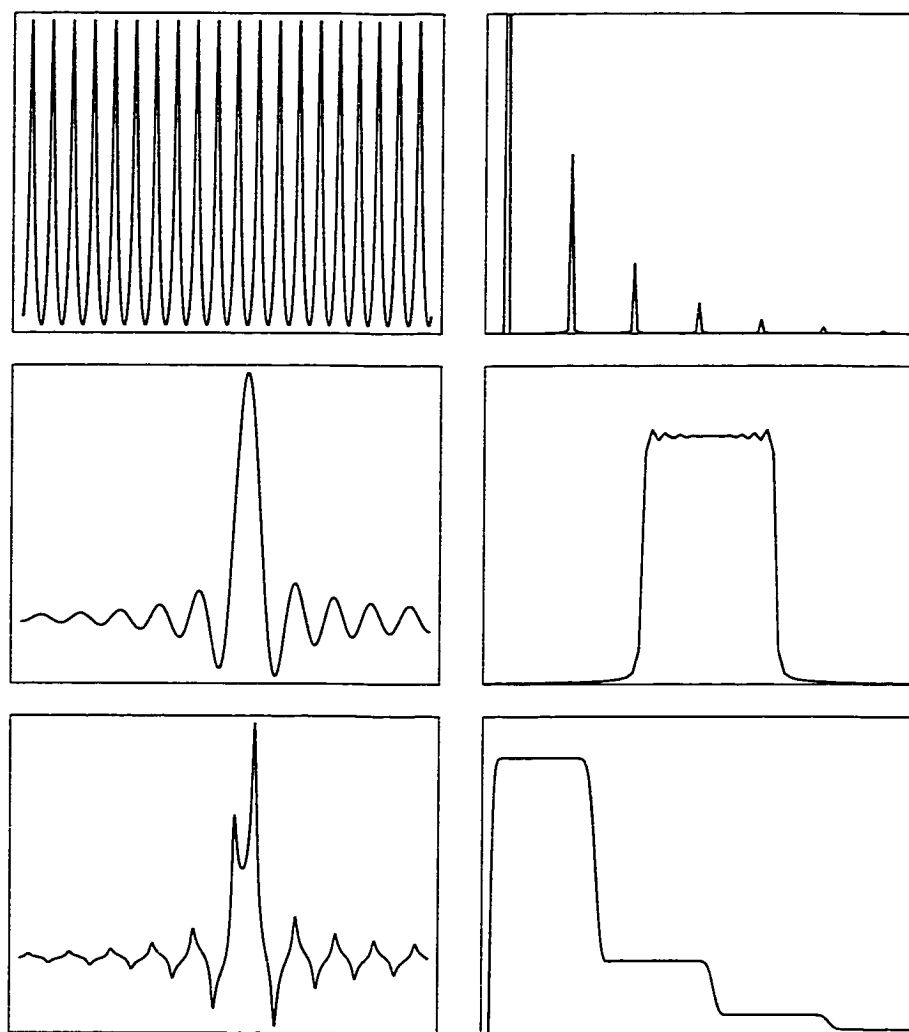


Figure I.1

Functions and their Fourier transforms in the Large- n limit. Each function on the right is the Fourier Transform of the function to its left. The function in the lower left corner is the product of the two above it. The stair-step decay of a Shock-wavepacket (lower right) can be calculated either as the Large- n Fourier Transform of this function, or as the convolution of the two functions above it. The stair-steps are more easily understood if one takes the later approach.

The first term is simply a series of spikes -- a set of resonances describing interactions between a highly excited valence electron and a second electron in a lower lying state. The Fourier transform of this term is determined to be a series of narrow spikes with exponentially

decreasing amplitudes. This term and its transform are the upper two plots in Figure I.1.

The second term is very much like the Sinc function often found in describing interference phenomena, and it describes how the different highly excited states of the atom relate to each other. The Fourier transform of this term is well known to be a step function -- a square pulse of finite amplitude and duration. This second transform pair are the middle plots of Figure I.1.

The convolution of two functions is a way of combining them that qualitatively "folds" them together such that the resulting "child" function inherits some of the traits of each of its "parents". In the bottom right-hand plot of Figure I.1, we have plotted the stair-step decay predicted by Cooke and Wang. Each stair-step has a width "inherited" from the unit step and an amplitude from the decreasing series of spikes. While the stair-step decay can be calculated directly by Fourier transforming the function in the lower left-hand plot, it is more easily understood using this convolution method.

It is also possible, and quite useful, to think of this process in terms of a "solar system" atom with "planetary" electrons. Imagine our solar system, but with only two planets : Mars (the inner electron) and Pluto

(the outer electron). After a very sudden explosion, Mars "jumps" into a new, larger orbit. This new orbit takes it into the path of Pluto. A collision ensues, with Mars returning to a lower orbit, and Pluto scattering off into the cosmos.

We can push this simple, classical picture towards the quantum regime if we replace our planets by highly elliptical asteroid belts. This replacement underscores the quantum mechanical idea that an electron, rather than occupying a definite position in space, is instead described by a probability distribution spread out over all space. Initially, all of the asteroids in the inner belt are much closer to the sun than those in the outer. The two belts overlap and begin to interact only after the aforementioned sudden explosion.

In this picture, the surprising stair-steps are easily understood -- at least qualitatively. Focus on a particular cross-sectional "slice" of the outer belt, imagining the asteroids as being uniformly distributed throughout the slice. The asteroid belts only intersect near the sun, so all of the scattering occurs in this region. As our slice passes through the scattering region, the number of asteroids it contains is drastically reduced. After a complete orbital period, *every* slice in the belt has been similarly depleted. It should be clear that in such a simple scattering picture as this, the rate at which asteroids leave the belt is directly

proportional to the number of asteroids in each slice. Hence, when the first "reduced" slice returns to the scattering region, the rate of scattering is also reduced. But this is exactly the stair-step decay of Wang and Cooke -- the rate is constant over each period, with each orbit exhibiting a decrease in amplitude.

The rest of this work proceeds as follows. In Chapter 1, we present an introduction to some of the underlying pictures and mathematical foundations of Atomic Physics as it applies to this problem. Chapter 2 builds on these foundations to develop a physical and mathematical description of Rydberg Atoms and the process of autoionization. Chapter 3 provides a sketch of our experimental procedure and an in-depth description of our apparatus. In Chapter 4, a quantitative framework (analogous to the qualitative arguments presented above) is established to better describe and analyze our data. The results of our experiments are conveyed in Chapter 5 and compared with our theoretical models. Finally, in Chapters 6 we examine the entire process from another perspective in order to better describe the physics involved.

Chapter 1

The Hydrogenic Atom

Just as our work on Shock-Wavepackets is a building block towards understanding the temporal dynamics of quantum control, modeling the Hydrogenic Atom is a building block towards understanding all of Atomic Physics. This is evident at all levels – from the most sophisticated: the self-consistent Hartree-Fock method[2] for describing non-hydrogenic, multi-electron atoms in "hydrogenish" terms – to the most fundamental: Atomic Units are defined so that the simplest properties of the Hydrogen Atom have values of 1 (or are at least of order unity – see Appendix A1 for details) [3]. Given then, its obvious and necessary role in formulating both the description and the analysis of our experiment, we present in this chapter, a brief development of some fundamental properties of the Hydrogen atom.

Composed of a single electron interacting with an oppositely charged nucleus, the Hydrogenic atom is in many ways the simplest of physical systems. Classically, its description is one of the oldest known: orbital motion under the influence of a central force. Quantum mechanically, its description reduces to the solution of a one dimensional differential equation, the radial Schrödinger Equation, and is the only atomic system for which this equation can be exactly solved[4].

In certain cases, there is significant agreement between the classical and quantum mechanical pictures. It is this agreement which we will exploit

in order to describe the more complex two-electron systems directly relevant to our work.

1.1 The Classical Hydrogenic Atom

The classical Hydrogenic Atom has a point particle of negative unit charge (the electron), orbiting a point nucleus of charge $Z > 0$, and infinite mass located at the origin. The electron's position is specified in spherical coordinates by r , θ , and ϕ . The variable r is the separation between the electron and the nucleus, while θ and ϕ are the polar and azimuthal angles about an arbitrarily imposed right-handed coordinate system.

It is not our intent to develop explicit expressions for the position of the electron as a function of time (In fact, while simple expressions can be obtained for $t(r)$ or $t(\theta)$, inverting these expressions to determine $\mathbf{r}(t)$ is quite an involved process [5]). Rather, we will derive quantitative descriptions with which to characterize all allowed motions.

1.1.1 The Equations of Motion

Before we derive the equations of motion, in order to simplify our analysis we will exploit the spherical symmetry of the system to reduce the number of coordinates we need consider. [5]

Consider the time derivative of total angular momentum vector, $\mathbf{L} \equiv \mathbf{r} \times \mathbf{p}$, (where $\mathbf{p} \equiv m \dot{\mathbf{r}}$).

$$\dot{\mathbf{L}} = \dot{\mathbf{r}} \times \mathbf{p} + \mathbf{r} \times \dot{\mathbf{p}} \quad (1.1)$$

The first of these terms vanishes, since $\dot{\mathbf{r}}$ is parallel to \mathbf{p} . The Second term also vanishes, since Newton's Second Law, when applied to a spherically symmetric potential, reads

$$\dot{\mathbf{p}} = -\frac{\mathbf{r}}{r} \partial_r \mathcal{V}[r]. \quad (1.2)$$

With both terms vanishing, the total angular momentum (both orientation and magnitude) is clearly conserved; that is, the total angular momentum remains constant throughout the time development of the system.

If we then proceed to remove the arbitrary orientation of our coordinate system by fixing \mathbf{L} to be along the polar axis ($\theta \equiv \frac{\pi}{2}$), we restrict the motion of the electron to be in the plane perpendicular to the polar axis and reduce the number of coordinates by one.

Assuming these coordinates to be functions of time, the Lagrangian for the system is

$$\mathcal{L} = \frac{1}{2} \dot{r}^2 + \frac{1}{2} r^2 \dot{\phi}^2 + \frac{Z}{r}. \quad (1.3)$$

The resulting equations of motion (noting that the coordinate ϕ does not appear in the Lagrangian) are

$$\dot{\phi} = \frac{L}{r^2}, \text{ and} \quad (1.4)$$

$$\ddot{r} - \frac{L^2}{r^3} = -\frac{Z}{r^2}. \quad (1.5)$$

The first of these equations is simply a restatement of our aforementioned result that the magnitude of total angular momentum is conserved. The solution of the second equation, while not intractable by any means, involves non-algebraic relationships between transcendental functions of r and t and is best solved numerically. Since we are seeking qualitative understanding as well as quantitative descriptions of the allowed motions, it is far more useful if we proceed to manipulate equation (1.5) as follows:

$$\ddot{r} = \frac{L^2}{r^3} - \frac{Z}{r^2} = \partial_r \left(-\frac{L^2}{2r^2} + \frac{Z}{r} \right) \quad (1.6)$$

$$\dot{r} \ddot{r} = \dot{r} \partial_r \left(-\frac{L^2}{2r^2} + \frac{Z}{r} \right) \quad (1.7)$$

$$\partial_t \left(\frac{1}{2} \dot{r}^2 \right) = \dot{r} \partial_r \left(-\frac{L^2}{2r^2} + \frac{Z}{r} \right) \quad (1.8)$$

$$\partial_t \left(\frac{1}{2} \dot{r}^2 + \frac{L^2}{2r^2} - \frac{Z}{r} \right) = 0 \quad (1.9)$$

This last equation reveals the existence of another conserved quantity, the Energy (\mathcal{E}), which forms the basis for the rest of our analysis.

$$\mathcal{E} = \frac{1}{2} \dot{r}^2 + \frac{L^2}{2r^2} - \frac{Z}{r} \quad (1.10)$$

It should also be apparent that our problem is now equivalent to that of an electron in one dimension (r) acting under the influence of the effective potential $\frac{L^2}{2r^2} - \frac{Z}{r}$.

1.1.2 Bound State Motion

As we are only interested in characterizing the closed orbits of our system, we will work with $\mathcal{E} \leq 0$ for the rest of this section. In the most general terms possible, orbits described by Equation (1.10) will consist of radial excursions out to some maximal distance, r_{outer} , followed by a return trip to some minimal distance, r_{inner} . Since the electron reverses course at both of these locations, its radial velocity at these turning points must vanish. Solving Equation (1.10) for the values of r at which the radial velocity vanishes is then a simple method for determining the turning points.

$$r_{\text{outer, inner}} = \frac{Z}{2(-\mathcal{E})} \left(1 \pm \sqrt{1 - \frac{2L^2(-\mathcal{E})}{Z^2}} \right) \quad (1.11)$$

Qualitatively, we see that the inner turning point is dominated by the angular momentum. This can be seen either by noting that the L^2 term dominates Equation (1.10) in the small r limit, or by expanding the radical in Equation (1.11) and noting that the leading order term is

proportional to L^2 . This point will reappear in the next chapter. Similarly, by examining Equation (1.10) in the large r limit, we see that the outer turning point is almost completely determined by the energy and nuclear charge.

These orbits can be further characterized by calculating the duration of a complete cycle, or period of the orbital motion, τ . We start by writing the identity

$$dt = \frac{dr}{\dot{r}}. \quad (1.12)$$

Symmetry arguments applied to Equation (1.10) then lead us to the expression

$$\tau = \sqrt{2} \int_{r_i}^{r_o} \frac{r}{\sqrt{\mathcal{Z}r - \frac{L^2}{2} + \mathcal{E}r^2}} dr. \quad (1.13)$$

Simple algebra reveals

$$\frac{L^2}{2} = -\mathcal{E}(r_o r_i), \text{ and} \quad (1.14)$$

$$r_o + r_i = -\frac{\mathcal{Z}}{\mathcal{E}}, \quad (1.15)$$

so that we can re-parameterize our expression as

$$\tau = \sqrt{\frac{2}{-\mathcal{E}}} \int_{r_i}^{r_o} \frac{r}{\sqrt{(r_o + r_i)r - (r_o r_i) - r^2}} dr, \quad (1.16)$$

or

$$\tau = \sqrt{\frac{2}{-\mathcal{E}}} \int_{r_i}^{r_o} \frac{r}{\sqrt{(r_o - r)(r - r_i)}} dr. \quad (1.17)$$

Based on the discussion following Equation (1.10), we choose to recast our variable of integration as

$$r = \frac{r_o + r_i}{2} - \frac{r_o - r_i}{2} \cos[\gamma], \quad (1.18)$$

thus explicitly including the bound nature of the orbits in our calculation.

After noting that $\sin[\gamma] \geq 0$ for $0 \leq \gamma \leq \pi$, the resulting integration is trivially completed,

$$\tau = \sqrt{\frac{2}{-\mathcal{E}}} \int_0^\pi \frac{\left(\frac{r_o + r_i}{2} - \frac{r_o - r_i}{2} \cos[\gamma]\right) \left(\frac{1}{2} \sin[\gamma] (r_o - r_i)\right) d\gamma}{\sqrt{\frac{1}{4} \sin^2[\gamma] (r_o - r_i)^2}} \quad (1.19)$$

$$\tau = \sqrt{\frac{2}{-\mathcal{E}}} \int_0^\pi \left(\frac{r_o + r_i}{2} - \frac{r_o - r_i}{2} \cos[\gamma]\right) d\gamma, \quad (1.20)$$

$$\tau = \sqrt{\frac{2}{-\mathcal{E}}} \pi \frac{r_o + r_i}{2}, \quad (1.21)$$

resulting in a simple expression for the Kepler period:

$$\tau = 2\pi \frac{\mathcal{Z}}{(-2\mathcal{E})^{3/2}}. \quad (1.22)$$

It is interesting to note that for a given hydrogenic atom, the period depends on the total energy only -- it is completely independent of the orbital angular momentum.

While we have not determined an explicit equation for $r[t]$, there remains a large amount of position-related information which we are nonetheless able to calculate. For example, one might be interested in determining the average value of $r[t]$. As Bensky [6] points out, the integrand in Equation (1.13) is proportional to the classical probability of finding the electron within dr of r . The constant of proportionality is, fortuitously enough, the inverse of the period that we just calculated. Using our previous results and parameterizations, we write the normalized probability density as

$$\mathcal{P}_{cl}[r] dr = \frac{2}{\pi(r_o + r_i)} \frac{r}{\sqrt{(r_o - r)(r - r_i)}} dr. \quad (1.23)$$

While we can use this expression to calculate the average value of any function $f[r]$ we desire, it is mathematically simpler to use our γ parameterization, Equation (1.18), and evaluate the integral as

$$\begin{aligned} f_{ave} = \\ \frac{2}{\pi(r_o + r_i)} \int_0^\pi f[r[\gamma]] \left(\frac{r_o + r_i}{2} - \frac{r_o - r_i}{2} \cos[\gamma] \right) d\gamma. \end{aligned} \quad (1.24)$$

In the table below, we present the classical expectation values of r^n for several values of n . These values will be of use to us in determining the circumstances under which classical and/or semiclassical descriptions of atomic systems are justified.

n	$\langle r^n \rangle_{\text{Cl}}(r_i, r_o)$	$\langle r^n \rangle_{\text{Cl}}(\mathcal{E}, L^2, \mathcal{Z})$
2	$\frac{5}{8}(r_i + r_o)^2 - \frac{3}{2}r_i r_o$	$\frac{5\mathcal{Z}^2 + 6L^2(-\mathcal{E})}{8\mathcal{E}^2}$
1	$\frac{3(r_i + r_o)^2 - 4r_i r_o}{4(r_i + r_o)}$	$\frac{3\mathcal{Z}}{-4\mathcal{E}} - \frac{L^2}{2\mathcal{Z}}$
-1	$\frac{2}{r_i + r_o}$	$\frac{2(-\mathcal{E})}{\mathcal{Z}}$
-2	$\frac{2}{\sqrt{r_i r_o}(r_i + r_o)}$	$\frac{(-2\mathcal{E})^{3/2}}{L\mathcal{Z}}$
-3	$\frac{1}{(r_i r_o)^{3/2}}$	$\frac{(-2\mathcal{E})^{3/2}}{L^3}$
-4	$\frac{3(r_i + r_o)^2 - 4r_i r_o}{4(r_i r_o)^{5/2}(r_i + r_o)}$	$\frac{(-2\mathcal{E})^{3/2}(\frac{3}{2}(\mathcal{Z}/L)^2 - (-\mathcal{E}))}{L^3\mathcal{Z}}$

Table 1.1

Expectation values of r^n for various values of n . Results are expressed in terms of the inner and outer turning points and, equivalently, in terms of Energy (\mathcal{E}), Angular Momentum (L), and nuclear charge (\mathcal{Z}). The results were calculated using Equation (1.24).

For general n , we can express this integral in terms of a Hypergeometric function [7]

$$\langle r^n \rangle = \frac{2 r_o^{1+n}}{r_o + r_i} {}_2F_1\left[\frac{1}{2}, -1 - n, 1, 1 - \frac{r_i}{r_o}\right]. \quad (1.25)$$

While interesting, this result is only really useful in the special case of $n \geq 0, L = 0 (\implies r_i = 0)$, where it reduces to a simpler form.

$$\begin{aligned} \langle r^n \rangle &= 2 \frac{\Gamma[n + \frac{3}{2}]}{\sqrt{\pi}} \frac{r_o^n}{(n+1)!} = \frac{(2n+1)!!}{(n+1)!} \left(\frac{r_o}{2}\right)^n \\ &= \frac{(2n+1)!!}{(n+1)!} \left(\frac{\mathcal{Z}}{-2\mathcal{E}}\right)^n \end{aligned} \quad (1.26)$$

In summary, then, we find that for the classical Hydrogenic atom, both energy and total angular momentum are conserved. Further, all closed orbits have a natural period that depends on the energy only -- the

Kepler period. The spatial probability distribution and all of its moments are completely described in terms of L , \mathcal{E} , and Z (or, equivalently, the inner and outer turning points). Finally, we note that $\langle r^n \rangle \sim r_o^n$, and that $r_o \sim \frac{Z}{-\mathcal{E}}$. Specifically, this means that (taking the case $n = 1$) the classical electron is most likely to be found near its outer turning point, and that the turning point moves outward from the nucleus as the electron's energy approaches zero.

1.2 The Quantum Mechanical Hydrogenic Atom

Our investigation of the probability distribution in the last section leads us quite naturally into a quantum mechanical analysis of the Hydrogenic atom. In the framework of Quantum Mechanics, the electron is no longer treated as a point particle deterministically moving in accordance with Equation (1.10). Instead, the electron is characterized by a wavefunction -- a complex valued 'amplitude' that extends over all space and evolves in time as described by the Schrödinger Equation. The absolute value squared of the wavefunction, evaluated at a given point in space, gives the probability of the electron existing within an infinitesimal volume about that point.

The Time Independent Schrödinger Equation (TISE) for a hydrogenic atom (with all variables shown corresponding to their classical counterparts defined in the previous section)

$$-\frac{1}{2} \nabla^2 \Psi[r, \theta, \phi] - \frac{Z}{r} \Psi[r, \theta, \phi] = \mathcal{E} \Psi[r, \theta, \phi], \quad (1.27)$$

can be solved using standard separation of variables techniques [8,9] starting with the factorization of the wavefunction as

$$\Psi[r, \theta, \phi] = \frac{u[r]}{r} Y_{\ell, m}[\theta, \phi]. \quad (1.28)$$

The function $Y_{\ell, m}[\theta, \phi]$ is a normalized spherical harmonic, where ℓ and m are, respectively, the orbital and magnetic quantum numbers of the electron. Insertion of Equation (1.28) into (1.27) yields a radial equation in the form of a one dimensional TISE with an effective potential of $\frac{\ell(\ell+1)}{2r^2} - \frac{Z}{r}$;

$$-\frac{1}{2} \partial_{r,r} u[r] + \left(\frac{\ell(\ell+1)}{2r^2} - \frac{Z}{r} \right) u[r] = \mathcal{E} u[r]. \quad (1.29)$$

The appropriateness of the identification of ℓ as the orbital angular momentum quantum number, and some of its significance can be seen if the effective potential in Equation (1.29) is compared with the classical effective potential $\left(\frac{L^2}{2r^2} - \frac{Z}{r} \right)$ from the previous section.

As was the case classically, the $r \rightarrow 0$ behavior of the equation of motion is completely dominated by the angular momentum term. To expose this

behavior, we drop the coulomb and energy eigenvalue terms from Equation (1.29), and substitute a leading order behavior for $u[r]$ of the form

$$u[r \rightarrow 0] = u_0 r^\gamma . \quad (1.30)$$

This resulting equation is satisfied for only two values of γ :

$$\begin{aligned} \gamma &= \ell + 1 \\ \gamma &= -\ell \end{aligned} . \quad (1.31)$$

Thus, we find that there are two solutions to Equation (1.29) that can be characterized by their behavior near the origin: $f[r, \ell, \mathcal{E}]$ (the regular coulomb function) which vanishes as $r^{\ell+1}$, and $g[r, \ell, \mathcal{E}]$ (the irregular coulomb function) which diverges as $\frac{1}{r}$. [10] These solutions are linearly independent, so that the most general solution to Equation (1.29) is (by convention)

$$u[r] = (\text{Cos}[\pi \delta] f[r, \ell, \mathcal{E}] - \text{sin}[\pi \delta] g[r, \ell, \mathcal{E}]) . \quad (1.32)$$

In our development of Multi-Channel Quantum Defect Theory, the phase δ will acquire some physical significance. At this point, however, it is simply taken to be a phase so that if $f[r, \ell, \mathcal{E}]$ and $g[r, \ell, \mathcal{E}]$ are both normalized, then $u[r]$ will also be normalized.

In order to calculate expectation values, the function $u[r]$ must be square-integrable over the entire range of r . Specifically, we demand

that $u[r]$ be regular at the origin; this is achieved by setting the coefficient of $g[r,\ell,\mathcal{E}]$ to zero, that is, δ is taken to be an integer. With this assignment, the coefficient of the regular coulomb function reduces to ± 1 (Since measurable quantities depend only on $u[r]^2$, we will drop this irrelevant phase.). It now remains for us to develop an explicit expression for this function.

As $r \rightarrow \infty$, the approximate equation of motion is seen to be

$$-\frac{1}{2} \partial_{r,r} u[r] = \mathcal{E} u[r] . \quad (1.33)$$

Since we are interested in the bound states of Hydrogen, as we did in the classical case, we restrict ourselves here to values of $\mathcal{E} < 0$. The general solution to this approximate equation is easily verified to be

$$u[r \rightarrow \infty] = A E^{-\sqrt{-2\mathcal{E}} r} + B E^{\sqrt{-2\mathcal{E}} r} . \quad (1.34)$$

The aforementioned requirement of square-integrability is satisfied in this regime by setting $B = 0$. That is, we require our bound states to vanish exponentially as $r \rightarrow \infty$.

With these limiting behaviors in mind, and following Schiff [11], we solve Equation (1.29) for $f[\mathcal{E} < 0, \ell, r]$ by assuming a power series solution of the form

$$u[r] = u_0 r^{\ell+1} E^{-\sqrt{-2\mathcal{E}} r} \sum_{j=0}^{\infty} a_j r^j . \quad (1.35)$$

In order for the series to terminate with a finite number of terms, the energy is required to be quantized [11]:

$$\mathcal{E}_n = -\frac{\mathcal{Z}^2}{2n^2}, \quad (1.36)$$

and the angular momentum eigenvalue is restricted to be an integer such that

$$0 \leq \ell \leq (n-1). \quad (1.37)$$

The finite series are identified as the Generalized Laguerre polynomials, and the corresponding normalized radial eigenfunctions are written as

$$u_{n,\ell}[r] = (-1)^{n+1+\ell} \left(\frac{2\mathcal{Z}}{n}\right)^{1/2} \sqrt{\frac{(n-\ell-1)!}{2n(n+\ell)!}} \left(\frac{2\mathcal{Z}r}{n}\right)^{\ell+1} e^{-\frac{\mathcal{Z}}{n}r} \mathcal{L}_{n-\ell-1}^{2\ell+1}\left[\frac{2\mathcal{Z}r}{n}\right]. \quad (1.38)$$

In anticipation of future work, we have chosen the overall (and physically arbitrary) phase of our eigenfunctions such that the outer-most lobe is always positive. This results in the sign of the innermost lobe alternating as n increases. This convention is chosen so as to be in agreement with the wavefunctions which we will generate numerically for non-integer effective principle quantum numbers in later chapters.

Examination of Equation (1.29), reveals that there are two values of r for which the coefficient of $u[r]$, and hence its second derivative must vanish.

Clearly, these are the quantum mechanical equivalents of the classical turning points (Refer to Equation (1.11) in light of Equations (1.36) and (1.37)).

$$r_{\text{outer, inner}} = \frac{n^2}{Z} \left(1 \pm \sqrt{1 - \frac{\ell(\ell+1)}{n^2}} \right) \quad (1.39)$$

Physically, these points correspond to the locations where the effective potential becomes greater than the energy of the electron. Mathematically, these turning points correspond to the point where $u[r]$ begins to be dominated by the small- r and large- r asymptotic forms deduced above.

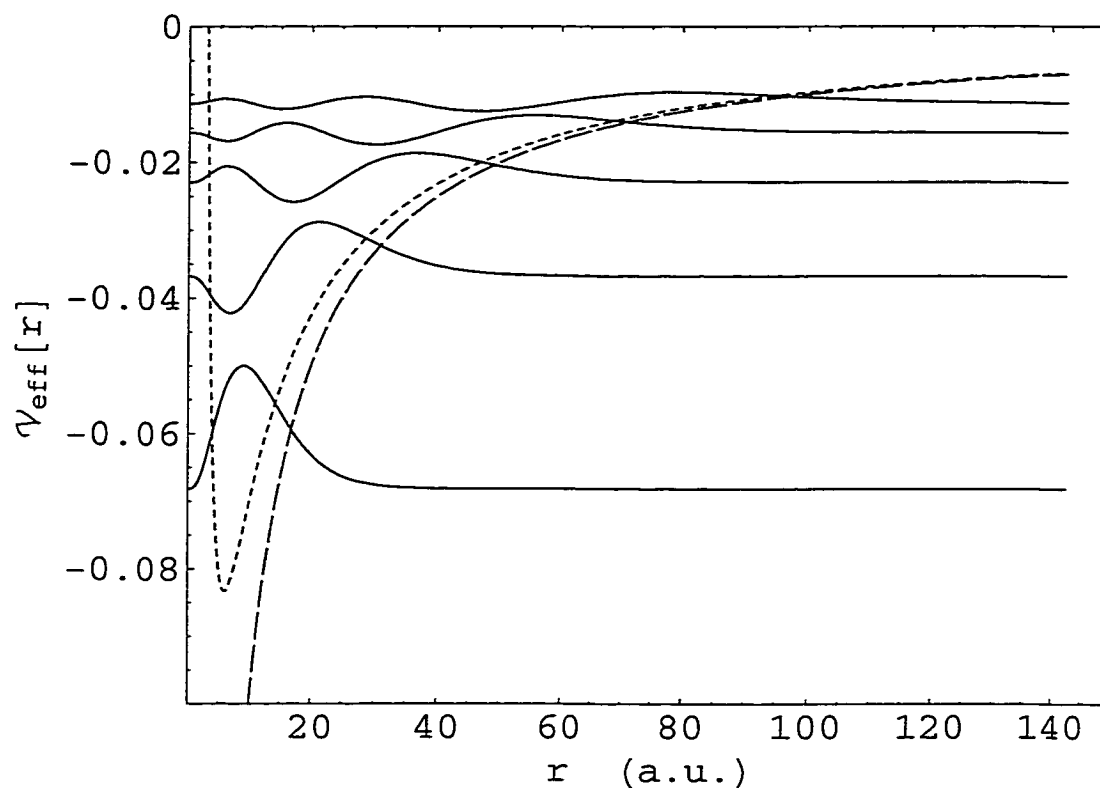


Figure 1.1

$\ell=2$ radial wave functions for $3 \leq n \leq 7$ (solid lines) superimposed on the coulomb potential (large dashed line) and the effective potential (small dashed lines) seen by the electron.

In Figure 1.1 above, we plot the coulomb potential (long dashed line) and the total effective potential (short dashed line) for $\ell = 2$. Superimposed on this plot are the radial coulomb functions for $3 \leq n \leq 7$. The amplitude of each function is scaled so that it intersects the effective potential at the outer turning point. This scaling results in the wavefunctions intersecting the effective potential at the inner turning point as well. These intersections serve to illustrate our previous claim that the inner turning point is almost completely determined by the

value of ℓ . In this case, $\ell = 2$, they occur at approximately the same position for each function. For $n = 3$, $r_i = 3.8$ atomic units, while for $n = 7$, $r_i = 3.1$ atomic units. As n increases, the location of the inner turning point very quickly approaches its limiting value of $r_i = \frac{1}{2} \ell(\ell + 1)$.

In Figure 1.2 below, we again plot the coulomb potential (long dashed line) and the total effective potential (short dashed line) for $\ell = 2$. This time, however, we superimpose on the radial probability distributions ($\rho_{n,\ell}[r] \equiv r^2 u_{n,\ell}[r]^2$) for $3 \leq n \leq 7$. The scalings employed are similar to those described above. The r^2 weighting enhances the size of the outer lobes relative to the inner ones, and it becomes apparent that the electron is most likely to be found near the outer turning point.

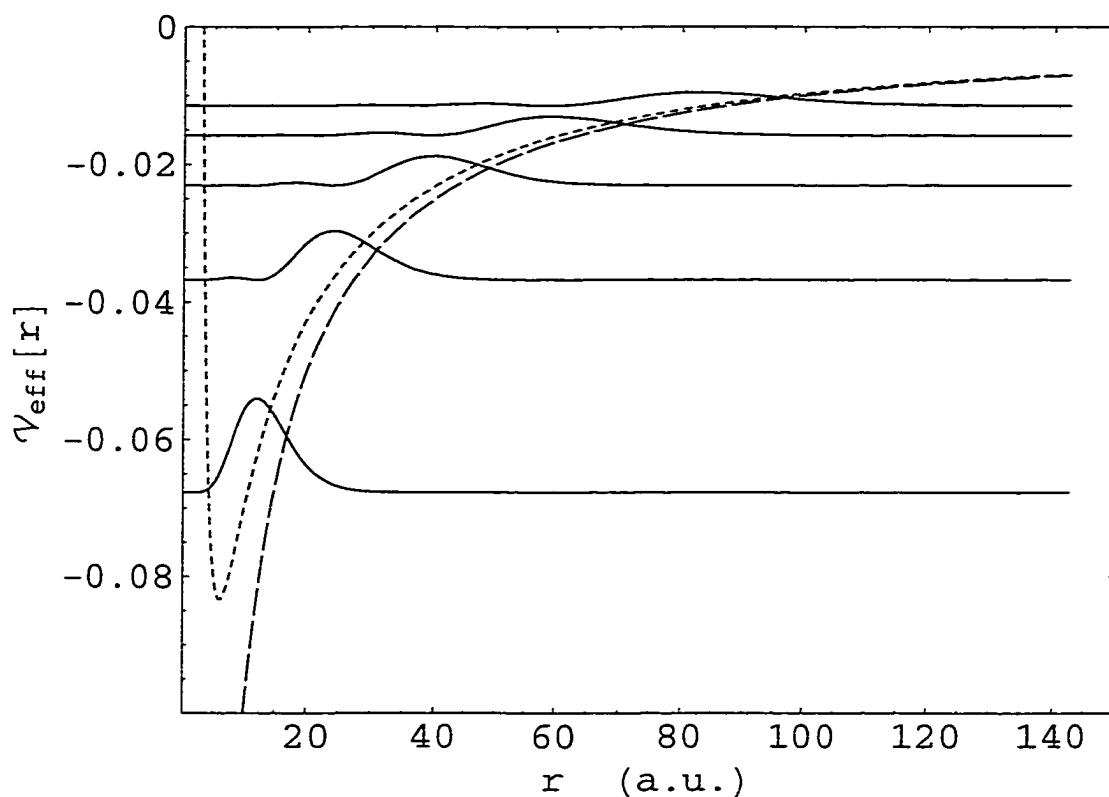


Figure 1.2

$l=2$ radial probability distributions for $3 \leq n \leq 7$ (solid lines) superimposed on the coulomb potential (large dashed line) and the effective potential (small dashed lines) seen by the electron. The distributions are scaled so that they intersect the effective potential at the outer turning point. Note how the maximum in the probability distribution is always near this point.

While the large- r , exponential decay of $u[r]$ is easily seen in the Figures above, the small- r , r^{l+1} behavior is not. In Figure 1.3 below, we plot (on a *logarithmic scale*), the radial coulomb functions for $3 \leq n \leq 7$. For comparison, we have added curves of the form $a_n r^{l+1}$ (dashed lines).

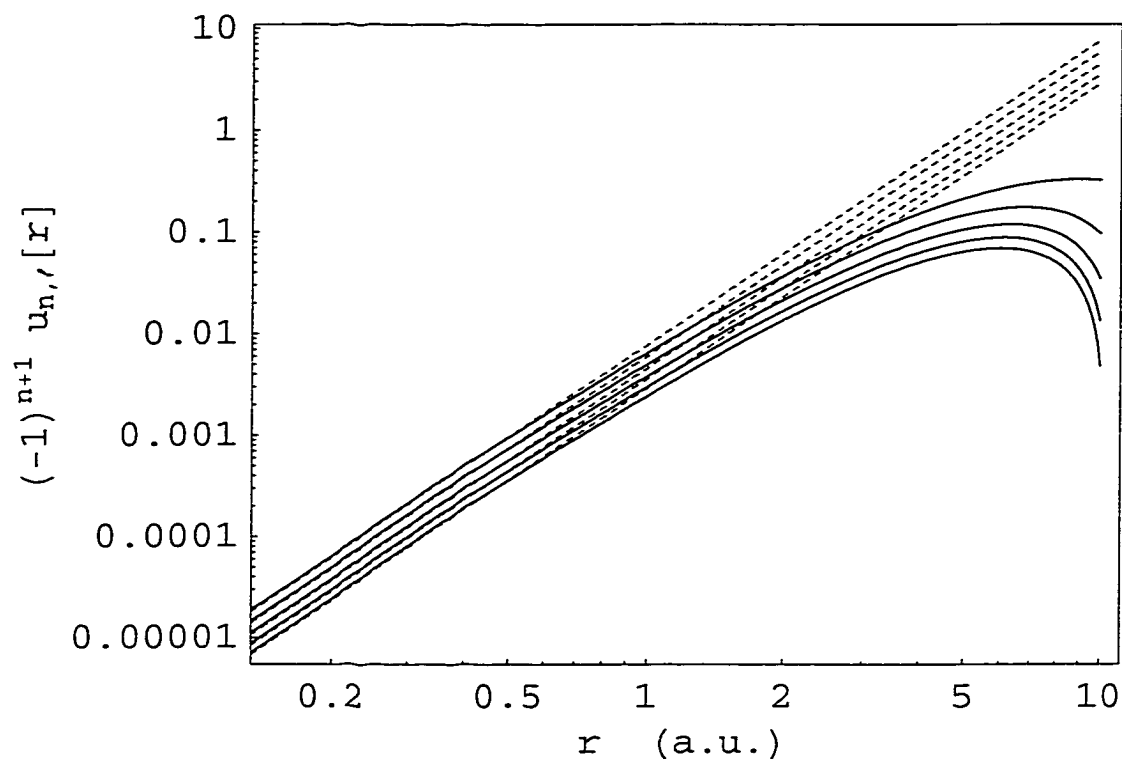


Figure 1.3

$l=2$ radial wave functions for $3 \leq n \leq 7$ (solid lines), plotted on a Log-Log scale, superimposed on asymptotes $\sim r^{l+1}$. The inner turning point for all these functions is ≈ 3 a.u., and it is clear that this point marks the small- r transition to power-law behavior for the wavefunctions. In this plot, we have adjusted the physically irrelevant phases so that our small- r wavefunctions are positive.

We are now in a position to calculate expectation values for various values of r^σ . [12] For comparison, we include the classical results obtained above, along with their "quantized" versions.

σ	$\langle r^\sigma \rangle_{\text{Cl}} (\mathcal{E}, L^2, \mathcal{Z})$	$\langle r^\sigma \rangle_{\text{Cl}} (n, \ell, \mathcal{Z})$	$\langle r^\sigma \rangle_{\text{QM}} (n, \ell, \mathcal{Z})$
2	$\frac{6L^2\mathcal{E}+5\mathcal{Z}^2}{8\mathcal{E}^2}$	$\frac{n^2}{2\mathcal{Z}^2} (5n^2 - 3\ell(1+\ell))$	$\frac{n^2}{2\mathcal{Z}^2} (5n^2 - 3\ell(1+\ell))$
1	$-\frac{L^2}{2\mathcal{Z}} - \frac{3\mathcal{Z}}{4\mathcal{E}}$	$\frac{1}{2\mathcal{Z}} (3n^2 - \ell(1+\ell))$	$\frac{1}{2\mathcal{Z}} (3n^2 - \ell(1+\ell))$
-1	$\frac{2(-\mathcal{E})}{\mathcal{Z}}$	$\frac{\mathcal{Z}}{n^2}$	$\frac{\mathcal{Z}}{n^2}$
-2	$\frac{(-2\mathcal{E})^{3/2}}{L\mathcal{Z}}$	$\frac{\mathcal{Z}^2}{n^3 \sqrt{\ell(\ell+1)}}$	$\frac{\mathcal{Z}^2}{n^3 (\ell+1/2)}$
-3	$\frac{(-2\mathcal{E})^{3/2}}{L^3}$	$\frac{\mathcal{Z}^3}{n^3 \ell^{3/2} (\ell+1)^{3/2}}$	$\frac{\mathcal{Z}^3}{n^3 \ell(\ell+1)(\ell+1/2)}$
-4	$\frac{(-2\mathcal{E})^{3/2} (L^2\mathcal{E} + \frac{3}{2}\mathcal{Z}^2)}{L^5\mathcal{Z}}$	$\frac{(3n^2 - \ell(\ell+1))\mathcal{Z}^4}{2n^5 \ell^{5/2} (\ell+1)^{5/2}}$	$\frac{(3n^2 - \ell(\ell+1))\mathcal{Z}^4}{2n^5 \ell(1+\ell)(\ell+1/2)(\ell-1/2)(\ell+3/2)}$

Table 1.2

Expectation values of r^σ for various values of σ . Results are expressed in terms of Energy (\mathcal{E}) – or alternatively (n), Angular Momentum (ℓ), and nuclear charge (\mathcal{Z}). The results were calculated using both classical and quantum mechanical[12] expressions. The two formulations agree for $n \geq -1$. The classical results for $n < -1$ are approximately correct in the Large- n , Large- ℓ , limit.

Surprisingly, we see that our classical expectations are correct for $\sigma \geq -1$. For $\sigma < -1$, the classical expectations are clearly wrong, but just as clearly, we see that numerically, they begin to approach the correct values as ℓ (and of necessity n) becomes large.

There is a lot of physics to be extracted from these observations. First, we note that in calculating expectation values of r^σ , different regions of $u[r]$ receive different weightings: for $\sigma < 0$, $\langle r^\sigma \rangle$ is dominated by contributions near the nucleus, while for $\sigma > 0$, $\langle r^\sigma \rangle$ is dominated by contributions near the outer turning point. We take this to mean that the considerations that led to our classical probability distribution, Equation(1.23), are valid at large distances from the nucleus ($r \sim r_o$) but break down at very short distances ($r \sim r_i$). This interpretation is

supported when one considers the conditions under which our classical expectations for the reciprocal powers of r became 'correct' -- large n and ℓ . The largest possible value for any ℓ is $n - 1$. In this case, the expression for the turning points becomes

$$r_{\text{outer, inner}} = \frac{n^2}{Z} \left(1 \pm \frac{1}{\sqrt{n}} \right). \quad (1.40)$$

For large values of n , we see that $u[r]$ becomes radially localized around $\frac{n^2}{Z}$, which is clearly far away from the nucleus.

Chapter 2 Rydberg Atoms and Autoionization

Rydberg Atoms are useful experimental "laboratories" for several reasons. Primarily, they are easily produced using nanosecond lasers in a table-top environment. Secondly, their properties are easily understood in terms of simple classical and quantum mechanical pictures. Finally, Rydberg states lie quite close (energetically speaking) to the ionization threshold of an atom, and therefore are useful for exploring all sort of excitation phenomena resulting in an ion with an unbound electron [13].

In this Chapter, we investigate the aforementioned simple pictures of a Rydberg atom as they apply to our experiment. From these pictures we develop a wavefunction representation for a Rydberg electron. We introduce the process of autoionization, and present a sketch of Multi-Channel Quantum Defect theory (MQDT) in order to describe it.

2.1 Rydberg Atoms -- the Physical Framework for MQDT

The basic picture we will use in our theoretical development is that of an atom with two electrons in its outer shell: that is, He or an alkaline earth atom. One of the electrons is taken to have a large principle quantum number n (the "outer", or Rydberg electron), while the other electron (the "inner" electron) is taken to be in a much lower state. While any atom with at least one Rydberg electron can be considered a Rydberg atom, we will focus for now on singly excited alkaline earth atoms -- to be precise, Calcium.

As measured from the ionization limit, the energy of the outer electron is written as

$$\mathcal{W} \equiv -\frac{1}{2(n-\delta)^2}, \quad (2.1)$$

where n is the principle quantum number, and δ is known as the quantum defect. The energy of the atom, then, is the sum of the energy of the outer electron with that of the ionic core (ionic core = inner electron + all electrons in closed shells). A Rydberg series is simply a grouping of all the states of the atomic system possessing identical quantum numbers *except* for the principle quantum number of the

Rydberg electron. As the principle quantum number of the outer electron increases, its contribution to the total atomic energy decreases; vanishing in the limit $n \rightarrow \infty$. Physically, this ultra-large- n limit corresponds to the ion produced by removing the outer electron from the atom, and the Rydberg series is said to converge to this ionic energy level. The term "channel" is used to refer collectively to a given Rydberg series, and the continuum states for the outer electron as its energy is increased above the ionization limit.

In presenting this picture, we are making several tacit assumptions. First, we are assuming that we can separate out the behavior of the outer electron from the rest of the atomic system -- that is, that we can write down a wavefunction for the outer electron, labeled by its energy, that depends only on its coordinates. Second, we assume this wave function to be somewhat "hydrogenish" -- at least near the classical outer turning point. Third, we assume the core to be a spherically symmetric distribution of N protons and $N-2$ electrons that is unaffected by the states of the two valence electrons.

In a complete "first principles" calculation, for example, the wave function of an N -electron system depends on the coordinates of all of the electrons, and must account for exchange effects as well as possessing an overall antisymmetric form.[14] Separating out the Rydberg electron's

behavior from that of the remaining electrons profoundly simplifies our calculations. We are lead to this assumption (wavefunction separability) from our analysis of hydrogenic atoms in Chapter 2. Specifically, we saw that as the principle quantum number grew, classical descriptions became increasingly valid, and the electron was more likely to be found away from the nucleus. Classically, we can say that the electron spent more time near the outer turning point, which was shown to increase like n^2 . We assume the same sort of behavior for the Rydberg electron in our non-hydrogenic atom. Classically, then, near its outer turning point, the Rydberg electron sees a simple coulombic potential. We construct a wavefunction for the Rydberg electron by solving the radial Schrödinger equation corresponding to this classical picture.

$$-\frac{1}{2} \partial_{r,r} u[r] + \left(\frac{\ell(\ell+1)}{2r^2} - \frac{1}{r} \right) u[r] = \mathcal{W} u[r] \quad (2.2)$$

This equation is formally identical to Equation (1.29), but it should be remembered that the $\frac{1}{r}$ coulombic potential is only valid in an asymptotic sense. For small- r values, the actual potential is usually deeper than coulombic as the Rydberg electron should be able to "see" past the inner electrons, partially "viewing" the nuclear charge at the core.

Our Rydberg wavefunction, then, should be formally identical to the hydrogenic wavefunction we found in the last chapter,

$$u[r] = \text{Cos}[\pi\delta_\ell] f[r, \ell, \mathcal{W}] - \text{sin}[\pi\delta_\ell] g[r, \ell, \mathcal{W}], \quad (2.3)$$

but in light of our comments above, there will be several significant differences. First, Equation (2.3) is only valid for $r > r_c$, where r_c is some effective core radius at which the potential is no longer simply coulombic, and hence our radial equation is no longer valid. Since Equation (2.3) is not valid near the origin, we cannot simply eliminate the irregular solution based on its $r^{-\ell}$, small -r divergence. This situation turns out to be appropriate, as we need the irregular coulomb function to describe (spatially) the large-r behavior of a "hydrogenish" wavefunction that is "pulled into" the deeper potential of an imperfectly screened core. The quantum defect δ is now seen to determine the amount of irregular coulomb wavefunction present at $r > r_c$, and in fact, Equation (2.3) gives the exact linear combination of regular and irregular components to ensure that a wavefunction with energy given by Equation (2.1) vanishes at infinity. [15]

The second difference in our radial solution is underscored by a change of notation: the quantum defect δ is written as δ_ℓ . The implication of this new notation is that the quantum defect for a given ℓ depends strongly on ℓ , and is essentially energy independent (in other words, δ_ℓ doesn't

depend on n). This can be understood qualitatively as follows. Since the potential differs from that of hydrogen only for $r < r_c$, the value of the quantum defect must be determined by interactions close to the core, i.e. interactions with the rest of the atomic electrons. The classical inner turning point is a good measure of how close the Rydberg electron gets to the core, and was shown to be

$$r_{\text{inner}} = \frac{1}{2(-\mathcal{E})} \left(1 - \sqrt{1 - 2L^2(-\mathcal{E})} \right), \quad (2.4)$$

or

$$r_{\text{inner}} = n^{*2} \left(1 - \sqrt{1 - \frac{\ell(\ell+1)}{n^{*2}}} \right) \quad (2.5)$$

where $n^* \equiv n - \delta_\ell$, and is referred to as the *effective* principle quantum number. For large- n Rydberg states, we can expand the expression for the inner turning point in a Taylor series, and we find that

$$r_{\text{inner}} \simeq \frac{\ell(\ell+1)}{2}, \quad (2.6)$$

independent of the energy. The correction term goes like $\left(\frac{\ell^2}{n^*}\right)^2$, so for large n and small ℓ , Equation (2.6) is a very good approximation.

Unfortunately, solutions to Equation (2.2) are difficult to write down analytically, and the calculation of matrix elements is even more difficult. For example, the series solution technique that we used for Hydrogenic atoms will no longer work. Since the effective principle

quantum number is not an integer, the series will not terminate at a finite number of terms, and consequently diverges for large r . This difficulty can be overcome to some extent if one also constructs a series solution in reciprocal powers of r . [42] This solution also fails to terminate, but it only diverges near the origin. An effective solution could then be constructed if one used each series in its region of applicability, while retaining only those terms that would remain if $\delta \rightarrow 0$, and determining appropriate multiplicative constants to ensure agreement in a region where both are well behaved. This is perhaps the simplest analytic method for constructing approximate non-hydrogenic wave functions, and a moment of reflection will show that just determining a normalization constant -- let alone calculating matrix elements -- will prove to be an arduous task. In the end, one resorts to calculating the matrix elements numerically, a choice which defeats the purpose for determining closed form expressions in the first place! The standard choice then, and the one which we will make for this work, is to construct all of our wavefunctions numerically, using the Numerov [29] method.

A complete description of this method, along with the *Mathematica* code we used to implement it is found in Appendix A2. Briefly though, the Numerov method is fast, accurate, and numerically stable (see below).

For bound states, we begin in a region of space well beyond the outer turning point where the wavefunction is essentially zero, and integrate the radial Schrödinger Equation inwards. We achieved very accurate results over several thousand Bohr radii with steps sizes as large as 0.25 au. Our claim that the Numerov method is stable requires one qualification: the integration must be stopped (and the rest of the wavefunction set to zero) at some well chosen point before $r = 0$. Simply, the wavefunction generated by the Numerov method contains the appropriate mixture of regular and irregular solutions for exponential vanishing at large r . This mixture is retained throughout the integration; hence, the small- r divergent behavior of the irregular solution would dominate near the origin. Clearly, this non-physical behavior must be discarded, as a physically correct wave function would vanish near the origin. The important thing to remember is that the physics in which we are interested is dominated by the large- r values of the wavefunction, so zeroing out the small- r values has no significant effect.

This last statement might seem counterintuitive and even paradoxical, since the interactions that make our wavefunctions different from their hydrogenic counterparts are only significant near the core. The resolution of this paradox foreshadows the power of the Multi-Channel

Quantum Defect Theory to be presented in the final section of this chapter. *Without knowing the exact form of the small- r interactions, we can infer their long range effects on Rydberg electrons, and efficiently "encode" these effects in the large- r wavefunctions we construct.*

2.2 Interacting Rydberg Series and Autoionizing States

In the last section, we used our previous analysis of Hydrogenic atoms to model Rydberg states. Using numerical techniques based on this model, we were able to construct a wavefunction for any state in a given Rydberg series. The next logical avenue to explore is how different Rydberg series in a given atom interact with, and thereby modify, each other.

We have defined a Rydberg series as a grouping of all the states of an atomic system that share a given ionic core state. The obvious implication of this definition is that each state of the ionic core corresponds to a different Rydberg series. Given the multiple series that must exist for a given atom, it is not impossible to imagine that the continuum states lying above a given series' ionization limit, might be iso-energetic with the bound states of a different series. Such a situation is illustrated below.

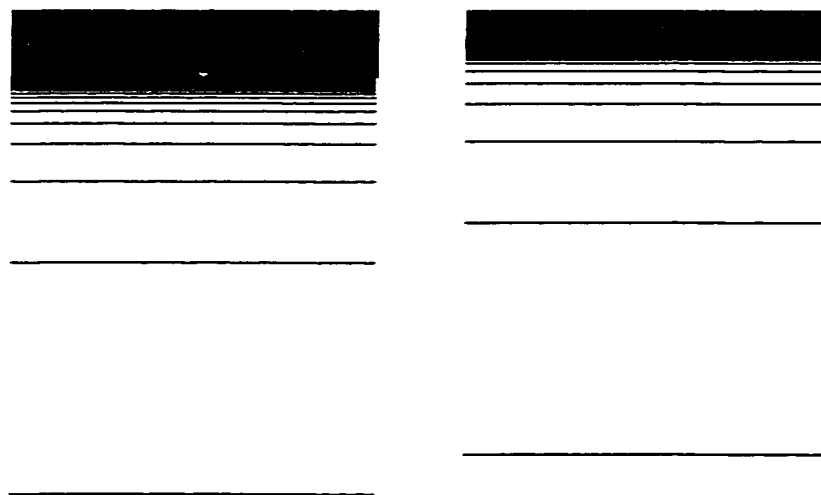


Figure 2.1

Autoionizing Rydberg series -- each group of lines corresponds to a different state of a two electron atom's ionic core. Each line within a series represents an energy level, or state in the series, with the solid black regions denoting continuum states. The otherwise bound states depicted on the right are energetically degenerate with the continuum states on the left. Autoionization occurs when the system makes a radiationless transition from the series on the right to the one on the left (i.e., a transition to an energetically lower ionic core state and a continuum electron).

The bound states of the "higher" series are known as autoionizing states and are in fact *no longer bound*. In the time domain we can easily understand how this process might come about -- at least qualitatively -- for our prototypical two-electron system. The inner electron makes a radiationless transition to an energetically lower state, while its excess energy is "given" to the outer electron in order to promote it to the continuum. The two electrons are able to interact with each other through the higher order terms in their mutual coulombic repulsion (the 0th order term is included in the $\frac{1}{r}$ potential appearing in the Rydberg electron's radial Hamiltonian). [16]

The classical analog of this time-domain picture is simply the "Planetary" model presented in the Introduction to this work. When "Mars" (the inner electron) made a rapid transition to a new, higher orbit, "Pluto" (the outer electron) suddenly found itself in an autoionizing Rydberg state and was soon scattered into the cosmos (continuum).

Within our planetary model, "Mars" made its "rapid transition to a higher orbit" after a "sudden explosion". The atomic level, experimental equivalent of this "sudden explosion" is an Isolated Core Excitation (ICE), a laser-induced promotion of the atom's ionic core to a higher energy state. [17] The ionic core excitation is described as "isolated", because it proceeds as if the Rydberg electron were not present. We explain this description in two ways. First, the ICE pulse has no *direct* effect on the Rydberg electron.[18] The Rydberg electron has a bound state energy on the order of 0.01 eV. The ICE pulses employed in our experiment have energies between 3 and 4 eV. The final state of an electron excited directly to the continuum by one of these pulses would have a very large kinetic energy (as compared to the binding energy of the initial state). The final state wavefunction would therefore be oscillating very rapidly in the region where the initial state function was a maximum -- the outer turning point. The transition moment for direct excitation is proportional to the dipole moment, or matrix element,

between these two states. The poor overlap of the wavefunctions results in a dipole moment that is extremely small; and consequently, the probability of direct excitation is also minuscule. On the other hand, the core excitation is a transition between two bound states of the system. The dipole moment is significantly larger, and with our pulses chosen to be resonant with the transition, the relative probability for core excitation approaches 1. We have just argued that the ICE pulse has no *direct* effect on the Rydberg electron; the second reason why our core excitation is "Isolated", is that the Rydberg electron has no effect on the core transition. This can be seen from our classical model; the Rydberg electron spends almost all of its time at the outer turning point. In order to influence the core excitation, the Rydberg electron would have to be significantly closer to the nucleus so that it exchanges momentum as well as energy with the core during the ICE pulse. For our experimental work, we make use of a short-pulse ICE technique so that the excitation occurs before the Rydberg wavefunction has time to react. This last consideration is only applicable, however, when an ICE is tuned so as to be on resonance with the transitions it drives, and when the bandwidth of the ICE is large compared to the energy spacing between Rydberg levels. Story, Duncan, and Gallagher [46] have demonstrated this in Mg -- both for on-resonance ICEs and ICEs with small detunings. For large

detunings, they show that the excitation only takes place when the Rydberg electron's energy is also able to change (and thus conserve total energy). As we have previously argued, this can only occur when the Rydberg electron is near the core.

In the frequency domain, autoionizing states are described by modifying the wavefunction used to describe the Rydberg electron. For example, a single bound series interacting with a single continuum results in a modification of the Rydberg electron's wavefunction of the form

$$\phi_{\text{Rydberg}} \rightarrow A\phi_{\text{Rydberg}} + B\phi_{\text{Continuum}} \quad (2.7)$$

The determination of the energy dependent functions A and B lies within the domain of Multi-channel Quantum Defect Theory and will be explored in the next section.

2.3 Multi-channel Quantum Defect Theory

Multi-channel Quantum Defect Theory (MQDT) is a physically intuitive mathematical description of Rydberg series in an atom, their couplings to, and interactions with, each other. Several equivalent formulations of MQDT exist [19-21], but in this work we shall use the formalism of Cooke and Cromer[20], as it is extremely well-suited for the description of autoionizing spectra resulting from Isolated Core Excitations. Specifically, their parameterization relies on relatively energy independent quantities that are easily extracted from ICE spectroscopic data.[20,25,26] Our hope is that the proven applicability of MQDT in the frequency domain can be extended to interactions in the time domain as well. Indeed this turns out to be the case, as our data and subsequent analysis will show.

Although we are only interested in the two-channel case, MQDT is constructed to deal with an arbitrary number of quasi-bound and continuum states. The complete modified wavefunction for the Rydberg electron in the general case of \mathcal{N}_b bound states and \mathcal{N}_c continuum states is

$$\Psi = \sum_{i=1}^{N_b} A_i \psi_i + \sum_{j=1}^{N_c} B_j \psi_j . \quad (2.8)$$

Each function ψ_i above is defined as

$$\psi_i[r] = \frac{1}{r} \chi_i \phi_i[r]. \quad (2.9)$$

The function χ_i is essentially a bookkeeping function, keeping track of the total wavefunction of the ionic core, as well as the angular wave function of the Rydberg electron. The function $\phi_i[r]$ is a phase shifted version of Equation (2.3)

$$\phi_i[r] = f[r, \ell, \mathcal{E}_i] \text{Cos}[\pi \nu_i] + g[r, \ell, \mathcal{E}_i] \text{sin}[\pi \nu_i], \quad (2.10)$$

with f and g defined as

$$\begin{pmatrix} f \\ g \end{pmatrix} = \begin{pmatrix} \text{Cos}[\pi \delta_i] & -\text{Sin}[\pi \delta_i] \\ \text{Sin}[\pi \delta_i] & \text{Cos}[\pi \delta_i] \end{pmatrix} \begin{pmatrix} f \\ g \end{pmatrix}. \quad (2.11)$$

The ν_i are the effective principle quantum numbers, defined as

$$\nu_i \equiv \frac{1}{\sqrt{-2 \mathcal{E}_i}}, \quad (2.12)$$

The δ_i are the quantum defects for a given channel. The phase-shifted functions f and g differ from f and g in that near the origin, instead of being regular or irregular, they have a phase shift relative to hydrogen of $\pi \delta_i$ or $\pi(\delta_i + \frac{1}{2})$, respectively. [20,22]

An alternative representation of the total Rydberg wavefunction can be constructed in terms of the normal modes of scattering from the core (wavefunctions that change, upon scattering, by at most a phase shift). The coefficients A_i are determined by requiring these two representations to be equivalent.[23]

Following Cooke and Cromer, the calculation of the A_i can be reduced to finding the "energies" of an equivalent $\mathcal{N}_c + \mathcal{N}_b$ level pseudo-Hamiltonian, \mathbf{R}' . Partitioning \mathbf{R}' by the nature (bound or continuum) of the states it mixes together, we have

$$\begin{pmatrix} (\mathbf{R}')_{bb} + \text{Tan}[\pi \nu'] & (\mathbf{R}')_{bc} \\ (\mathbf{R}')_{cb} & (\mathbf{R}')_{cc} + \text{Tan}[\pi \nu'] \end{pmatrix} \mathbf{a} = \mathbf{0} . \quad (2.13)$$

The major simplification is in the use of the ν_i' and α_i :

$$\nu_i' \equiv \nu_i + \delta_i, \quad (2.14)$$

$$\alpha_i \equiv A_i \text{Cos}[\pi \nu_i'], \quad (2.15)$$

and the phase-shifted functions f and g . Since the δ_i contain all of the core-screening "information", the matrix \mathbf{R}' contains only channel-mixing information -- in other words, only the off-diagonal elements are non-zero.

For the two channel case of interest to us, we have

$$\begin{pmatrix} \text{Tan}[\pi \nu_1'] & R_{12} \\ R_{12}^* & \text{Tan}[\pi \nu_2'] \end{pmatrix} \mathbf{a} = \mathbf{0} \quad (2.16)$$

The condition for a non-trivial solution to our problem is that the determinant of \mathbf{R}' must vanish. This results in the requirement that

$$\text{Tan}[\pi \nu_1'] \text{Tan}[\pi \nu_2'] = |R_{12}|^2. \quad (2.17)$$

Our next step is to rewrite Equation (2.16) as a pair of equations

$$A_1 = -A_2 R_{12} \frac{\text{Cos}[\pi \nu_2']}{\text{Sin}[\pi \nu_1']} \quad (2.18)$$

and

$$A_1 = -A_2 \frac{\text{Sin}[\pi \nu_2']}{R_{12}^* \text{Cos}[\pi \nu_1']}. \quad (2.19)$$

Multiplying the complex conjugate of the second equation by the first yields

$$|A_1|^2 = \frac{|A_2|^2 \text{Sin}[2\pi \nu_2']}{\text{Sin}[2\pi \nu_1']} \quad (2.20)$$

Without loss of generality, we set the continuum state coefficient to be unity

$$|A_2|^2 = 1, \quad (2.21)$$

and simplify our expression with trigonometric reduction identities

$$|A_1|^2 = \frac{\text{Tan}[\pi \nu_2']}{1 + \text{Tan}[\pi \nu_2']^2} \frac{1 + \text{Tan}[\pi \nu_1']^2}{\text{Tan}[\pi \nu_1']}. \quad (2.22)$$

All of the terms involving ν_2' are of the form $\text{Tan}[\pi \nu_2']$. Equation (2.17) allows us to eliminate these terms in favor of the bound-continuum coupling constant and ν_1' .

$$|A_1|^2 = \frac{|R_{12}|^2}{1 + \frac{|R_{12}|^4}{\tan[\pi \nu_1']^2}} \frac{1 + \tan[\pi \nu_1']^2}{\tan[\pi \nu_1']} \quad (2.23)$$

$$|A_1|^2 = \frac{|R_{12}|^2 (1 + \tan[\pi \nu_1']^2)}{|R_{12}|^4 + \tan[\pi \nu_1']^2} \quad (2.24)$$

We can recast this in a more symmetric form if we write

$$|A_1|^2 = -i \tan\left[i\pi \frac{\gamma}{2}\right] \frac{1 + i \tan[\pi \nu_1']}{\tan[\pi \nu_1'] + \tan\left[i\pi \frac{\gamma}{2}\right]} \frac{1 - i \tan[\pi \nu_1']}{\tan[\pi \nu_1'] - \tan\left[i\pi \frac{\gamma}{2}\right]}, \quad (2.25)$$

where we have implicitly defined γ using

$$\tan\left[i\pi \frac{\gamma}{2}\right] \equiv i |R_{12}|^2. \quad (2.26)$$

From the definition of Tangent, and De Moivre's theorem, we find

$$|A_1|^2 = \frac{-i \sin\left[i\pi \frac{\gamma}{2}\right]}{e^{i\pi \nu_1}} \frac{\cos\left[i\pi \frac{\gamma}{2}\right] \sin[\pi \nu_1'] + \sin\left[i\pi \frac{\gamma}{2}\right] \cos[\pi \nu_1']}{e^{-i\pi \nu_1}} \frac{1}{\cos\left[i\pi \frac{\gamma}{2}\right] \sin[\pi \nu_1'] - \sin\left[i\pi \frac{\gamma}{2}\right] \cos[\pi \nu_1']} \quad (2.27)$$

and finally,

$$|A_1|^2 = \left| \frac{\sqrt{\sinh\left[\pi \frac{\gamma}{2}\right]}}{\sin\left[\pi\left(\nu_1' + i \frac{\gamma}{2}\right)\right]} \right|^2. \quad (2.28)$$

The end result, in our two-channel case, is that a given autoionizing state, suppressing all but the radial wavefunction, labeled now by the Rydberg electron's effective quantum ν , is represented as

$$\Psi_\nu = A_\nu \phi_\nu + e^{i\alpha} \phi_c, \quad (2.29)$$

where

$$A_\nu = \frac{\sqrt{\text{Sinh}[\pi\gamma/2]}}{\text{Sin}[\pi(\nu + \delta + i\frac{\gamma}{2})]}, \quad (2.30)$$

and α is an undetermined real phase.

In figure (2.2) below, we plot $|A_\nu|^2$ for $\gamma = 0.21$, $\delta = -0.19$, for $\nu \simeq 30$. Note that large resonances (spikes) occur whenever $\nu + \delta =$ an integer, and are therefore evenly spaced.

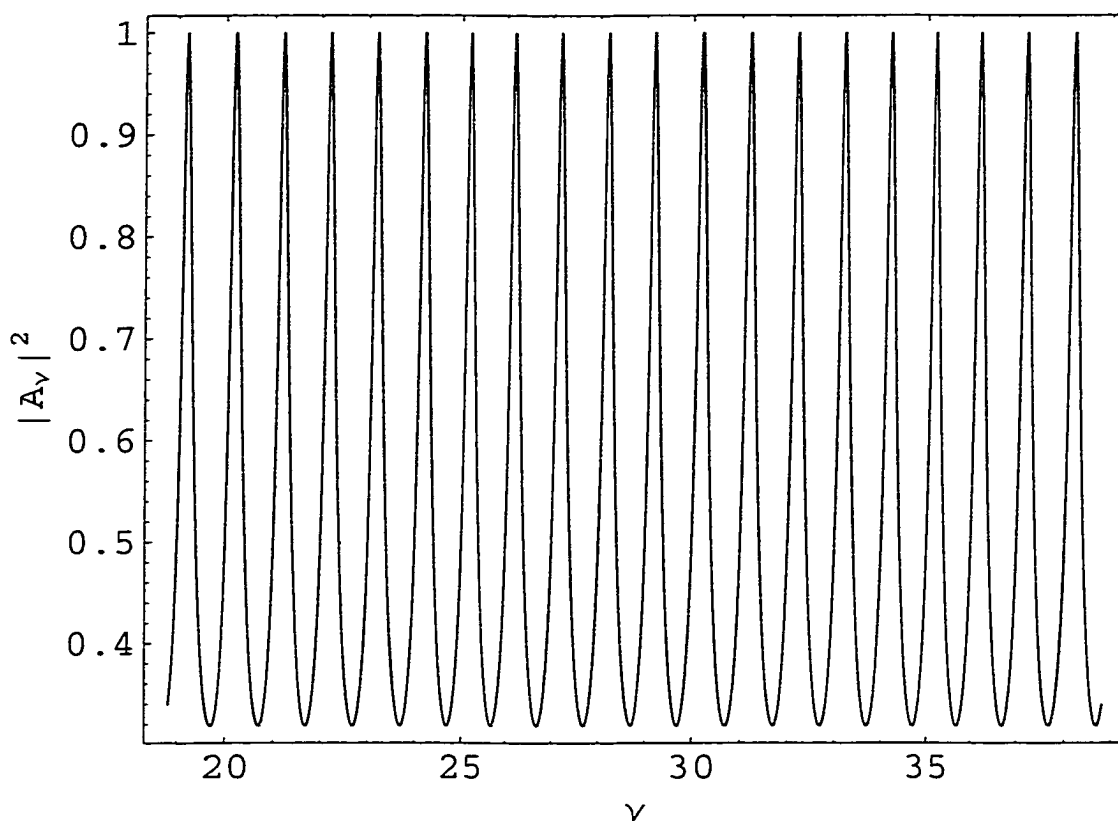


Figure 2.2

The spectral density, $|A_\nu|^2$. This function gives the amount of autoionizing character in a given state ν , and is a maximum when $\nu + \delta$ takes on an integer value.

These are the "spikes" shown in our introduction. However, as we will explain in Chapters 4 and 5, the "important" representation of the spectral density isn't in ν -space, but rather in energy-space. In this representation, the resonances are no longer evenly spaced (their spacing goes roughly like ν^{-3}), becoming infinitely dense as \mathcal{W} approaches 0. For comparison, we have plotted the spectral density as a function of energy in Figure (2.3) below. The numbers across the top of the graph

correspond to the "integer value" of $\nu + \delta$ responsible for a given resonance, and extend over those resonances depicted in Figure (2.2).

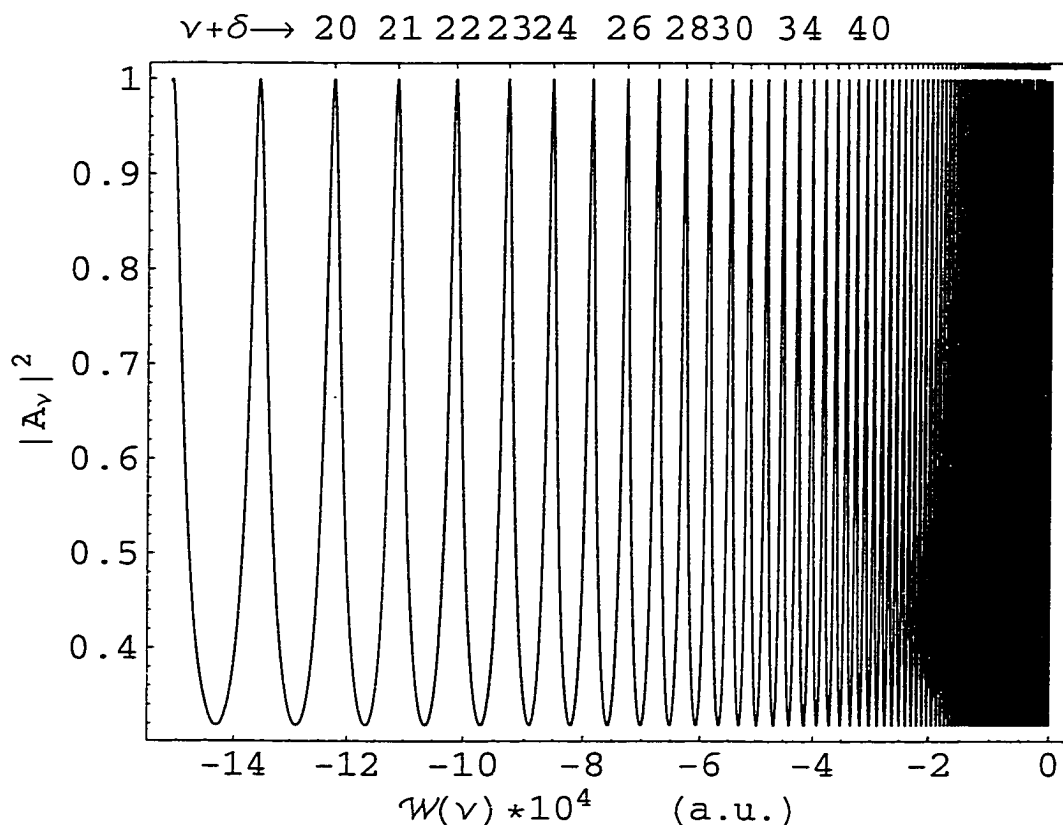


Figure 2.3

The spectral density, $|A_\nu|^2$. This function gives the amount of autoionizing character in a given state ν , and is a maximum when $\nu + \delta$ takes on an integer value. This is the same function as in Figure (2.2), except in this case, it is plotted as a function of energy. Resonant values of $\nu + \delta$ are labeled across the top.

Note that ν is treated as a continuous variable, as the infinite number of quasi-bound states are blurred into a quasi-bound continuum due to the experimentally short lifetimes of these states.[1] The Rydberg wavefunctions ϕ_ν are no longer orthonormal, possessing instead an overlap function defined as[24]

$$O[\nu, n^*] \equiv \int dr r^2 \phi_{\nu}^*[r] \phi_{n^*}[r] = \frac{\text{Sin}[\pi(\nu - n^*)]}{\pi(\mathcal{W}_{\nu} - \mathcal{W}_{n^*})}. \quad (2.31)$$

Under this convention, $O[\nu, \nu] = \nu^3$. If the states are to be normalized to 1 instead, we must multiply each wavefunction by a factor of $\nu^{-3/2}$. The "unit state" normalized overlap function for $n^* \simeq 30$ is displayed in the figure below. Note that $O[\nu, n^*] = 0$ for $\nu - n^* = \text{Integer}$.

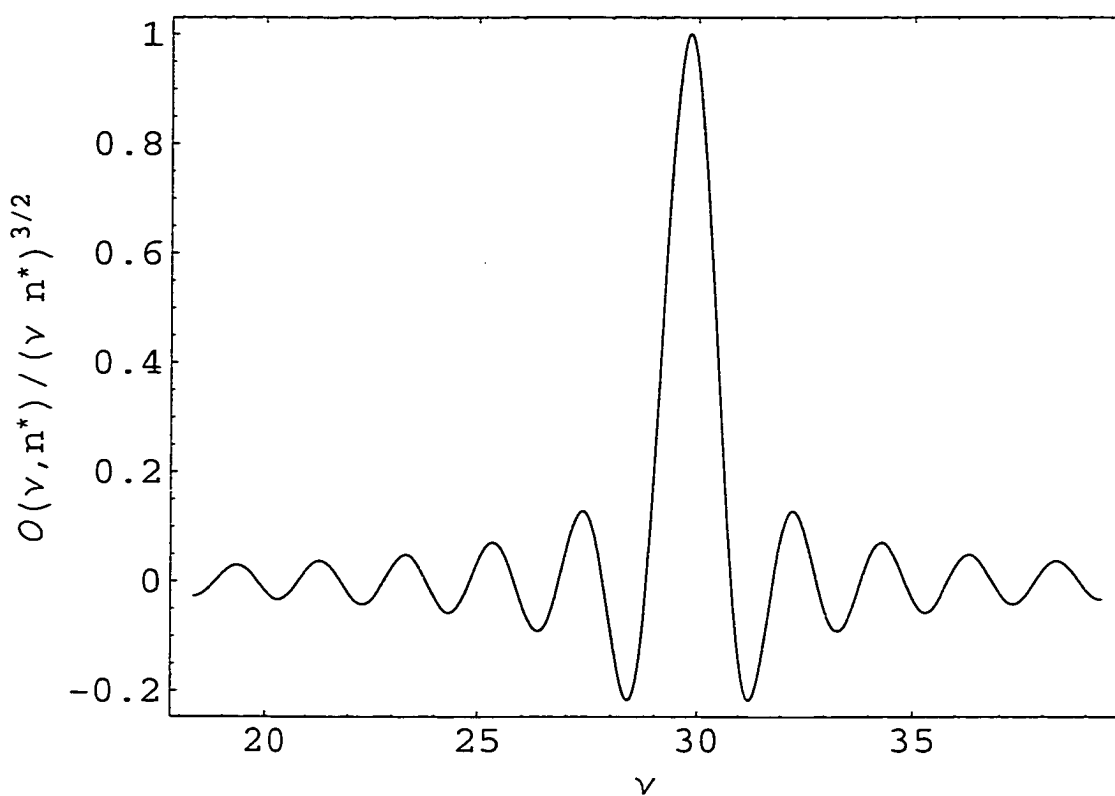


Figure 2.4

The overlap function $\alpha(\nu, n^*)$ normalized by $(\nu n^*)^{3/2}$, for $n = 31$. This function is maximal when ν and n^* differ by zero or a half-integer, and vanishes when they differ by an integer.

In the beginning of this section, we claimed that the parameters of Cooke and Cromer's MQDT formulation were easily extracted from spectroscopic data. As an example, we present a sample data set (see

Figure (2.5), below) from a spectroscopic study of Calcium undertaken by R. R. Jones. [25,26] This data set was produced using the ICE technique to drive $4s\ 25d \rightarrow 4p_{3/2}\ 25d$ transition. The amplitude for the process depends simply on the overlap between the initial and final states,

$$\text{Amplitude}_{\text{ICE}} \propto A_\nu O(\nu, n^*), \quad (2.32)$$

so that the ICE Cross Section is proportional to $|A_\nu|^2 O(\nu, n^*)^2$.

Pictorially, this means that we expect the cross section to look like the Figure (2.3) multiplied by the square of Figure (2.4).

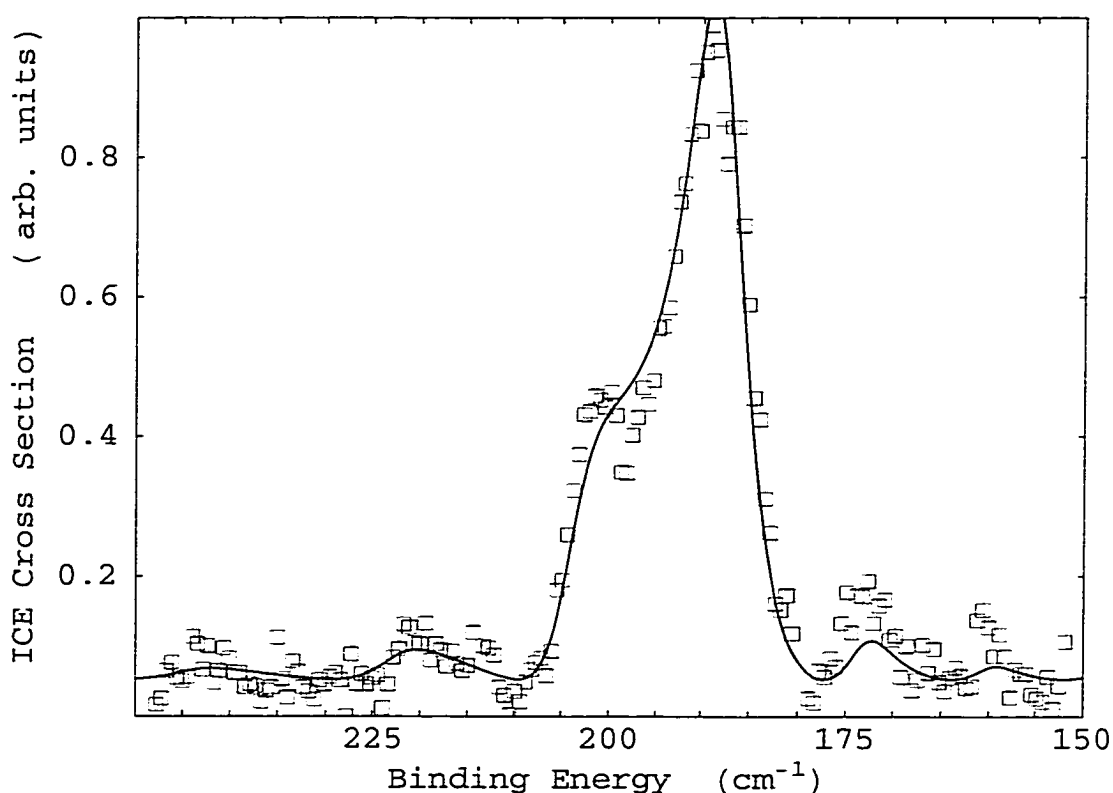


Figure 2.5

ICE Cross Section data of R. R. Jones, Phys. Rev. A 57, 446 (1998). The boxes are experimental measurements, while the line is a fit to $|A_\nu|^2 O(\nu, n^*)^2$ for $n = 25$ in Calcium. The fit parameters were $\gamma = 0.41$, and $\delta = -0.19$.

The fitting of the theory to the data is also easy to understand from a pictorial point of view. The overlap function acts as a filter on the spectral density -- only those "spikes" near the central peak of $O(\nu, n^*)$ are seen. Adjusting the value of δ shifts the "spikes" back and forth across the central peak. The location of the central peak in $O(\nu, n^*)$ is determined by $n^* = n - \delta_n$ (n is the principle quantum number, and δ_n is the quantum defect of the initial state). Given the periodic nature of the spectral density, the value for δ is only determined modulo 1, or any other integer. This being the case, the location of the maxima in ICE spectra are determined by the *difference between the quantum defects of the initial and final states*.

Traditionally, ICE spectra have been fit using the Tangent form of the spectral density given in Equation (2.24). [20,25,26 for example] For this form, assuming values of $R_{1,2} \ll 1$, it is easy to show that the spectral density can be approximated by a Lorentzian,

$$\left| A_\nu \right|^2 \simeq \frac{|R_{12}|^2}{|R_{12}|^4 + (\pi \nu_1')^2}, \quad (2.33)$$

with the FWHM given by

$$\text{FWHM} = \frac{2 |R_{12}|^2}{\pi}. \quad (2.34)$$

If the condition $R_{1,2} \ll 1$ holds, then the spikes of the spectral density are much narrower than the central peak of the overlap function.

Consequently, the width of the central "spike" , Γ , is largely unaffected by $O(\nu, n^*)$, so that R_{12} can be directly determined using

$$\Gamma = \frac{2 |R_{12}|^2}{\pi n^{*3}}. \quad (2.35)$$

The n^{*3} factor appearing in the last Equation arises from the transition from ν -space to energy-space.

Even when the small - R_{12} condition is not met, $R_{1,2}$ is still related to the widths of the ICE spectra peaks, so that pictorially, it is these widths that are being adjusted when one fits for R_{12} (or in our case, γ).

The exact relationship between γ and the widths of the "spikes" in the spectral density is more readily determined from the Csc form of A_ν that we use in this work. Consider the related function

$$f[z] \equiv \frac{1}{\text{Sin}[\pi(z + i \frac{\gamma}{2})]} \frac{1}{\text{Sin}[\pi(z - i \frac{\gamma}{2})]}. \quad (2.36)$$

Using Mittag-Leffler's expansion theorem[40], we can write

$$f[z] = f[0] + \sum_{n=1}^{\infty} b_n \left(\frac{1}{z - a_n} + \frac{1}{a_n} \right), \quad (2.37)$$

where the a_n are the simple poles (and only singularities) of $f[z]$, and the b_n are the residues of $f[z]$ at these points. For our $f[z]$, we have poles at $z = k \pm i \frac{\gamma}{2}$, with corresponding residues of $\mp \frac{i}{\pi} \text{Csch}[\pi \gamma]$ (k is an integer of either sign). Thus, we write

$$\begin{aligned}
f[z] &= \operatorname{Csch}\left[\pi \frac{\gamma}{2}\right]^2 + \\
&\frac{i}{\pi} \operatorname{Csch}[\pi \gamma] \sum_{k=-\infty}^{\infty} \left(\frac{1}{z - (k - i \frac{\gamma}{2})} + \frac{1}{(k - i \frac{\gamma}{2})} \right) - \\
&\frac{i}{\pi} \operatorname{Csch}[\pi \gamma] \sum_{k=-\infty}^{\infty} \left(\frac{1}{z - (k + i \frac{\gamma}{2})} + \frac{1}{(k + i \frac{\gamma}{2})} \right).
\end{aligned} \tag{2.38}$$

Rearranging terms in our sum gives

$$\begin{aligned}
f[z] &= \operatorname{Csch}\left[\pi \frac{\gamma}{2}\right]^2 + \\
&\frac{i}{\pi} \operatorname{Csch}[\pi \gamma] \sum_{k=-\infty}^{\infty} \left(\frac{1}{z - (k - i \frac{\gamma}{2})} - \frac{1}{z - (k + i \frac{\gamma}{2})} \right) + \\
&\frac{i}{\pi} \operatorname{Csch}[\pi \gamma] \sum_{k=-\infty}^{\infty} \left(\frac{1}{(k - i \frac{\gamma}{2})} - \frac{1}{(k + i \frac{\gamma}{2})} \right),
\end{aligned} \tag{2.39}$$

but these are just sums of complex conjugates, so we can write $f[z]$ as an entirely real function,

$$\begin{aligned}
f[z] &= \operatorname{Csch}\left[\pi \frac{\gamma}{2}\right]^2 + \frac{\gamma}{\pi} \operatorname{Csch}[\pi \gamma] \sum_{k=-\infty}^{\infty} \left(\frac{1}{(k - z)^2 + (\frac{\gamma}{2})^2} \right) \\
&- \frac{1}{\pi} \operatorname{Csch}[\pi \gamma] \sum_{k=-\infty}^{\infty} \frac{4 \gamma}{4 k^2 + \gamma^2}.
\end{aligned} \tag{2.40}$$

The sum in the last term on the right-hand side of this expression is proportional to $\operatorname{Coth}[\pi \frac{\gamma}{2}]$, so that the last term and the first term cancel each other. Comparing our initial and final expressions for $f[z]$ (Equations (2.33) and (2.37)), we see that it is possible to express the

spectral density as an infinite sum of Lorentzians -- each with a FWHM of γ .

$$|A_\nu|^2 = \left| \frac{\sqrt{\text{Sinh}[\pi \frac{\gamma}{2}]} }{\text{Sin}[\pi(\nu + \delta + i \frac{\gamma}{2})]} \right|^2 = \text{sech}[\pi \frac{\gamma}{2}] \sum_{k=-\infty}^{\infty} \frac{\frac{\gamma}{2\pi}}{(\nu + \delta - k)^2 + (\frac{\gamma}{2})^2} \quad (2.41)$$

If we write $\nu = \frac{1}{\sqrt{-2\mathcal{W}}}$, we can approximate the spectral density in energy-space as

$$|A_\nu|^2 = \text{sech}[\pi \frac{\gamma}{2}] \sum_{k=-\infty}^{\infty} \frac{1}{(k - \delta)^3} \frac{\frac{\gamma}{2\pi(k-\delta)^3}}{(\mathcal{W} + \frac{1}{2(k-\delta)^2})^2 + (\frac{\gamma}{2(k-\delta)^3})^2}. \quad (2.42)$$

Since $O(\nu, n^*)$ restricts the contributions from A_ν to only those "spikes" near n^* , we find that in practice, we can replace the infinite sum in the equations above with a finite sum over a small number of k -values near n^* . In the series of plots collected below, we calculate the ICE cross section, and show its development as we increase the number of Lorentzians used.

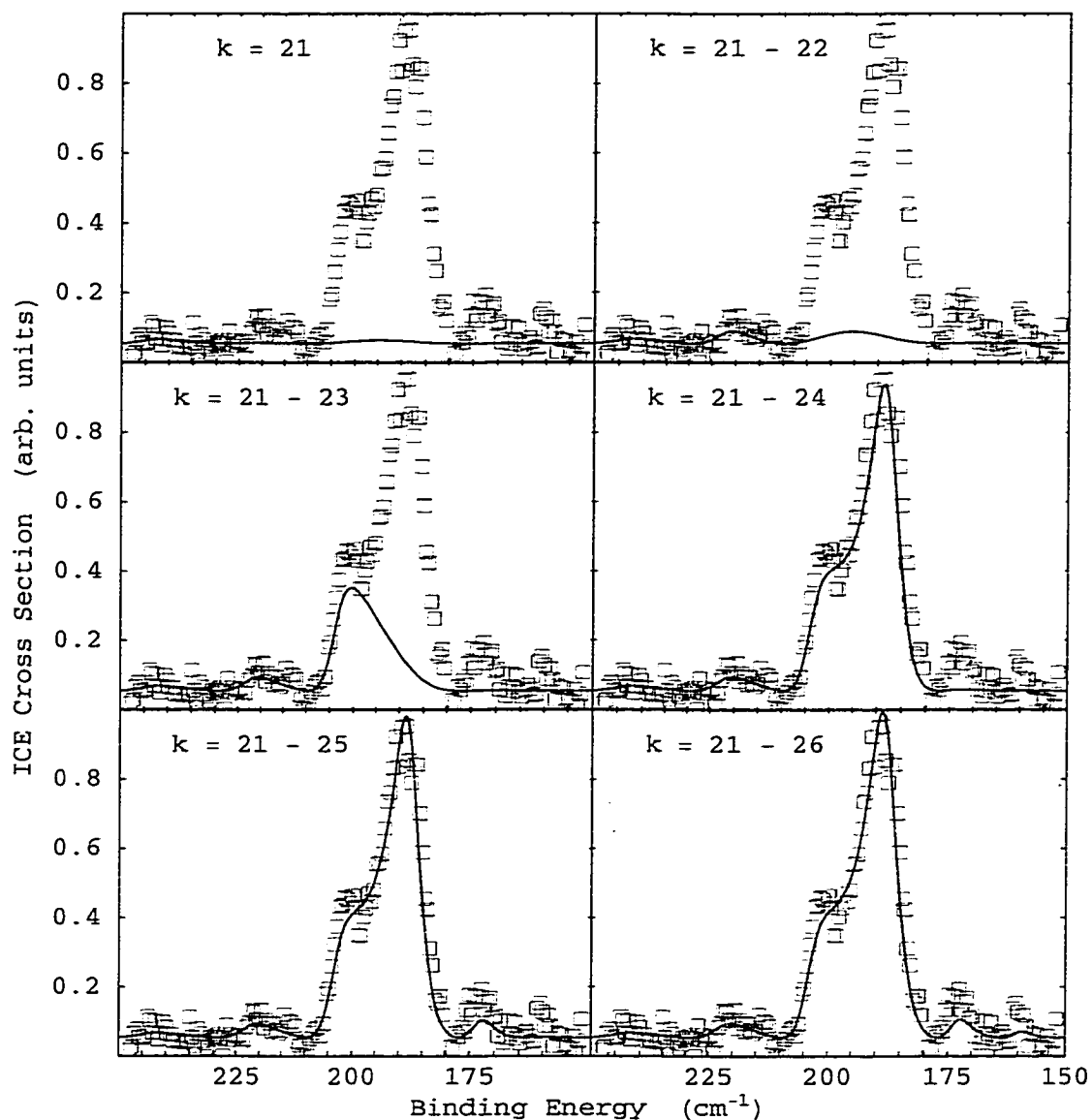


Figure 2.6

ICE Cross Section data of R. R. Jones, Phys. Rev. A 57, 446 (1998). The boxes are experimental measurements, while the line is a fit to the Lorentzian form of $|A_n|^2$, multiplied by $O(\nu, n^*)^2$ for $n = 25$ in Calcium. In the upper left-hand corner of each plot, the Lorentzians included in the fit are indicated. Six terms are required to represent this data. The fit parameters were $\gamma = 0.41$, and $\delta = -0.19$.

The simple relationship of Equation (2.35) between the width of the central peak and $R_{1,2}$ is clearly not applicable in this case, as the fit

parameter $\gamma = 0.41$ produces a large $R_{1,2}$ value of 0.75. The figures above serve to illustrate *why or how* this relationship breaks down.

For small values of γ , the individual Lorentzians in Equation (2.41) and Equation (2.42) are essentially well separated from each other. In those circumstances, Equation (2.35) follows easily from width of the central "peak" of Equation (2.42).

For larger values of γ however, these Lorentzians overlap each other. This is most pronounced in the middle two "frames" of Figure (2.6). The physical width of the central ICE peak is now determined by a combination of the widths of the peaks labeled by $k = 23$ and $k = 24$. Furthermore, the overlap function changes significantly over the course of two peaks, so there is no hope left for a simple relationship.

In summary, it cannot be stressed enough that Cooke and Cromer[20] have presented us with an amazing result *Using MQDT, we are able to modify Rydberg wavefunctions to accurately describe autoionization and autoionizing states. This is accomplished by parameterizing the small- r interactions responsible for bound channel mixing and autoionization into a small number of energy independent parameters. Remarkably, no precise knowledge of the small- r interactions (or the wavefunction in this region) is required.*

Chapter 3

Experimental Methods and Apparatus

In this section we first present a brief sketch of our experimental procedure for shock-wavepacket (SWP) creation and detection, followed by a more detailed description of the various apparatus used throughout the process.

Using a narrow-band ($\sim 0.5 \text{ cm}^{-1}$), Hansch style, dye laser ($\lambda = 423 \text{ nm}$), Calcium atoms in an effusive beam are excited from their $4s4s \ ^1S_0$ ground state to an intermediate $4s4p \ ^1P_1$ state. A second, similar dye laser ($\lambda \approx 393 \text{ nm}$) promotes the $4p$ electron to a highly excited $4snd$ Rydberg state. This stage of the excitation scheme, along with all subsequent steps, is shown in Figure (3.1) on the next page. Both nsec dye lasers have a sufficiently narrow band-width to ensure that the Rydberg electron is in a single- n eigenstate. This singly excited Rydberg state is the starting point for our shock-wavepacket experiment. Before proceeding, we wait for approximately 50 nsec. The delay is much larger than the lifetime of the $4s4p$ intermediate state ($\tau \approx 3 \text{ nsec}$), and ensures that any electrons not transferred to the $4snd$ Rydberg state have returned to the ground state. This consideration is important, as

the short-pulse laser used to create the shock-wavepacket could also transfer population from the intermediate state to a number of Rydberg states.

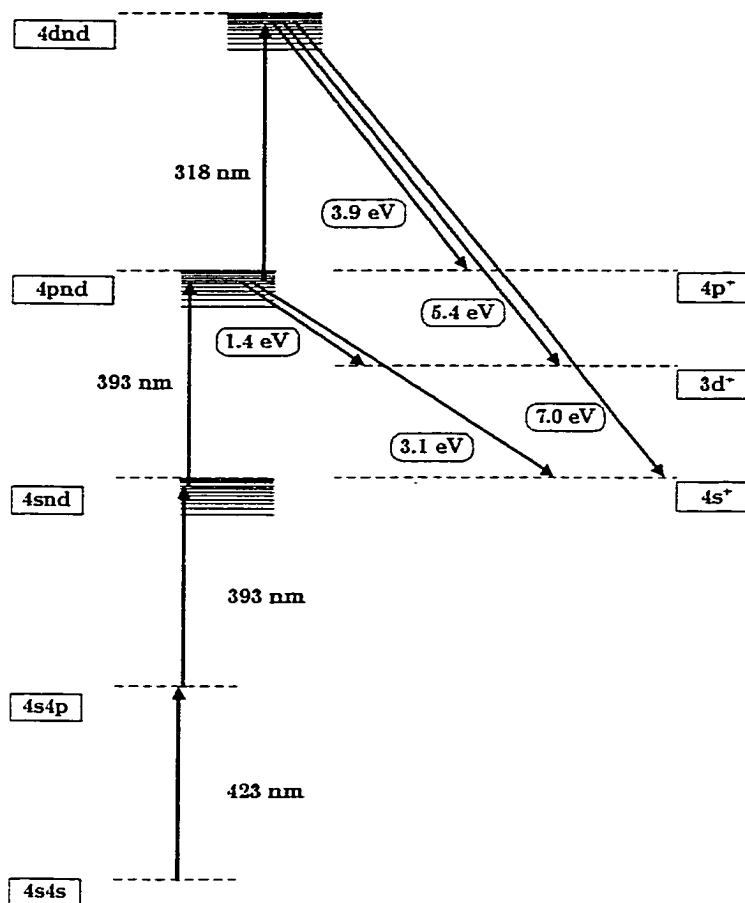


Figure 3.1

Excitation scheme for the Shock-wavepacket experiment in Ca. Two nsec dye lasers are used to excite a valence e^- of Ca into a Rydberg state. An ultra-fast Isolated Core Excitation (ICE) promotes the remaining valence e^- from the 4s to the 4p state, and autoionization of the Rydberg e^- follows. A second ICE (as described in the text) is used to monitor the time dependence of the autoionization process. Excitations are shown as ascending arrows. Each possible decay is depicted by a downward arrow to the final ionic state of Ca^+ , with the energy of the continuum e^- noted at its left.

The ultra-fast output from a chirped-pulse amplified, self-mode-locked, Ti:Sapphire oscillator ($\lambda \approx 787 \text{ nm}$) is split into two separate beams (Figure (3.2)). The first beam (SP1) is frequency doubled ($\lambda \approx 393 \text{ nm}$) in

a 1mm thick, beta barium borate (BBO) crystal, and used to drive the isolated core transition $4s\ n\ d \rightarrow 4p_{3/2}\ n\ d$. A portion of the second beam is similarly doubled, and used to pump an optical parametric amplifier (OPA). The remainder of the second beam is summed with the output of the OPA ($\lambda \approx 534\ \text{nm}$) in a BBO crystal to produce light with a nominal wavelength of 318 nm. The summed short pulse (SP2) is used to drive a second ICE transition, $4p_{3/2}\ n\ d \rightarrow 4d\ n\ d$. The pulse SP1 is used to create the shock-wavepacket, while the pulse SP2 is used to measure the shock-wavepacket's survival probability.

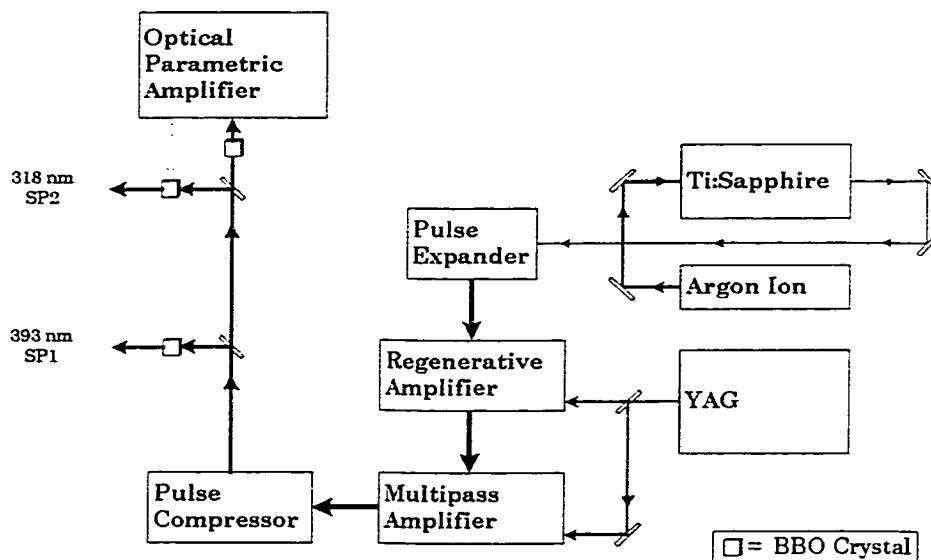


Figure 3.2

Schematic of the ultra-fast laser system used in this experiment. An Argon Ion laser is used to pump a self-mode-locked, Ti:Sapphire oscillator ($\lambda = 787\ \text{nm}$). The output pulses are temporally expanded, amplified in two stages, and compressed again. Part of the light is split off, and doubled to become SP1, the first ICE ($\lambda \approx 393\ \text{nm}$). The rest of the light is also split into two parts. One "branch" is used to pump a white-light seeded, double-pass optical parametric amplifier (OPA). The second "branch" of amplified Ti:Sapphire light is combined with the OPA light ($\lambda \approx 534\ \text{nm}$) in a BBO Crystal to become SP2, the second ICE ($\lambda \approx 318\ \text{nm}$).

The autoionizing electrons resulting from both SP1 and SP2 are monitored using a microchannel plate detector. As can be seen from the excitation scheme (Figure 3.1), all of the electrons leaving the $4p_{3/2}nd$ autoionizing state have a kinetic energy of either 1.4 or 3.1 eV, whereas the electrons leaving the $4dnd$ state have kinetic energies of 3.9, 5.4, and 7.0 eV. This difference in energy suggests a simple scheme for measuring the decay of the SWP. Using a high resolution translation stage, an adjustable delay leg (Figure 3.3) is inserted in the optical path of SP2.

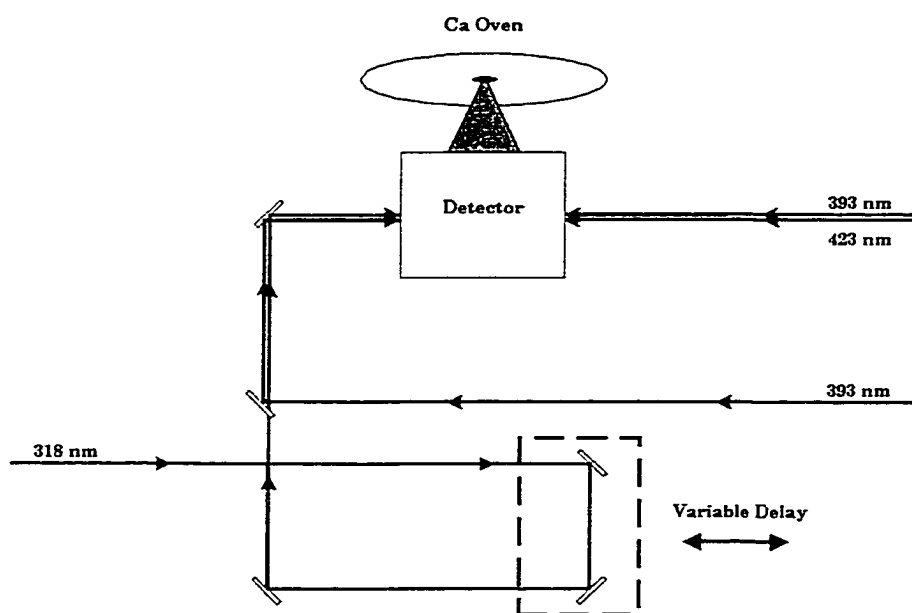


Figure 3.3

The Decay of the Shock-wavepacket is measured using pump-probe techniques. The "pump" beam ($\lambda \approx 393 \text{ nm}$) produces a superposition of autoionizing Rydberg states -- a Shock-wavepacket. The "probe" beam ($\lambda \approx 318 \text{ nm}$) monitors the remaining population as a function of time. The time delay between the two beams is controlled by adjusting a high-precision translation stage. (Also shown: the initial Rydberg states are produced via a two-stage excitation scheme acting on a beam of Ca atoms)

Since both SP1 and SP2 originate from the same Ti:Sapphire pulse, adjusting the path length for SP2 allows one to precisely control their temporal separation to within a small fraction of their pulse lengths. With each pulse SP2, a consistent fraction (nominally 20%) of the remaining $4p_{3/2}nd$ population will be transferred to the $4dnd$ state. Since the electrons autoionizing from the $4dnd$ state have a higher kinetic energy, they will leave the interaction region quicker, and consequently arrive at the MCP detector sooner than their slower $4p_{3/2}nd$ counterparts. Thus, we measure the survival probability for the SWP as a function of time, by "counting" fast electrons as a function of the delay between SP1 and SP2. A weak static field (≈ 1 V/cm) is applied to enhance the resolution between the slow and fast electrons. In Figure (3.4) below, we present two sample oscilloscope traces for $n = 30$. The peaks have been normalized to the same constant so that the maximum peak height in the upper plot is set to 1. The three fast electron peaks are found in the upper plot between 100 ns and 120 ns. These peaks correspond to electrons with kinetic energies of 7.0 eV, 5.4 eV, and 3.9 eV, respectively. We "count" the fast electrons by recording the areas under these peaks.

In both traces, a small peak is also present at an arrival time of roughly 84 ns. The origin and location of this peak are easily understood.

Referring to Figure (3.1), we see that the 393 nm light that drives the $4s4p \rightarrow 4snd$ transition is energetically capable of driving the $4snd \rightarrow 4pnd$ transition as well. Thus, the 84 ns peak is produced by autoionizing electrons ejected from Ca atoms that have absorbed 2 photons of 393 nm light. The location of this peak (relative to the location of our slow electron peak), is a reflection of the delay time that we introduced between the second nsec pulse and the first ICE.

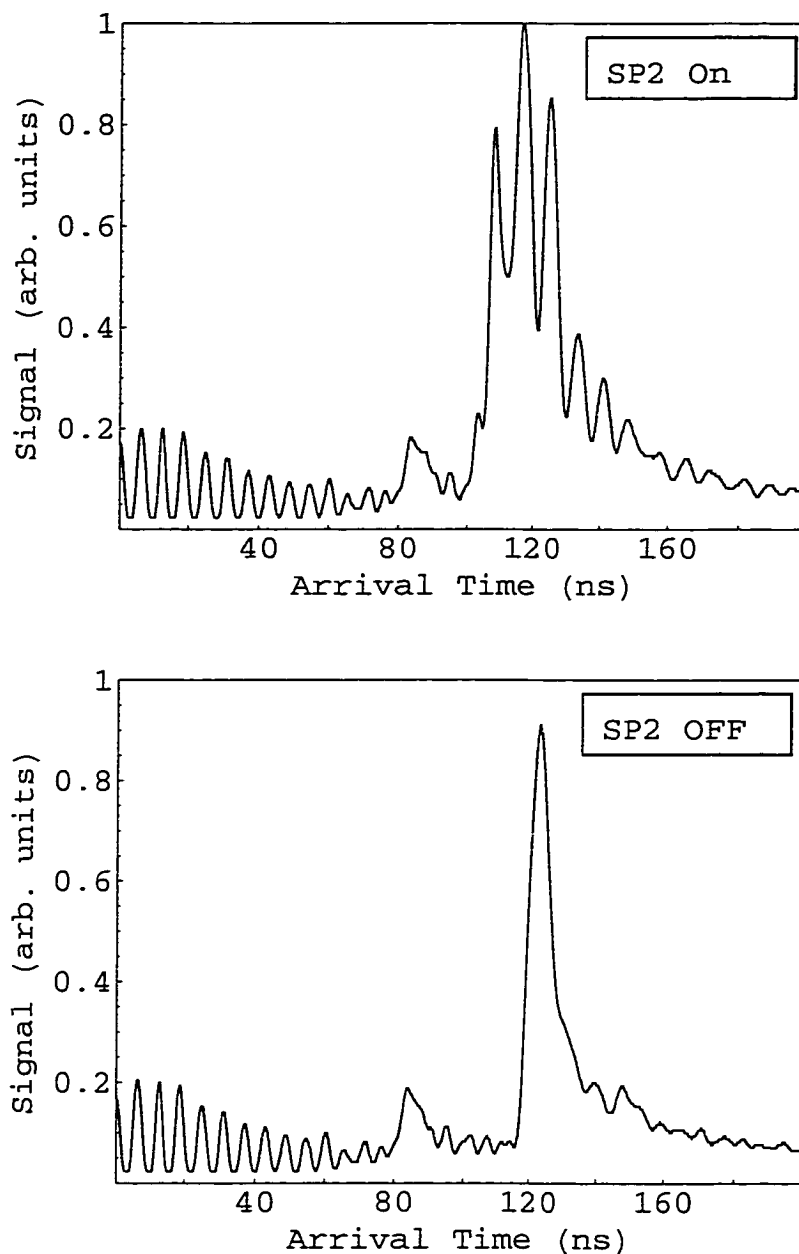


Figure 3.4

Sample traces for $n = 30$. In the lower plot, SP2 is blocked. The large peak at ~ 120 ns is produced by the slow electrons autoionizing from the $4p\ 30d$ state. In the upper plot, SP2 is on, so fast electrons autoionizing from the $4d\ 30d$ state are also detected. The fast electron peaks appear at ~ 102 ns, 108 ns, and 116 ns.

3.1 Vacuum Chamber

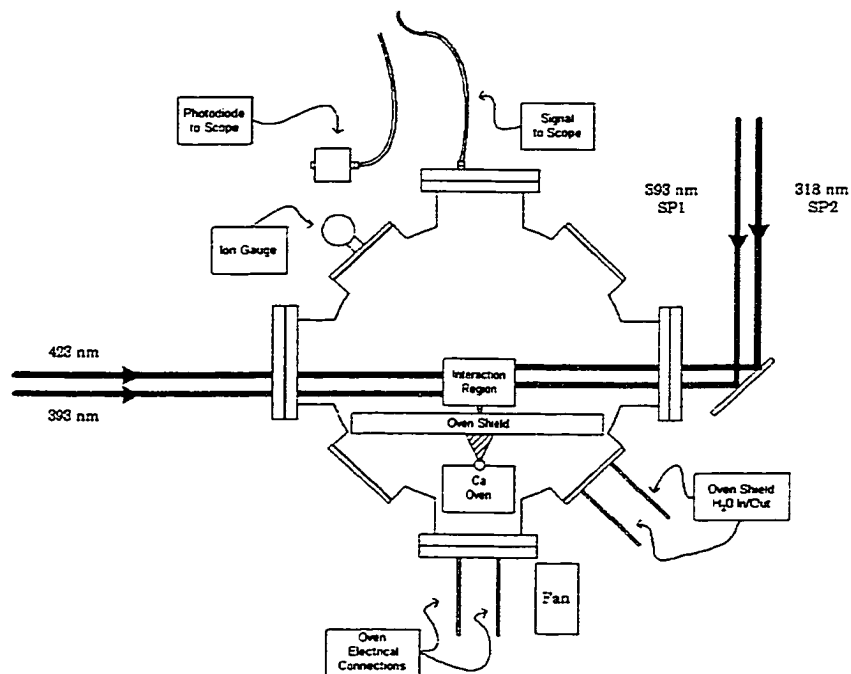


Figure 3.5

Overhead View of the Vacuum Chamber. Made of aluminum, ~ 2ft OD, 1ft deep, the inside of this chamber is maintained at $\sim 5 \times 10^{-7}$ Torr. The Oven and Interaction Region are shown schematically, but the rest of the elements are drawn more or less to scale. For clarity, laser beams are shown on their entrance paths only.

The vacuum chamber in which the lasers and Ca atoms interact is made of aluminum, and is essentially cylindrical in shape (see Figure 3.5). The pressure is monitored with an ionization gauge, and is maintained at $\sim 5 \times 10^{-7}$ Torr by a 6" ID diffusion pump suspended beneath the chamber (the diffusion pump is backed by a Welch 1376 mechanical pump). The chamber contains several windows allowing for both the

entrance and exit of multiple laser beams, as well as visual inspection of the interior.

The interior region of the chamber is divided into two regions: the atomic Ca source (or oven), and the interaction region. Between the two sections is a water-cooled copper heat shield designed to prevent the temperature in the interaction region from rising significantly above 300K.

3.2 Oven

The thermal source of atomic Ca is essentially a small, hollow, stainless steel tube (about the size of a pencil), with a pin-point hole drilled into its side. Our experiments were performed exclusively on Ca, and to that end, the oven is filled up until just beneath the hole with Ca shot. The ends of the tube are crimped and, with the tube in vertical position, held securely in place by clamps at either end. A large current (between 80 and 100 Amps) is run through the tube, raising the temperature of the Ca through resistive heating, and causing the Ca atoms to boil off, exiting the oven as a gas through the center hole. The tubes come in both $\frac{3}{8}$ " and $\frac{1}{4}$ " diameters. We obtained better results with, and generally prefer, the $\frac{1}{4}$ " tubes. It is important to be conservative when picking a current to run at -- larger currents produce more Ca atoms,

3.3 Interaction Region

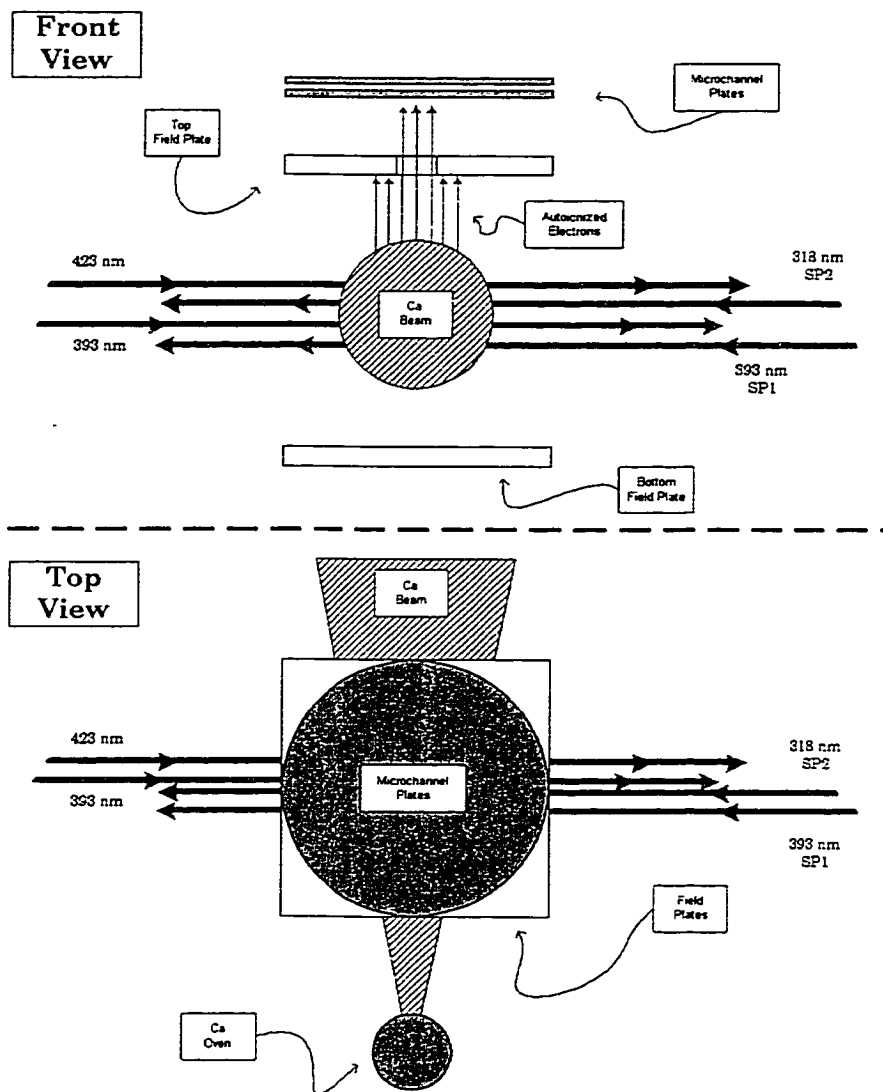
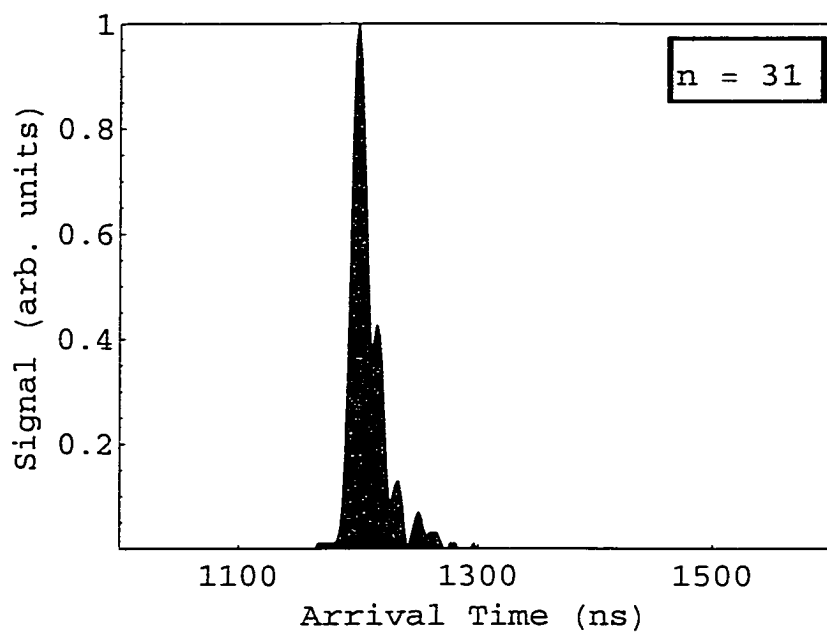


Figure 3.6

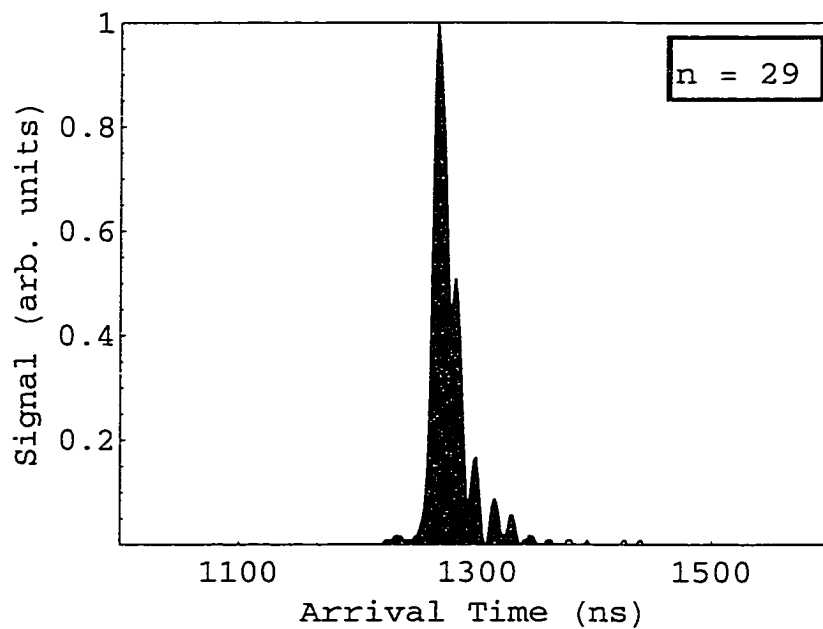
The Interaction Region. Ca atoms in a thermal beam undergo autoionization after a multi-step excitation process. A potential difference of $\sim 1\text{ V}$ is applied between the top and bottom field plates (actual separation between plates is $\sim 1\text{ cm}$). This voltage retards the high-energy electrons, and suppresses some of the low-energy ones. Only those electrons emitted parallel to the polarization of the lasers (i.e., vertically) are detected; for clarity, these are the only ones shown. The electrons are "counted" using a dual multichannel plate detector located above a small hole in the upper field plate. *For clarity, the laser beams have been drawn offset from each other.*

Designed around the small volume in space where the diverging beam of Ca atoms is intersected by multiple laser beams, the Interaction Region is where the Shock-wavepacket experiment actually takes place. The autoionized electrons come into existence between two field plates with a separation of ~ 1 cm. The weak static field mentioned in the first section of this chapter is produced by applying a static voltage of ~ 1 V to the lower plate. The voltage slows down all of the emitted electrons since it reduces their kinetic energy. With speed going like \sqrt{KE} , this has a bigger impact on the lower energy electrons. Those electrons emitted parallel to the lasers' polarization (i.e., vertically) travel through a small hole in the upper plate, impinging upon the first of a set of microchannel plates (MCPs). The MCPs amplify the electron yield signal in a cascade fashion -- each plate producing $\sim 1.2 \times 10^4$ e^- per incident charged particle (although we counted electrons, this apparatus could just as easily be used to count positive ions). The two MCPs in series, biased at 2000V, amplify our signal enough for it to be "seen" on an oscilloscope connected to a stainless steel collection plate behind the second MCP. The arrival times of the electrons are well separated on a 20 nsec/Div time scale, and the high-energy electrons are easily distinguished (refer to Figure 3.4).

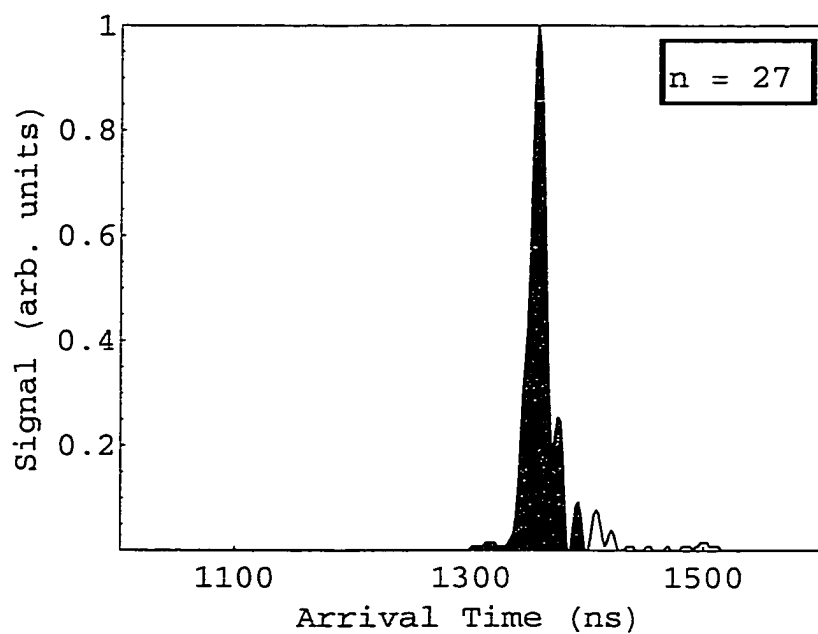
The Field plates can also be used to monitor which Rydberg state we are populating. A relatively long pulse (several μsecs), with an amplitude of $\sim 6000\text{V}$ can be applied to field ionize Rydberg atoms. The electrons thereby produced are detected as before, with the peaks from different n -states easily discernible. This is the technique we used both to identify our initial (pre ICE) Rydberg state, and to verify that these initial states were singly excited. The field ionization signal is so much stronger than that of our SWP experiment, that to prevent our detector from saturating, we needed to reduce the bias voltage by 15%. In the plots below, Figure (3.7) through Figure (3.10), we display sample oscilloscope traces of the field ionization signal in decreasing n order. Note that the arrival times of the peaks increase as n decreases. This is easy to understand: our field ionizing pulse increases with time; since higher n states are easier to ionize, they ionize sooner and consequently arrive sooner than lower n states.

**Figure 3.7**

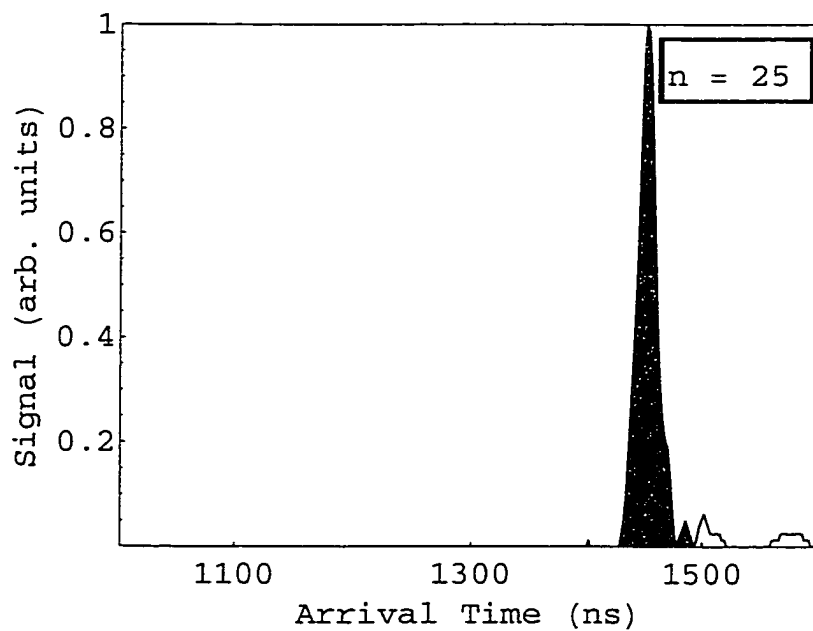
Sample trace of field ionization signal for Ca in the 4s 31d state.

**Figure 3.8**

Sample trace of field ionization signal for Ca in the 4s 29d state.

**Figure 3.9**

Sample trace of field ionization signal for Ca in the $4s\ 27d$ state.

**Figure 3.10**

Sample trace of field ionization signal for Ca in the $4s\ 25d$ state.

3.4 Data Acquisition

The signal from the micro channel plates is cabled directly to a TEKTRONIX 2440 Oscilloscope. The scope is triggered by a photo-diode that picks up some scattered light from the nsec lasers. Once a signal is seen, various machinations ("tuning" of mirrors, adjusting extraction voltages, inserting/adjusting ND filters in the path of the Rydberg laser, etc.) are gone through in an iterative fashion in order to optimize its amplitude and clarity.

All of the data for these experiments are recorded by computer. The oscilloscope is essentially used as a fast A/D converter. As well as being displayed on the scope, the resulting digitized signal is read out by computer through the GPIB interface located in the back of the scope. A powerful yet compact computer program, written by Tom Bensky (a former student in this lab) is used for the actual data acquisition, pre-processing, and recording.

3.5 Dye Lasers

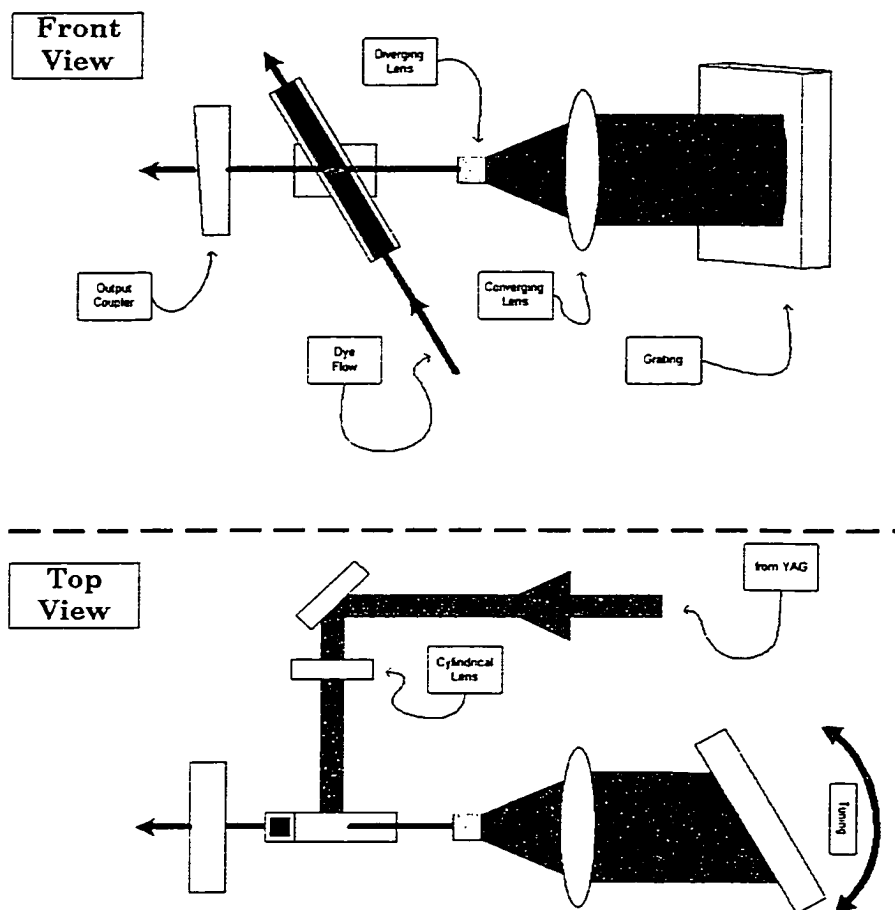


Figure 3.11

Front and Top views of a Hansch-style dye laser. Both dye lasers in our experiment are of this design, and are side-pumped by light from a YAG laser. Tunability is achieved by rotating a grating mounted at the rear of the cavity. The intra-cavity telescope serves to expand the beam thus narrowing the line width while preventing damage to the grating.

Two dye lasers are used in these experiments. The lasing medium in both is an organic compound (dye) dissolved in methanol. The dye is circulated through a quartz cuvet inclined at an angle relative to the optics table. The laser is side-pumped by YAG light focused down

through a cylindrical lens to a line parallel to the optics table about midway through the cuvet. The YAG light causes the dye to fluoresce, sending light in both directions along the cavity. The important light to follow is the light heading for the back of the cavity, where it strikes a grating with an adjustable orientation. Only that light within a fraction of a wavenumber of our desired frequency is reflected back by the grating -- the rest is scattered away. A beam expander (telescope) is inserted between cuvet and grating to increase the number of grating lines "seen" by the beam. On its way to the output coupler, the returning light passes through the dye cell where it stimulates more of the excited, organic, molecules to produce light of the same wavelength, polarization, and phase.

The total path length of the cavity is under a foot long, so that the light traverses it and is amplified several times over the duration of the YAG pulse. A dye laser cavity with these components and geometry is a Hansch-style dye laser[30]

3.6 Argon-Ion Laser

The Argon-Ion laser produces 8.0 W of CW light at 514nm and 488nm. The lasing medium -- i.e. substance in which a population inversion is created -- is an Ar^+ plasma. The Ar^+ ions used for visible light generation are produced when several tens of amperes of electrons are discharged through a sealed tube filled with Argon. The strongest emission lines for this transition scheme are at 514nm and 488nm, and the desired transition can be encouraged through coatings on the cavity mirrors. [31]

The cavity of the Argon laser is designed so that only modes polarized perpendicular to the plane of our optical tables are supported. This is accomplished by sealing the output end of the plasma tube with a quartz crystal window oriented such that the laser light is incident upon the window at Brewster's angle (light polarized parallel to the plane of incidence of the window surface experiences no surface reflection loss). [32]

The sole purpose of the Argon-Ion laser in our lab is to pump the Ti:Sapphire laser. Both "strong" wavelengths of the Argon-Ion fall within the absorption bands of the Ti:Sapphire, so both of these wavelengths are "encouraged" and used.

3.7 Ti-sapphire Laser

The blue-green light of the Argon-ion laser feeds directly into the self mode-locking Ti-sapphire laser. Originally a Spectra-Physics 3900S Ti-sapphire laser designed to operate in CW mode, this laser has been extensively modified by R. R. Jones. The output coupler has been moved forward, outside of the original cavity. The rear mirror has also been moved outside of the casing (with, of course, an additional hole in the back wall to let the beam through). Finally, a pair of prisms has been added before the rear mirror to deal with group velocity dispersion (GVD) effects.[33]

The lasing medium for this solid state laser is a Ti^{3+} -doped sapphire crystal Al_2O_3 , where the Ti^{3+} has replaced some of the Al^{3+} ions. While it is the optically active electrons of Ti^{3+} that are responsible for the lasing, the bulk thermal and optical properties are determined by the Al_2O_3 . [34]

The Ti-sapphire is encouraged to lase in Mode-locked operation by gently wobbling the output coupler [35]. This introduces a brief spike of noise into the laser cavity. As the spike traverses the Ti:Sapphire crystal, its basic shape is unchanged, and it experiences less absorption than the "background" noise of the cavity.[36]

In this mode of operation, the Ti-sapphire produces pulses at 787nm, which are characterized by a repetition rate of 78 MHz (set by the cavity length) and a pulse length of ~100 fs. The bandwidth of a typical pulse is about 150 cm^{-1} (for $\lambda = 787 \text{ nm}$, 150 cm^{-1} corresponds to $\sim 10 \text{ nm}$), and the pulse is assumed to be a transform limited Gaussian.

3.8 Pulse Expander/Compressor

Each pulse that leaves the Ti:Sapphire laser has less than a nanojoule of energy. This is several orders of magnitude too small for us to do our experiment with -- almost the equivalent of trying to sandblast a building by blowing sand through a soda straw. The obvious course of action is to amplify the pulse. This presents a difficulty, however; if we boost the energy of one of our ultra-short pulses by several orders of magnitude, the intensity will increase drastically as well. Intensity is average energy per unit area *per unit time* -- so a 1 μJ pulse lasting for ~ 200 fs will have an intensity **almost 5 orders of magnitude larger** than a nsec pulse with the same energy. High intensity light tends to damage optics -- to attest to this, the author could easily present a collection of mirrors he's damaged with the comparatively low-intensity light of a dye laser. Mirrors are relatively cheap (at this point in time, a good mirror can be found for \$100 or less), the Ti:Sapphire crystals used in the amplification process are far more expensive. Furthermore, as an intense pulse propagates through a material, nonlinear, intensity dependent effects -- self-lensing and self-phase modulation -- can occur. Self-lensing modifies the spatial profile of the beam, while self-phase modulation changes its spectral profile.[38]

Therefore, before we begin the amplification process, we temporally expand the ultra-short pulse. This high-intensity avoidance strategy is known as Chirped-pulse Amplification. [38] The essence of the technique is to have the pulse scatter from a grating, through a telescope. In first order scattering from a grating, the scattering angle is dependent on the wavelength.[39] This is exploited to introduce a wavelength dependent difference in path-length. The scattered light strikes a second grating inclined at just the right angle to re-collimate the beam. At this point, the pulse is "chirped" -- the components with shorter wavelengths are trailing those with higher ones. In our lab, the expander is composed of one grating, a lens, and two mirrors. The lens serves to shorten the physical path required in order to introduce a significant path-length difference. The first mirror serves to fold the light back upon itself, thus allowing one grating to play the role of two. After reflecting off the grating for a second time, the pulse is *spatially* as well as temporally chirped. The second mirror sends the light back through the grating system, thereby undoing the spatial chirp while increasing the temporal chirp even more. The second mirror is also slightly (and intentionally) misaligned in the vertical direction. This causes the beam to "walk" vertically -- each time it hits the grating on its second pass, it's a little bit higher up. The design is such that after its fourth scattering off the

grating, the significantly elongated pulse walks right out of the expander. After amplification, the pulse is sent through a similar grating-mirror setup -- the compressor -- to reverse the expansion process; leaving us with a $5 \mu\text{J}$, ~ 120 fs pulse.

3.9 Regenerative Amplifier

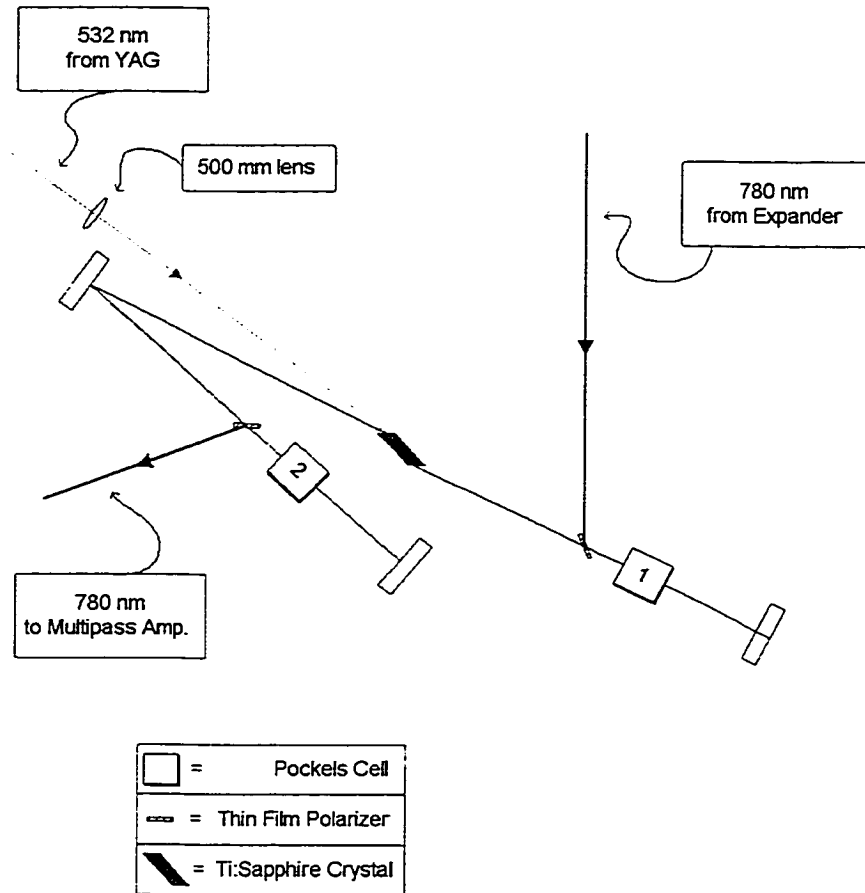


Figure 3.12

The Regenerative Amplifier. PC1 and its adjacent Thin-Film Polarizer (TFP) form a Q-switch mechanism selecting one pulse for amplification every 67ms. After approximately 20 passes, a second Q-switch (PC2 and its TFP) releases the amplified pulse from the cavity.

The Regenerative Amplifier ("Regen") is based around a YAG-pumped, Ti-sapphire crystal. As such, the amplification process is limited by the rep-rate of the YAG to 15 Hz. This means that most of the short pulses we produce get thrown away -- with one pulse being amplified about every 67ms. The mechanism by which a pulse is admitted into the

"Regen", and eventually released is known as a "dual Q-switch". Each Q-switch in this case, consists of a Thin-film Polarizer (TFP) and a Pockels cell. To admit a pulse for amplification, a voltage is applied to the Pockels cell at the entrance to the "Regen" (PC1 in Figure (3.7) above.) When activated, the PC1 rotates the polarization of a pulse passing through it by 45° . After reflection off of the rear mirror, the pulse passes through PC1 again, and emerges with its polarization rotated a total of 90° . At this point, instead of being reflected by the TFP, the pulse passes right through it. With this polarization, the pulse begins to bounce around the cavity, undergoing amplification each time it passes through the Ti:Sapphire crystal. After about 20 passes -- enough to extract a maximal amount of power from the cavity, a voltage is applied to the second Pockels cell (PC2). Two trips through PC2, and the pulse has its original polarization; thus it is reflected out of the cavity when it next encounters the second TFP.

3.10 Multipass Amplifier

The Multi-pass amplifier is essentially a low-tech version of the "Regen". The heart of the multi-pass is, like that of the "Regen", a YAG-pumped, water-cooled Ti:Sapphire crystal. The easiest way to understand the workings of the multi-pass is to think of it as a laser cavity with its end

mirrors purposely misaligned. This "mis-alignment" causes the beam to "walk" slightly on each path (this is the same sort of trick used in the Expander and Compressor). The end result being that after three complete passes the amplified beam exits the cavity.

3.11 Optical Parametric Amplifier

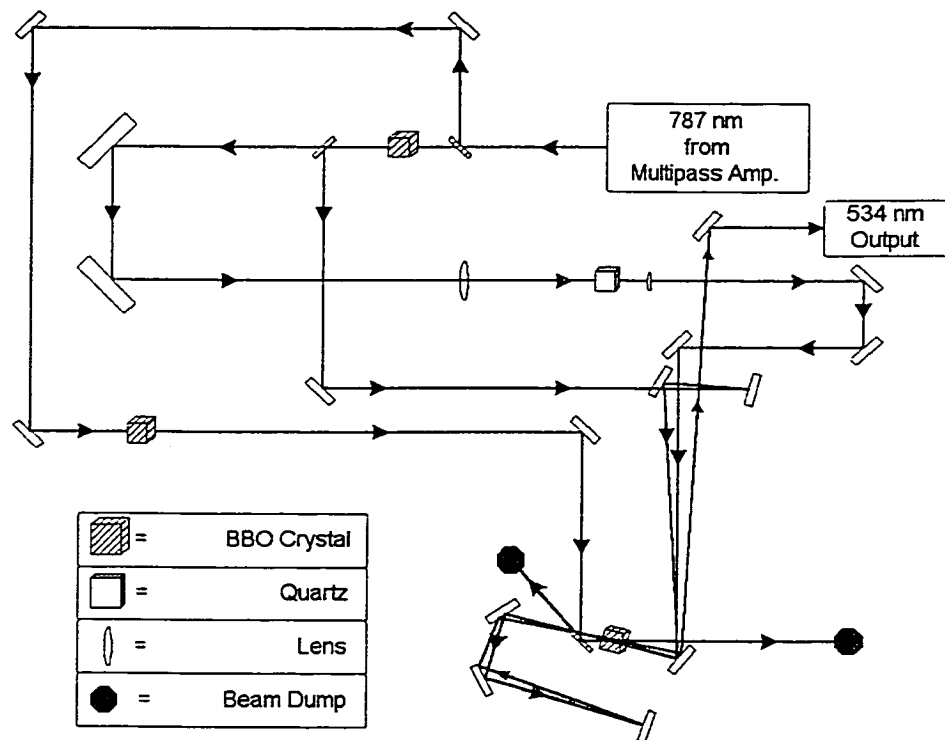


Figure 3.13

Schematic of the Optical Parametric Amplifier. 787 nm light from the chirped-pulse amplified, self mode-locked, Ti:Sapphire laser enters the OPA and is split into two branches. One branch is doubled in a BBO crystal, and then split into two more branches. One of these is focused into a quartz crystal to produce a white-light seed pulse for the OPA. The other passes through a second BBO crystal cotemporally and collinearly with the seed pulse. The remaining branch of 787 nm light is used to amplify the OPA output. Tuning over the visible spectrum is accomplished by turning the second BBO crystal relative to the propagation direction of the doubled light.

At its simplest level, the optical parametric amplifier (OPA) acts like an inverted doubling crystal -- instead of combining two photons in a non-linear crystal to produce one with higher energy, a single high-energy photon is induced to split into two lower energy ones -- the "signal" and the "idler".[43] By adjusting the angle of the BBO crystal relative to the propagation direction of the initial pulse, the output of the OPA can be "tuned" over the entire visible spectrum.

In our lab, the OPA is driven by a portion of the 787 nm light out of the multipass amplifier. Upon entering the OPA, the light is sent through a doubling crystal to produce a beam with $\lambda \approx 393$ nm. A small fraction of the fundamental light is split from the main beam, and focused into a small piece of quartz. This produces "white" light -- an extremely broadband pulse that more than covers the visible spectrum. The white light will act as a "seed" for our signal photons. In other words, the second BBO crystal will be adjusted so that the input 393nm pulse is most efficiently split up into two specific frequencies (the frequencies of the "signal" and "idler" photons mentioned above). The seed light guarantees that photons of the desired frequencies are present in order to start the process off (when the beams are sent through the crystal, they are collinear and cotemporal). Approximately 30% of the light is used for this process. The remaining 70% is sent through the BBO

crystal as the "signal" beam makes a second trip through, and serves to amplify the OPA output.

3.12 YAG Laser

Two YAG lasers (Spectra-Physics GCR's) are used in our setup. One is used to pump the Ti-sapphire crystals in both the Regenerative and the Multi-pass Amplifiers, while the other is used to pump the dye lasers. Like the Ti-Sapphire, the YAG is a solid state laser. The active medium is Neodymium-doped Yttrium Aluminum Garnet, and is the source of this lasers common name: Nd:YAG, or YAG.

A population inversion is achieved via flash lamp optical pumping of the YAG rods. The fundamental frequency of the YAG corresponds to 1064 nm, and lies in the IR region of the optical spectrum. The Spectra-Physics YAG laser has several crystals for generation of higher harmonics, and is capable of producing significant amounts of both 532nm (green) and 354nm (UV) light.

The repetition rate for the YAGs in our lab is 15Hz, and the pulse length is 7-9 ns. Since the Ti-sapphire has a repetition rate of 78 Mhz, the Argon Ion laser is CW, and the effusive beam of Ca atoms is relatively constant, it is the 15Hz Rep rate of the YAG that sets (limits) the rate at which data is taken in these experiments.

3.13 General Lab Environment

3.13.1 Optics Tables

All of our experimental work is performed on a pair of doubled 4"x10" RS3000 optics tables manufactured by the Newport Corp. All experimental equipment: lasers, amplifiers, chambers, pumps and detectors are mounted on, and supported by the tables. The tables are tuned to damp out vibrations, and the entire system is floating on a set of vibration isolators; creating a 4"x20" self stabilizing and leveling surface. The enhanced vibration damping minimizes noise (fluctuations in signals due to very transient, partial mis-alignment of optical components) during data collection. The single, stable surface decreases the amount of alignment drift between optical components occurring during data collection "runs", and from day to day. In other words, damped tables reduce short-term sources of error, while a single stable, floating surface minimizes cumulative effects.

3.13.2 Air Temperature

All of the equipment is surrounded by a canopy of transparent plastic sheets suspended from a ceiling-mounted, overhead shelf. A constant influx of filtered air creates a slight positive pressure under the canopy, thus keeping a significant amount of dust from entering and settling on the optics. A lot of critical optical alignments in the multi-laser and amplifier system are altered by minute temperature dependent expansions/contractions of the optics, optic mounts, and mounting adhesives. A great degree of day-to-day repeatability is achieved, and a large amount of re-alignment time saved, by maintaining a constant temperature within the canopy. In normal operation, the air temperature controller is used to maintain the temperature under the canopy at 75.3° F.

3.13.3 Chilled Water Cooling System

The biggest advantage of pulsed lasers, whether the fsec long, spectrally fat pulses from the ultra-fast system, or the nsec long, spectrally skinny pulses from either of the dye lasers, is their ability to deliver very intense bursts of energy. Thermodynamics dictates that the creation, amplification, and manipulation of these pulses should also produce "large" amounts of heat. If not removed through some sort of cooling system, this heat will alter (for the worse) the physical properties of the various gain media used in these laser systems; thus reducing both stability and power of our laser systems.

The low pressures under which our experiments are performed are generated and maintained by an oil based diffusion pump. Oil vapor from the pump is inhibited from entering the experimental chamber by a water-cooled cold trap. The pump itself is also cooled by water lines coiled about the exterior.

Finally, recall that the source for Ca atoms in these experiments is an "oven" -- a highly resistive stainless steel tube loaded with Ca (see Section 3.2), requiring a large amount of current in order to vaporize the Ca. A water-cooled heat shield is required to prevent the heat from the

oven from damaging the micro-channel plates in the detector, and/or melting the solder on electrical connections in the interaction region.

All of the cooling lines for the lab, excluding those for the Argon-Ion laser, connect up to the chilled water line for the building. The Argon-Ion laser is cooled using a closed-loop Haskris heat exchanger, for which the chilled water line serves as the primary cooling stage. Six ball valves determine water flow and operation of the Heat exchanger. When the lab is shut down, all valves are closed; opening the four exterior valves allows for flow into and out of the heat exchanger. The remaining two ball valves -- which serve to allow or prevent direct exchange of water between the lab lines and the chilled water line -- are left in the closed position during normal operation.

Chapter 4 Shock-Wavepackets

With our experimental and theoretical framework securely in place, we are now ready to present the Shock-Wavepacket analysis of Wang and Cooke[1] as it applies to our system.

A stationary Rydberg electron in calcium is excited to an autoionizing Rydberg wavepacket when the "inner" electron undergoes a sudden, isolated-core excitation. The resulting wavepacket contains a shock wavefront; a localized depletion of probability executing radial excursions. Starting near the core, this wavefront propagates through the radial wavepacket with a period equal to the classical period of the initial Rydberg state.

The concept of an ICE induced shock-wavepacket was first explored by Wang and Cooke[1]. In their formalism, they used a MQDT approach with two channels (one open, one closed). It has been experimentally demonstrated that such a two-channel formalism more than adequately describes the ICE excitation spectra of the $4p_{3/2}nd$ series for $n > 23$. [25, 26] All of our experiments were for $25 \geq n \geq 32$, so we expect that the two-channel approach will allow us to model our results to a sufficient degree of accuracy.

Wang and Cooke argued that the decay rate of the SWP was governed by the absolute square of the Fourier transform of the dipole moment for the transition

$$\mathcal{R}[t] \equiv \left| \int d\mathcal{W}_\nu e^{-i\mathcal{W}t} \mathcal{T}[\mathcal{W}_\nu] \right|^2, \quad (4.1)$$

where

$$\mathcal{T}[\mathcal{W}_\nu] = \frac{\sqrt{\text{Sinh}[\pi\gamma]/2\pi}}{\text{Sin}[\pi(\nu + \delta - i\frac{\gamma}{2})]} \frac{\text{Sin}[\pi(\nu - n^*)]}{\pi(\mathcal{W}_\nu - \mathcal{W}_{n^*})}. \quad (4.2)$$

The effective principle quantum number n^* specifies the initial Rydberg state, while ν is a continuous variable used to index the quasi-bound, autoionizing continuum of final states. The energies of these states are given, respectively, by

$$\mathcal{W}_{n^*} = -\frac{1}{2n^{*2}}, \text{ and } \mathcal{W}_\nu = -\frac{1}{2\nu^2}. \quad (4.3)$$

The first term in $\mathcal{T}[\mathcal{W}_\nu]$ is the MQDT coefficient A_ν , denoting the amount of autoionizing character present in a given final state. The second term is the familiar overlap between the initial and final radial wavefunctions.

As presented above, the decay rate of the SWP corresponds to a truly instantaneous ICE pulse with a correspondingly infinite spectral content. To account for the finite pulse duration, and its accompanying restricted spectral content, we model our ICE pulse as a

transform-limited gaussian with $\text{FWHM}_r = 212$ fs. Our formula for the decay rate is modified to read

$$\mathcal{R}[t] = \left| \int d\omega_\nu e^{-i\omega_\nu t} \mathcal{T}[\omega_\nu] G[\omega_\nu] \right|^2, \quad (4.4)$$

where $G[\omega_\nu]$ is the Fourier transform of the ICE pulse, centered at the frequency corresponding to the $4s\ 4n\ d \rightarrow 4p_{3/2}\ n\ d$ transition.

The probability of finding the electron in the continuum must be the time integral of $\mathcal{R}[t]$, the *rate* at which the wavepacket autoionizes. Since total probability must be conserved, the survival probability for the shock-wavepacket is given as

$$\mathcal{P}[t] = 1 - \int_0^t \mathcal{R}[t] dt. \quad (4.5)$$

Our measured signal will be proportional to the convolution of $\mathcal{P}(t)$ with a Gaussian to account for the finite length of the 2nd ICE pulse:

$$S[t] = \int G[t - \tau] \mathcal{P}[\tau] d\tau \quad (4.6)$$

In the series of plots on the next page (Figure 4.1), we show the decay rate $\mathcal{R}[t]$ as a function of time (measured in units of the Kepler period) for several values of γ .

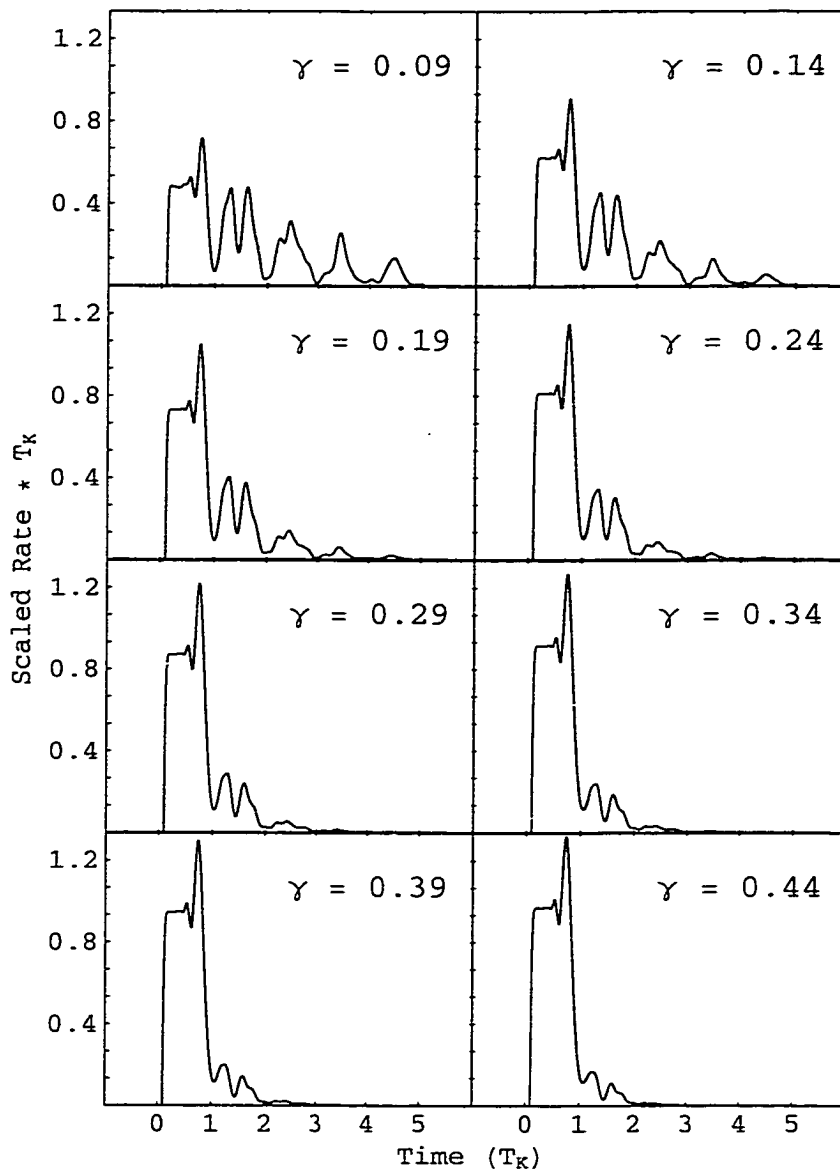


Figure 4.1

Shock-wavepacket decay rate as a function of time for several values of the scaled decay width γ . For larger values of γ , the decay rate is correspondingly larger for the first Kepler period. Since the decay rate depends on the amount of bound-state population present, a larger initial rate results in smaller rates for subsequent periods. The scaled width is related to the bound-continuum coupling via $\gamma \cong \frac{2}{\pi} \text{ArcTanh}[R_{bc}^2]$.

The γ dependence of $\mathcal{R}[t]$ is easy to interpret if we keep in mind that our shock-wavepacket contains a shock-front; starting at the core, moving through the wavepacket and returning to the core after every Kepler period. Qualitatively, the shock-front's behavior is similar to that of the initial cross-sectional "slice" of the "asteroid belt" in the planetary metaphor that we developed in the introduction. Recall now that γ is a measure of the coupling between the "bound" states and the continuum

$$\gamma \equiv \frac{2}{\pi} \text{ArcTanh}[R_{bc}^2] . \quad (4.7)$$

The larger the coupling, the larger the amount of probability initially transferred to the continuum, and hence the larger the rate over the first Kepler period. Since $\mathcal{R}[t]$ determines the amount of probability present in the bound state, the larger the initial value of the rate, the smaller the subsequent rate values will be. In other words, the heights of the remaining peaks decrease with increasing γ . In the planetary picture then, γ would describe how efficient the "inner" belt was at depopulating the "outer" belt. The more asteroids that are knocked out on the first pass, the less that will be around to get knocked out on subsequent orbits. In the array of plots on the next page (Figure 4.2), we exhibit the δ dependence of the decay rate (All curves were calculated assuming a quantum defect for the initial Rydberg state of 1.19). The graphs for

$\delta = 0.0$ and $\delta = -1.0$ are identical, as the value of the quantum defect is only unique Mod 1. The easiest way to understand these plots is to remember our pictorial explanation of ICE spectra presented in the last chapter. The location of the peaks in the ICE cross section were determined by the *differences between the quantum defects of the initial and final states*. Decreasing δ relative to the initial state's quantum defect, shifts the Spectral Density A_ν relative to the overlap function $O(\nu, n^*)$. For the ICE cross sections, this resulted in a translation of the peaks in the spectra. For the integral in Equation (4.1) this results in different weightings for the peaks of A_ν , and hence variations in the rate. After δ has been decreased by 1, the Spectral Density peaks are once again in their initial locations, and the rate is the same as the initial $\mathcal{R}[t]$. Of all these plots, the frame in the lower left most resembles the "stair-step" decay rate of Wang and Cooke that we presented in the introduction.[1] For this frame, the difference between the two quantum defects is most nearly an integer. Unlike the case for Ca, this corresponds to a peak in A_ν falling dead center at the maximum of the overlap function. In the Ca case examined in Chapter 2, δ was found to be -0.2 ; implying a difference in quantum defects of 0.4. This is depicted in the upper right-hand frame of Figure (4.2). Recall from Figure (2.6) that (for Ca) $\delta = -0.2$ resulted in two peaks of A_ν falling under the center

maximum of $O(\nu, n^*)$. Physically, this means that the shock-wavepacket will be dominated by two final states. This effect will be greatest for quantum defect differences of exactly $\frac{1}{2}$.

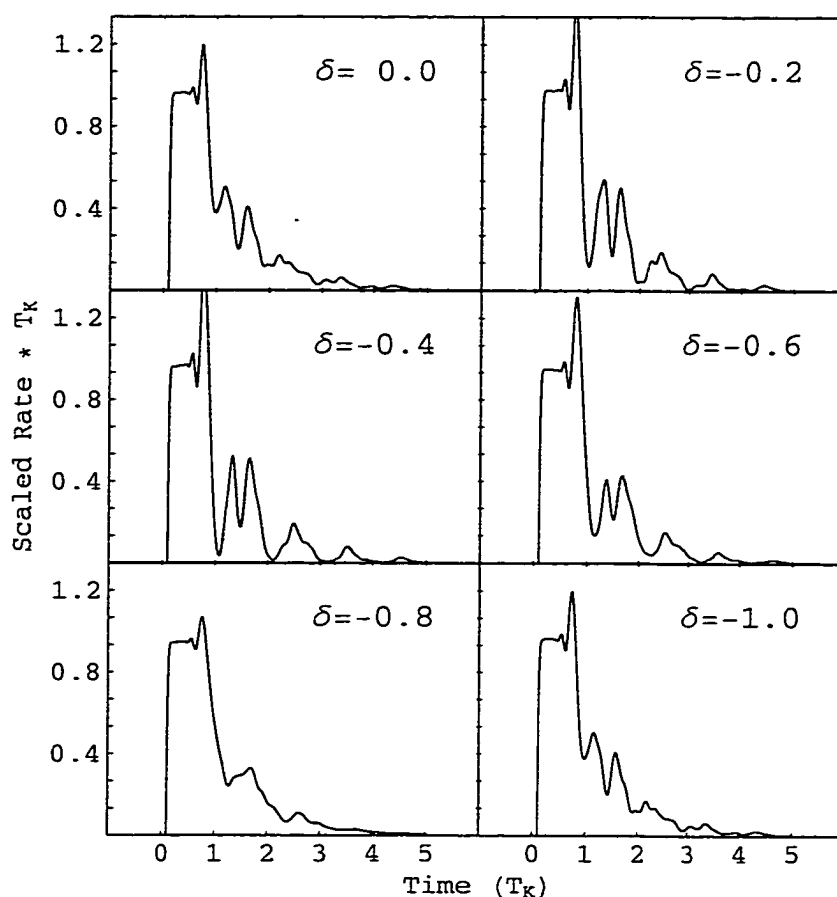


Figure 4.2

Shock-wavepacket decay rate as a function of time for several values of the final state quantum defect δ . The initial state is taken to have a quantum defect of 1.19 for all of the plots. Shifting the value of δ is equivalent to "shifting" the Spectral Density A_ν relative to the Rydberg overlap function $O(\nu, n^*)$; changing the number and position of spectral peaks that are seen through the overlap function, and thus the shape of the decay curve. Due to the periodic form of A_ν , values of δ are only unique Mod 1 – hence the graphs for $\delta = 0.0$ and $\delta = -1.0$ are identical. A different initial state quantum defect would result in different decay rates, but the periodicity would remain.

Chapter 5 Results and Analysis

We have produced shock-wavepackets from several different initial Rydberg states of Calcium. Their cyclic, non-exponential decays have been observed, and are presented here. Both the decays and the rates are found to be in excellent agreement with the predictions of MQDT.

Starting from Rydberg states in Calcium with principle Quantum number $25 \leq n \leq 32$, we have created and monitored the decay of ICE induced shock-wavepackets. Over the next eight pages we present our experimental results (Figures 5.1 - 5.9).

The small boxes in the upper plots are our normalized fast electron counts. Each point is the average of four separate data "runs". As mentioned previously, each point recorded in a run was averaged over 30 laser shots.

The vertical dashed lines appearing on each graph are spaced at integer multiples of the classical Kepler period ($\tau_k = 2\pi n^3$) corresponding to the initial Rydberg state of each SWP. While the slope of the data remains somewhat constant between Kepler periods, it changes dramatically from one to the next. This is clearly a non-exponential behavior.

The thin solid line running through the boxes is the theoretical survival probability $\mathcal{P}[t]$, calculated with $\delta = -0.19$ and $\gamma = 0.21$. The quantum defects for Ca used in these fits are found in [27], and are presented in tabular form below in Table 5.1. All of our data sets are well described by these parameters.

n	δ_n
25	1.1213494
26	1.1367962
27	1.1504678
28	1.1625950
29	1.1733802
30	1.1830017
31	1.1916109
32	1.1993386

Table 5.1

Quantum defects for Ca from Gentile, Hughey, and Kleppner, Reference [27]. The uncertainties are on the order of a few parts in 10^{-6} .

The thick solid line running through the boxes is simply a "smoothed" interpolation of the data. This smoothing was accomplished through an FFT convolution with a gaussian ($\tau_{\text{FWHM}} = 250$ fs). Since our resolution is already limited by the bandwidths of the two ICE pulses, a gaussian with this width does not significantly "blur" our signal, yet it is sufficient to eliminate the majority of the "noise" in our measurements.

Taking the derivative of our "smoothed" data, allows us to examine the Autoionizing decay *rate* for each SWP. The lower plot on each page is this rate. Note that we account for the decrease in resolution due to our smoothing procedure by reducing the number of "data" points displayed.

The thin line through the rate points is the derivative of the thin line through the data points, and is calculated with the same values for δ and γ .

The non-exponential, stair step decay, of the SWP is most strikingly seen in these plots of the rate. Each "step" has a width of about one Kepler period, with the rate vanishing between steps.

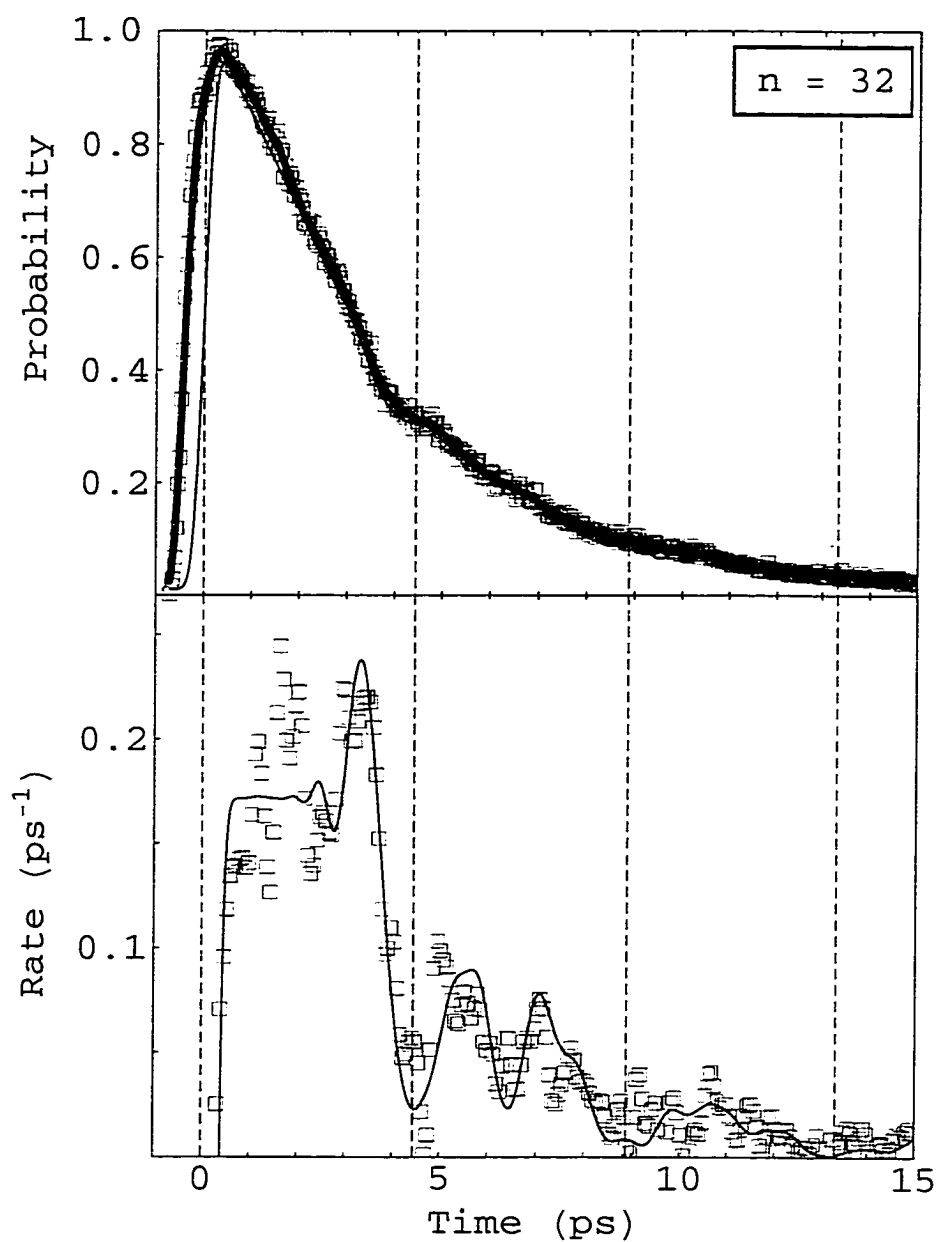


Figure 5.1

Measured decay of a Shock-wavepacket. **Upper plot: Bound State Survival Probability.** The boxes in the upper plot are the normalized electron yields. The thin line is a fit of the data to theory for a final state series quantum defect of $\delta = -0.19$, and scaled decay rate $\gamma = 0.21$. The fat line is an interpolation of our data smoothed through convolution with a gaussian (FWHM=0.250 ps). **Lower plot: Shock-wavepacket Decay Rate.** The boxes are produced by differentiating the smoothed curve above. The thin line is the calculated rate with the same parameters as in the upper plot.

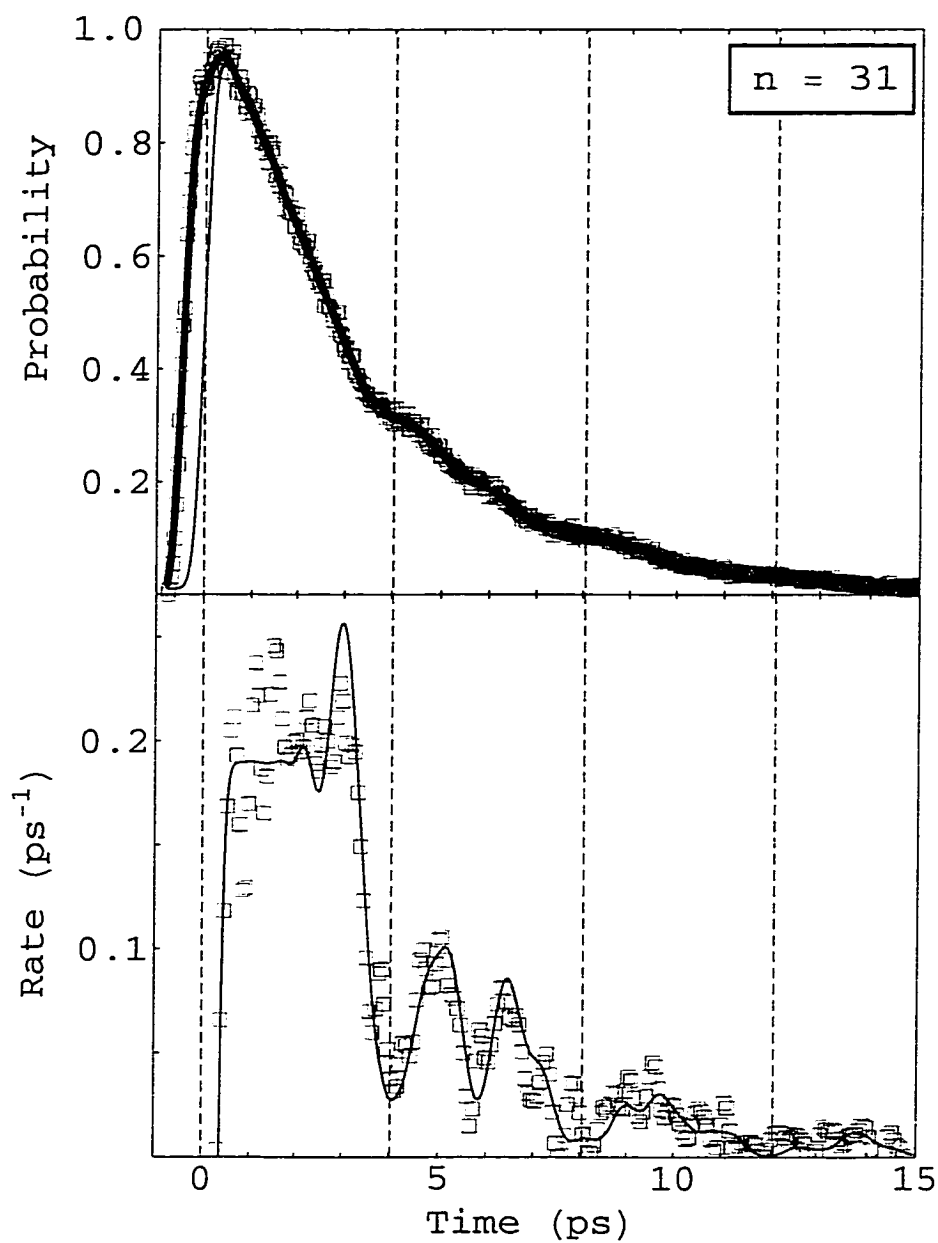


Figure 5.2

Measured decay of a Shock-wavepacket. **Upper plot: Bound State Survival Probability.** The boxes in the upper plot are the normalized electron yields. The thin line is a fit of the data to theory for a final state series quantum defect of $\delta = -0.19$, and scaled decay rate $\gamma = 0.21$. The fat line is an interpolation of our data smoothed through convolution with a gaussian (FWHM=0.250 ps). **Lower plot: Shock-wavepacket Decay Rate.** The boxes are produced by differentiating the smoothed curve above. The thin line is the calculated rate with the same parameters as in the upper plot.

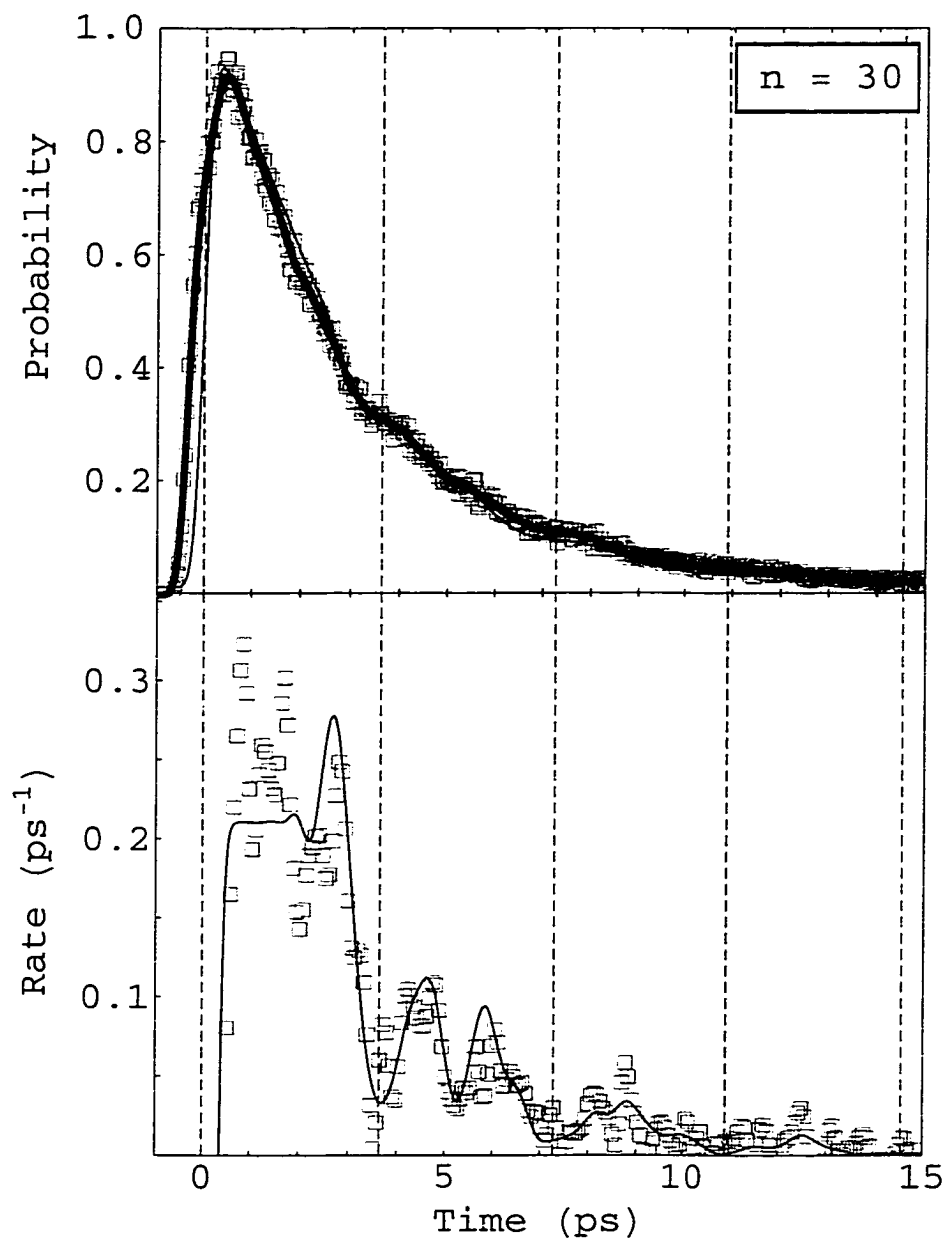


Figure 5.3

Measured decay of a Shock-wavepacket. **Upper plot: Bound State Survival Probability.** The boxes in the upper plot are the normalized electron yields. The thin line is a fit of the data to theory for a final state series quantum defect of $\delta = -0.19$, and scaled decay rate $\gamma = 0.21$. The fat line is an interpolation of our data smoothed through convolution with a gaussian (FWHM=0.250 ps). **Lower plot: Shock-wavepacket Decay Rate.** The boxes are produced by differentiating the smoothed curve above. The thin line is the calculated rate with the same parameters as in the upper plot.

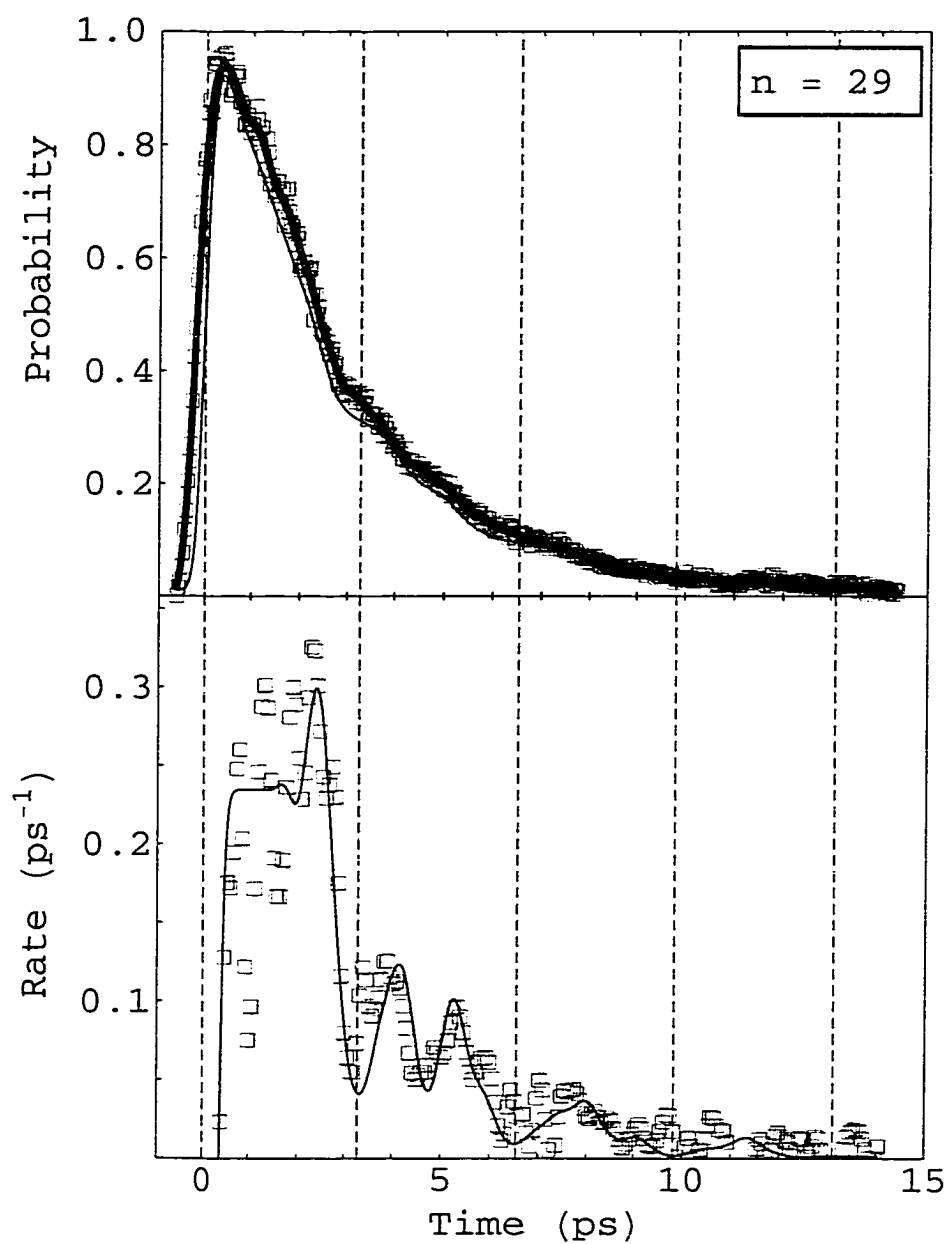


Figure 5.4

Measured decay of a Shock-wavepacket. **Upper plot: Bound State Survival Probability.** The boxes in the upper plot are the normalized electron yields. The thin line is a fit of the data to theory for a final state series quantum defect of $\delta = -0.19$, and scaled decay rate $\gamma = 0.21$. The fat line is an interpolation of our data smoothed through convolution with a gaussian (FWHM=0.250 ps). **Lower plot: Shock-wavepacket Decay Rate.** The boxes are produced by differentiating the smoothed curve above. The thin line is the calculated rate with the same parameters as in the upper plot.

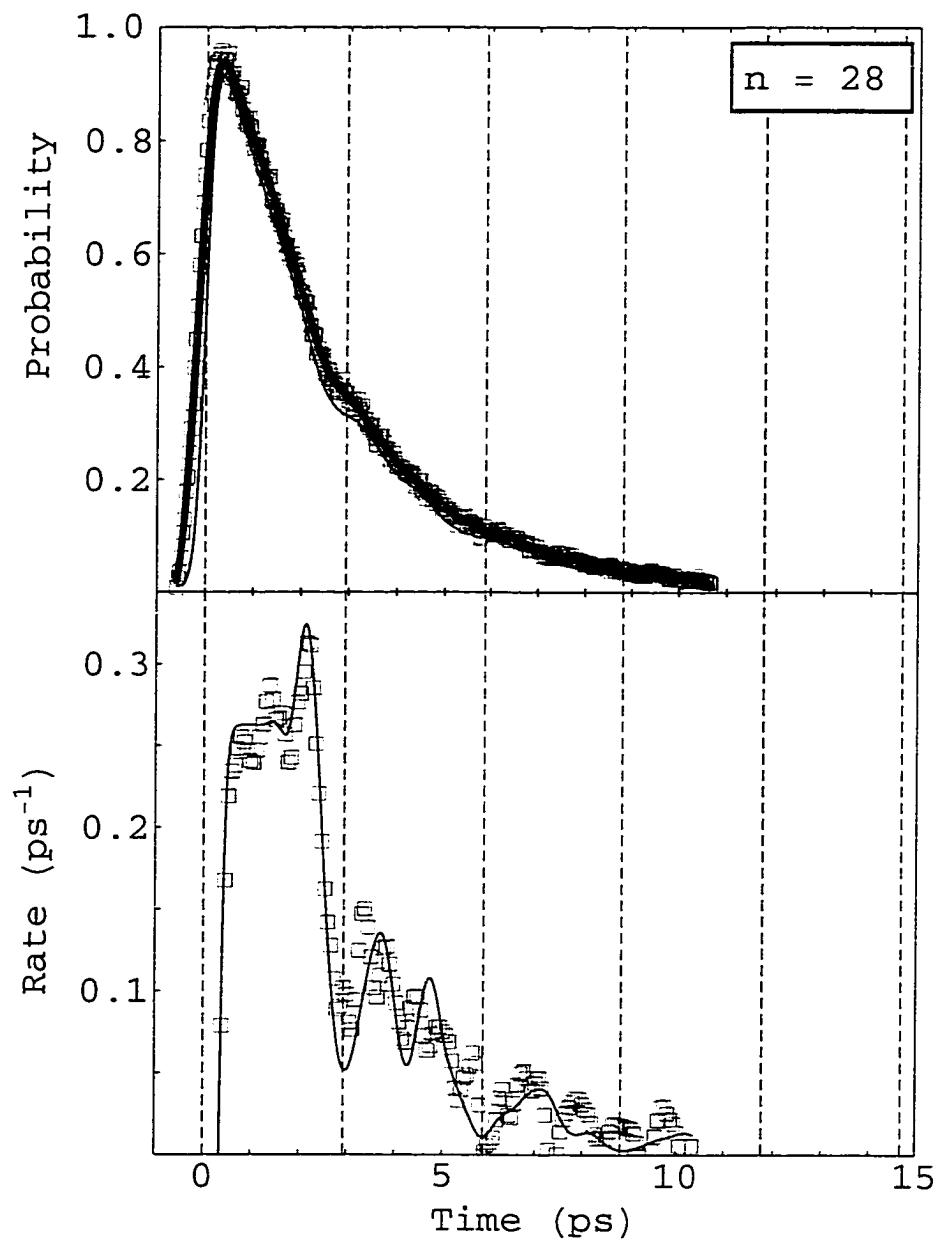


Figure 5.5

Measured decay of a Shock-wavepacket. **Upper plot: Bound State Survival Probability.** The boxes in the upper plot are the normalized electron yields. The thin line is a fit of the data to theory for a final state series quantum defect of $\delta = -0.19$, and scaled decay rate $\gamma = 0.21$. The fat line is an interpolation of our data smoothed through convolution with a gaussian (FWHM=0.250 ps). **Lower plot: Shock-wavepacket Decay Rate.** The boxes are produced by differentiating the smoothed curve above. The thin line is the calculated rate with the same parameters as in the upper plot.

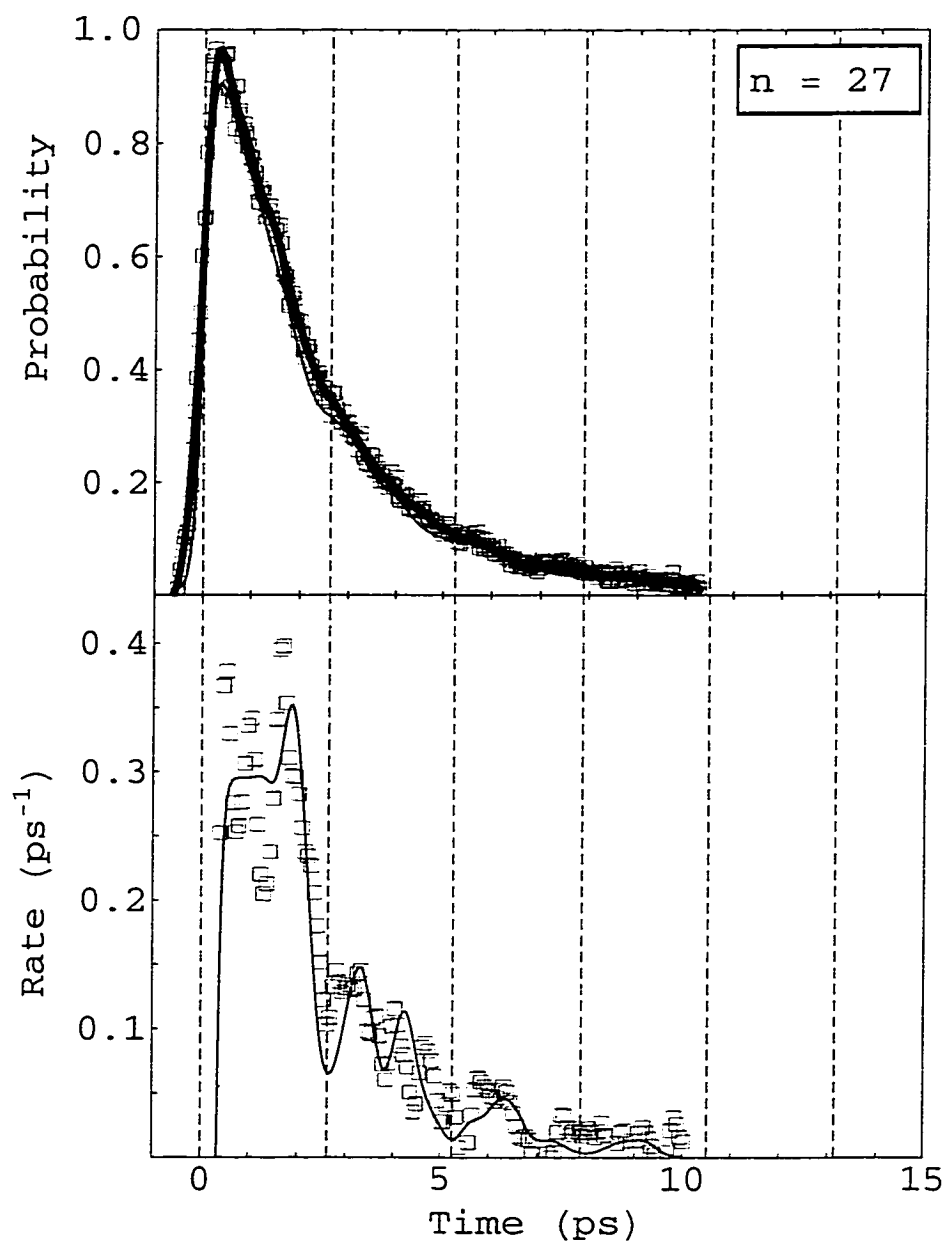


Figure 5.6

Measured decay of a Shock-wavepacket. **Upper plot: Bound State Survival Probability.** The boxes in the upper plot are the normalized electron yields. The thin line is a fit of the data to theory for a final state series quantum defect of $\delta = -0.19$, and scaled decay rate $\gamma = 0.21$. The fat line is an interpolation of our data smoothed through convolution with a gaussian (FWHM=0.250 ps). **Lower plot: Shock-wavepacket Decay Rate.** The boxes are produced by differentiating the smoothed curve above. The thin line is the calculated rate with the same parameters as in the upper plot.

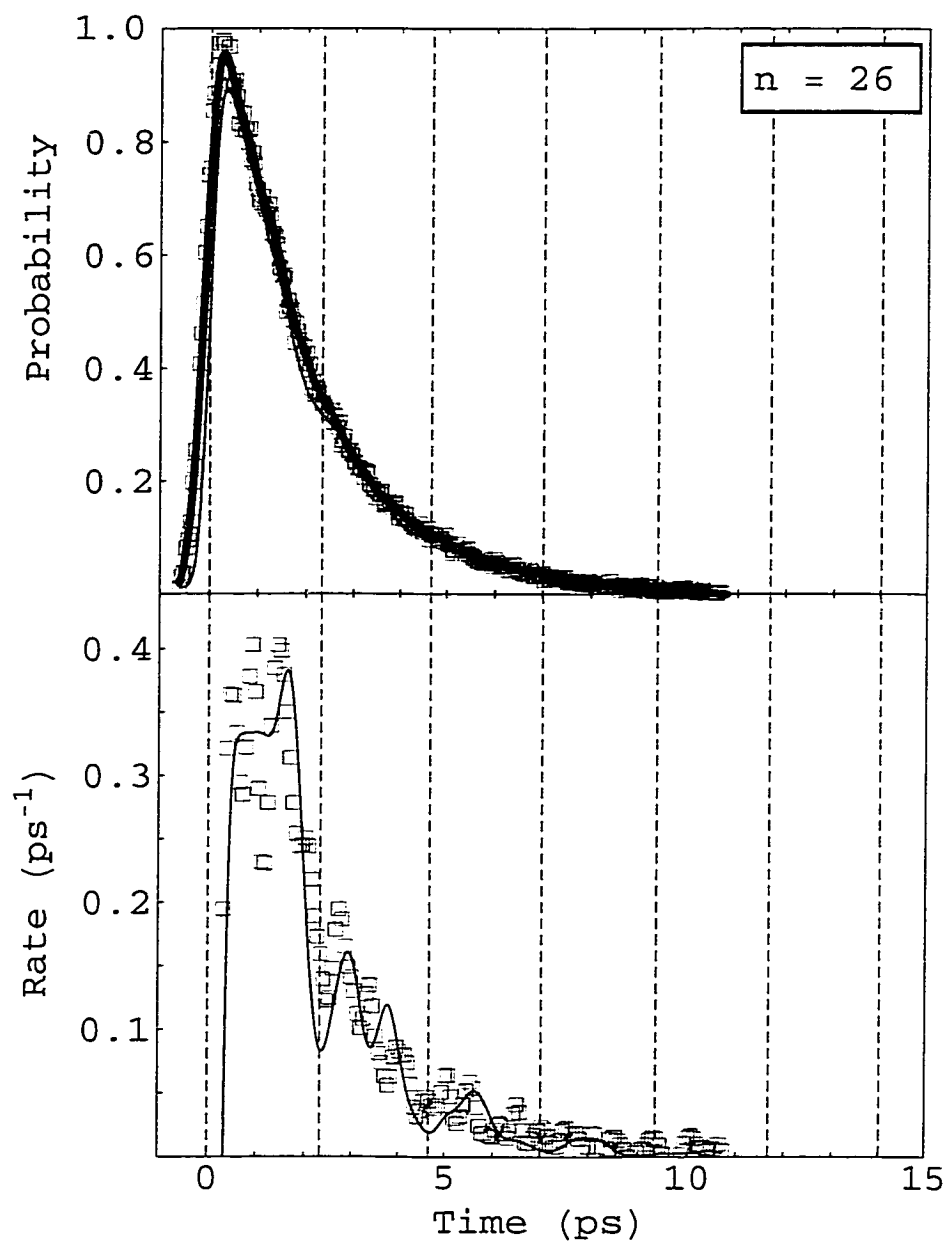


Figure 5.7

Measured decay of a Shock-wavepacket. **Upper plot: Bound State Survival Probability.** The boxes in the upper plot are the normalized electron yields. The thin line is a fit of the data to theory for a final state series quantum defect of $\delta = -0.19$, and scaled decay rate $\gamma = 0.21$. The fat line is an interpolation of our data smoothed through convolution with a gaussian (FWHM=0.250 ps). **Lower plot: Shock-wavepacket Decay Rate.** The boxes are produced by differentiating the smoothed curve above. The thin line is the calculated rate with the same parameters as in the upper plot.

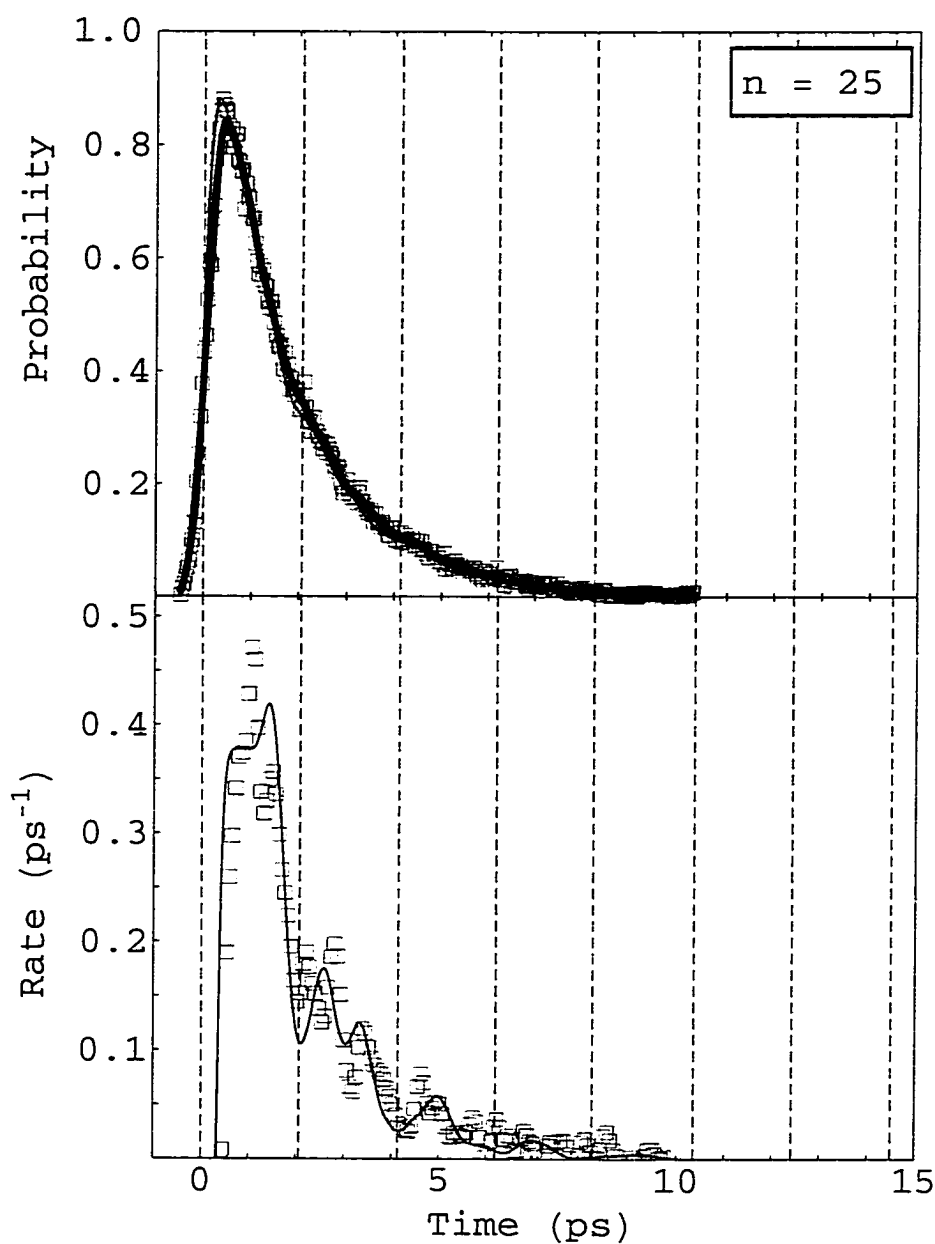


Figure 5.8

Measured decay of a Shock-wavepacket. **Upper plot: Bound State Survival Probability.** The boxes in the upper plot are the normalized electron yields. The thin line is a fit of the data to theory for a final state series quantum defect of $\delta = -0.19$, and scaled decay rate $\gamma = 0.21$. The fat line is an interpolation of our data smoothed through convolution with a gaussian (FWHM=0.250 ps). **Lower plot: Shock-wavepacket Decay Rate.** The boxes are produced by differentiating the smoothed curve above. The thin line is the calculated rate with the same parameters as in the upper plot.

The best-fit parameters ($\gamma = 0.211 \pm 0.004$, $\delta = -0.20 \pm 0.08$) were determined numerically using a routine written in *Mathematica* to minimize the sum of the squares of the residuals. The results did not change significantly from set to set, nor when multiple sets were fit simultaneously. Fits to the rates also yielded similar best-fit values. The errors quoted were determined using Monte Carlo techniques [45], assuming that the errors in our rate signal were normally distributed about the "true" signal with a standard deviation equal to 25% of the rate amplitude.

It should be apparent from our discussion in Chapter 2, that this value of γ is about half the size of 0.41 value determined from frequency domain measurements.[26] If we refer to the bottom two frames of Figure (4.1) from the last chapter, we see that for $\gamma = 0.41$, the shock-wavepacket decays almost entirely in the first Kepler period; vanishing entirely by the end of the second. This is quite obviously not the behavior we observed in our experiment. Looking back at our excitation scheme, Figure (3.1), we see that we could arrive in a final state with total angular momentum $J = 1, 3$. In the original frequency domain ICE measurements [25], Jones stated that the multiple resonances from the different excitation channels could not be resolved. Our time domain measurements then should be viewed as complementary to those made

in the frequency domain. In both domains, we are attempting to model the autoionization process in terms of two channels only; parametrizing the physics in terms of an effective series quantum defect δ , and an effective scaled rate γ . In the frequency domain, the effective series defect is very well determined, while the inferred scaled rate implies a temporal behavior quite different from what is actually observed. In the time domain measurements, the scaled rate is well determined, while the series defects (and hence, the locations of the resonances) are much harder to extract. This should be clear from the relative sizes of their respective errors (for γ , $\frac{0.004}{0.211} \Rightarrow 2\%$, while for δ , $\frac{0.08}{0.20} \Rightarrow 40\%$). These differences are indicative of the relative sensitivities of the decay rate to small changes in the parameters. Referring to Figure (4.1) and Figure (4.2) from the previous chapter, we see that small changes in γ result in very noticeable alterations of the stair-step heights; whereas small changes in δ (on the order of ± 0.1 or less) have almost no effect.

A careful examination of our curves reveals that all of the rise times are correct as well, although the rising edges for the highest n values are slightly displaced. In other words, the thin theory line maintains a slope that parallels that of the rising edge of the data.

We have assumed that our two ICE pulses, SP1 and SP2, are transform limited gaussians; for a short pulse system such as we are using, this

assumption has limited validity. For the decay portion of the curve, the exact shape of the pulse doesn't matter -- its main effect is to broaden the signal temporally, and any well behaved, reasonably narrow pulse shape will do. The rising edge, however, is extremely sensitive to the pulse shape; indeed, the derivative of the rising edge is directly proportional to it. A better knowledge of the temporal profile for our short pulses, then, might allow us to achieve better agreement in this region.

5.1 Scaling of SWP Data

There is a high degree of similarity among all of the decay curves. These similarities are made more apparent if we scale the time axis in units of the Kepler period of the initial Rydberg electron, $T_k = 2\pi n^3$. The upper plot, Figure 5.9 below, shows the decay curves for $n = 32, 30, 28,$ and 26 superimposed on the same time axis. The lower plot, Figure 5.10, shows the same data sets in scaled units.

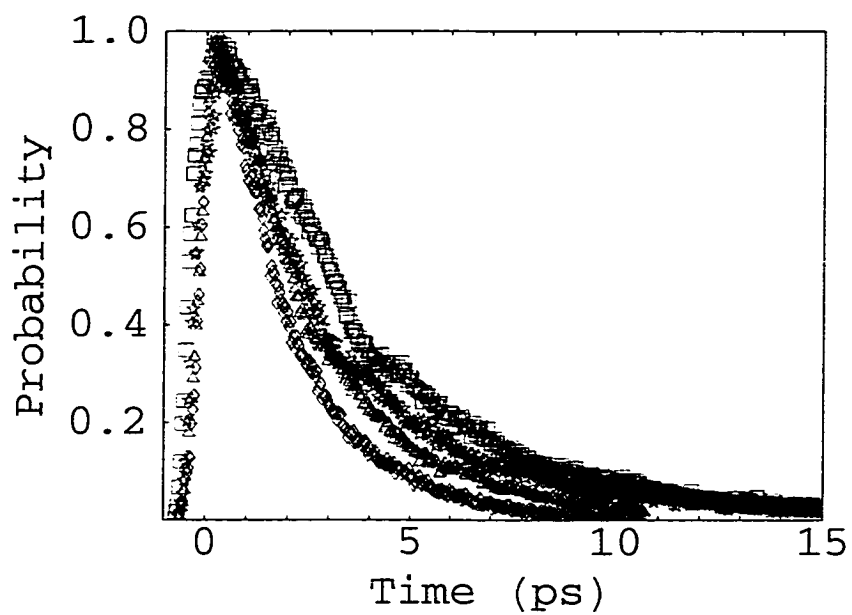


Figure 5.9

Scaling of SWP survival Probability. The survival probability data for four SWP's starting from initial Rydberg states of $n = 32, 30, 28, 26$.

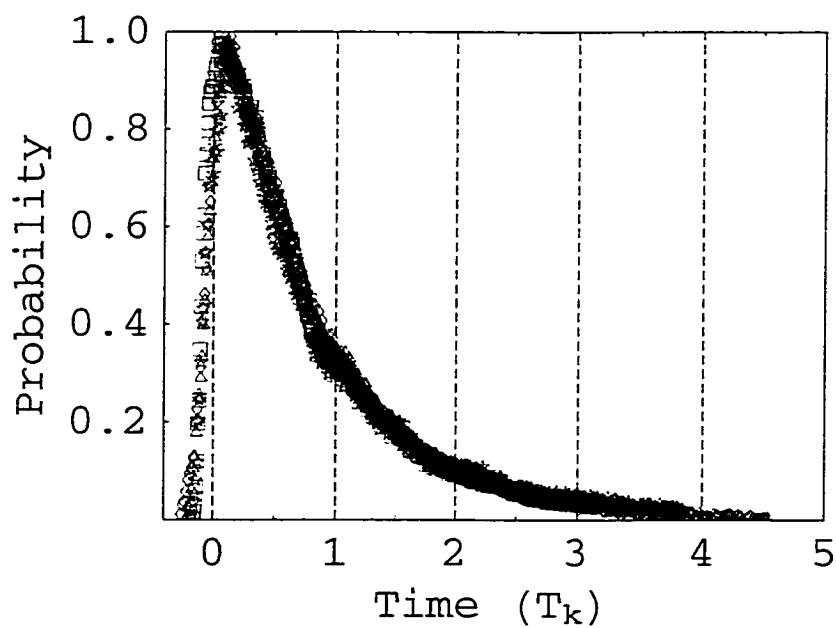


Figure 5.10

Scaling of SWP survival Probability. The same data sets ($n = 32, 30, 28, 26$) as Figure (5.9), but their time axes are rescaled by their initial state Kepler periods.

The same dramatic scaling is present in the rate. The left-hand plot in Figure 5.11 (below) shows the unscaled rates for $n = 32, 30, 28,$ and 26 . The right-hand plot shows the scaled rates for the same data sets. The (dimensionless) magnitude of the scaled rate is simply the derivative of the scaled decay curve with respect to scaled time, and is equal to the unscaled rate multiplied by the Kepler period.

$$t \rightarrow \tau (2 \pi n^3) \Rightarrow \partial_\tau S[\tau] = (2 \pi n^3) \partial_t S[t] \quad (5.1)$$

.

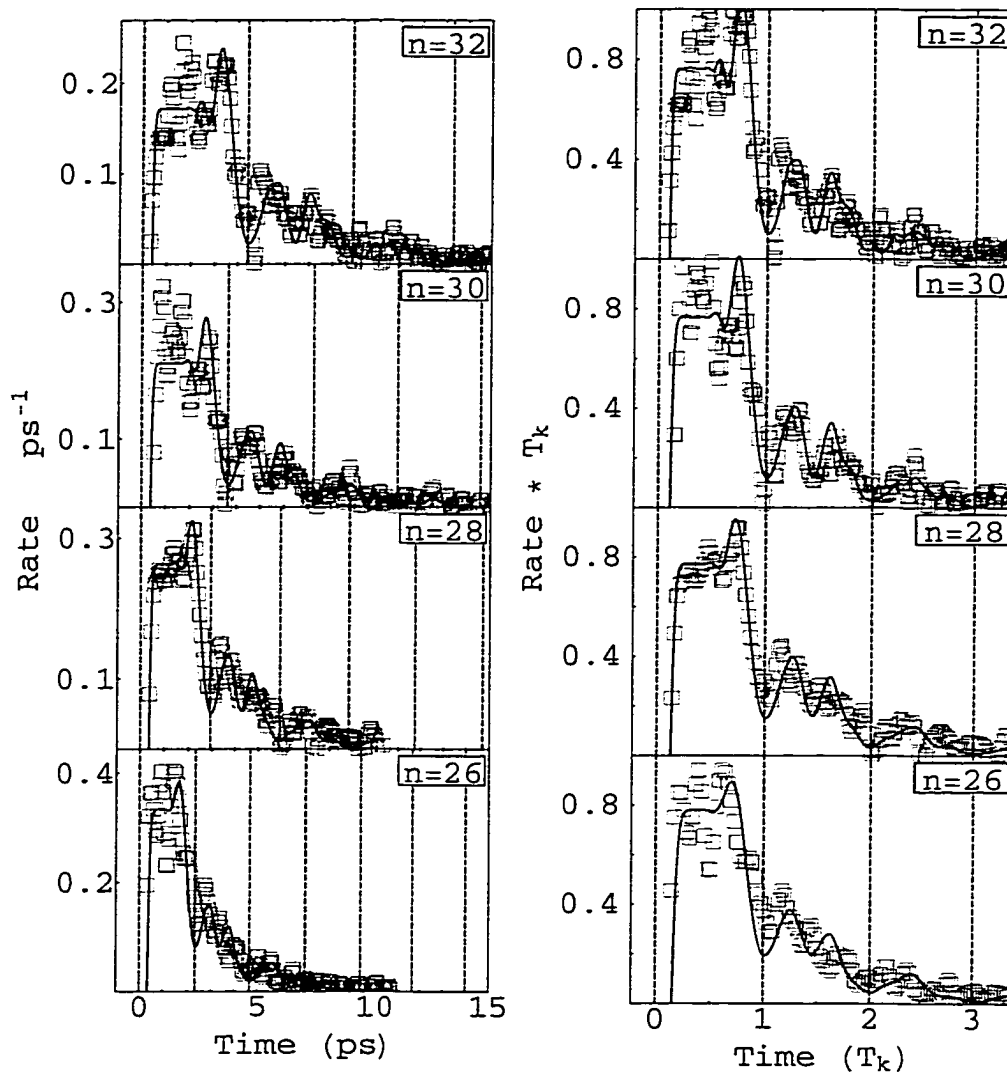


Figure 5.11

Scaling of SWP Decay Rate. The left-hand plot shows the decay rate for four SWP's starting from initial Rydberg states of $n = 32, 30, 28, 26$. The right-hand plot shows the same data sets rescaled by their initial state Kepler periods.

While highly similar, the scaled rates are not identical. These deviations from "perfect" scaling are easily explained in terms of three different effects.

First, it must be remembered that all of our curves (theory and data) have been convoluted with two gaussians to account for the finite pulse-length of our ultra-fast lasers. These pulse-lengths depend only on the laser, and therefore *do not scale* with the Kepler period of a given initial state. Even if our pre-convoluted scaled curves were identical, the physical curves would be different, since the scaled width of the gaussians is smaller for large n^* than for small n^* . For example, each scaled decay rate shown in Figure 5.11 has a minimum located at the first Kepler period. The minima become deeper (approach zero) as n^* increases. This is exactly what one would expect -- convolute a sharp minimum with a "narrow" gaussian, and it stays fairly sharp; convolute it with a "fat" gaussian, and it tends to get "filled in".

The second contributor to scaling deviations is the quantum defect of the initial state. In both Chapter 2 and Chapter 4, we have seen that the important quantity in determining the behavior of ICE experiments, isn't the series quantum defect per se, but rather, the difference between the series quantum defect and the quantum defect for the initial state. For the rates shown in Figure (5.11), the initial state quantum defect

varies from 1.14 to 1.20 , or by 5%. Even a change of this size will produce significant differences in the rate.

The third factor that produces deviations from scaling is the "nature of the beast" for the Rydberg states we are working in. Wang and Cooke's[1] pictorial "stair-step" calculation was made in the "large - n" limit. Essentially, this means that in the Equation for the transition rate (4.4), one expands the energy to 1st order in ν near n^*

$$\mathcal{W}_\nu = -\frac{1}{2\nu^2} \simeq -\frac{1}{2n^{*2}} + \frac{1}{n^{*3}}(\nu - n^*) = -\frac{3}{2n^{*2}} + \frac{\nu}{n^{*3}} \quad (5.2)$$

The first term is a ν -independent phase that can clearly be dropped. The transition rate (ignoring any convolutions for the moment) is now given by

$$T[t] = \left| n^{*-3} \int d\nu e^{i\frac{\nu}{n^*} t} \mathcal{T}[\mathcal{W}_\nu] \right|^2 \quad (5.3)$$

Scaling the time by the Kepler period results in

$$T[\tau] = \left| n^{*-3} \int d\nu e^{i2\pi\nu\tau} \mathcal{T}[\mathcal{W}_\nu] \right|^2 . \quad (5.4)$$

The integrand,

$$\mathcal{T}[\mathcal{W}_\nu] = \frac{\sqrt{\text{Sinh}[\pi\gamma]/2\pi}}{\text{Sin}[\pi(\nu + \delta + i\frac{\gamma}{2})]} \left(\frac{\text{Sin}[\pi(\nu - n^*)]}{\pi(\mathcal{W}_\nu - \mathcal{W}_{n^*})} \right) \quad (5.5)$$

is strongly peaked near $\nu = n^*$, where it can be approximated by

$$\mathcal{T}[\mathcal{W}_\nu] \simeq \frac{\sqrt{\text{Sinh}[\pi\gamma]/2\pi}}{\text{Sin}[\pi(\nu + \delta + i\frac{\gamma}{2})]} n^{*3} . \quad (5.6)$$

While this last approximation is too crude to accurately calculate the scaled rate with, we have included it to show that the overall factor of n^{*-3} tends to be eliminated. The end result is a scaled decay rate with very little dependence on the value of n^* .

In Figure (5.12) below we plot the survival probability and the decay rate for $n = 31$ using the large- n approximation of Equation (5.4) and Equation (5.6). For comparison, we include our signal and rate "data" as before.

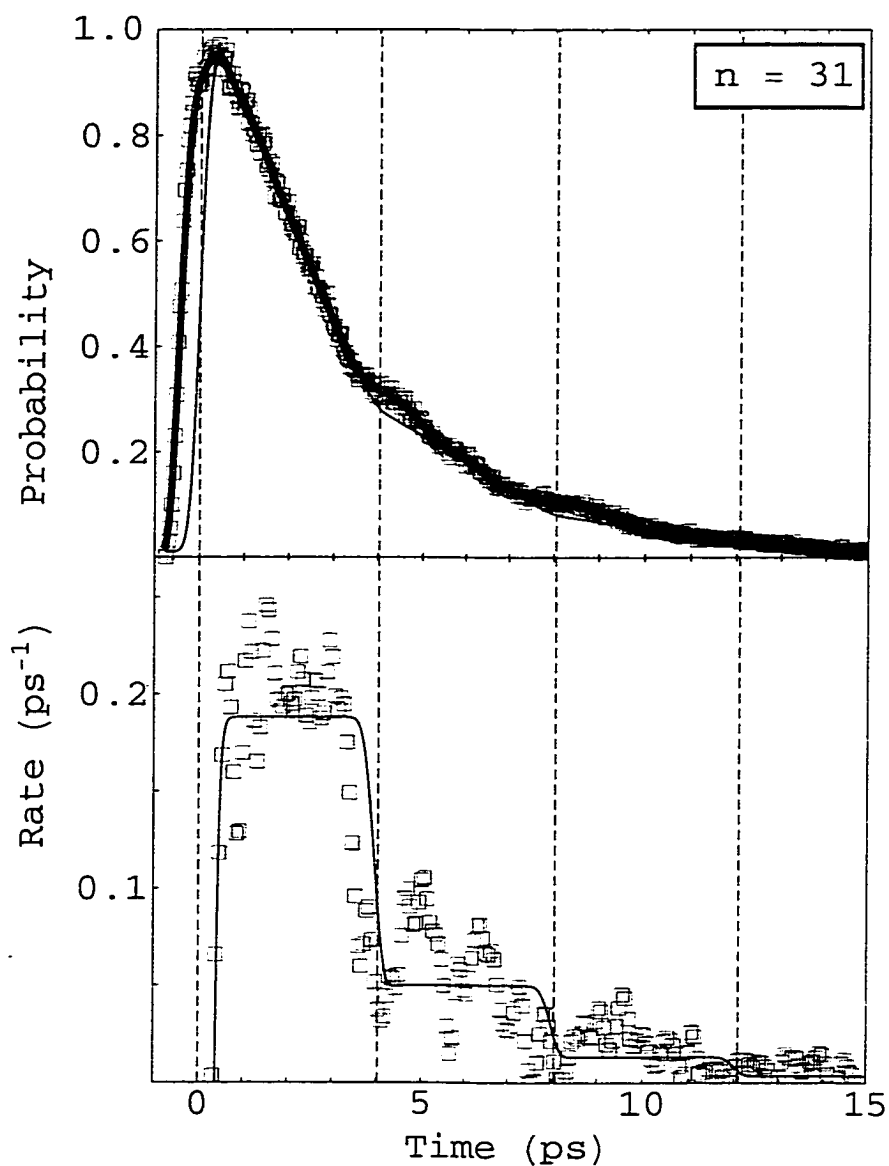


Figure 5.12

Measured decay of a Shock-wavepacket. **Upper plot: Bound State Survival Probability.** The boxes in the upper plot are the normalized electron yields. The thin line is a fit of the data to theory for a final state series quantum defect of $\delta = -0.19$, and scaled decay rate $\gamma = 0.21$ calculated in the Large- n limit. The fat line is an interpolation of our data smoothed through convolution with a gaussian (FWHM=0.250 ps). **Lower plot: Shock-wavepacket Decay Rate.** The boxes are produced by differentiating the smoothed curve above. The thin line is the calculated rate (in the Large- n limit) with the same parameters as in the upper plot. This Large- n approximation only matches the data "on average", but demonstrates the "stair-step" decay rate described by Wang and Cooke[1].

While this large- n approximation fits our data "on average" (and is easily seen to produce the stair-step decay curve of Wang and Cooke[1]), it completely misses the prominent wiggles in the rate. In order to capture these wiggles, we must retain higher order terms in our expansion of the exponential. Retaining terms to 2nd order in ν produces a significantly better fit to our data and the rate (Figure 5.13). Unfortunately, the factors of n^* no longer cancel in the exponent.

Consequently, Near-perfect scaling can only occur when a linear large- n approximation to the energy is valid. Whenever higher order terms are required to accurately model the decay rate, their presence will introduce non-scaling time dependent terms.

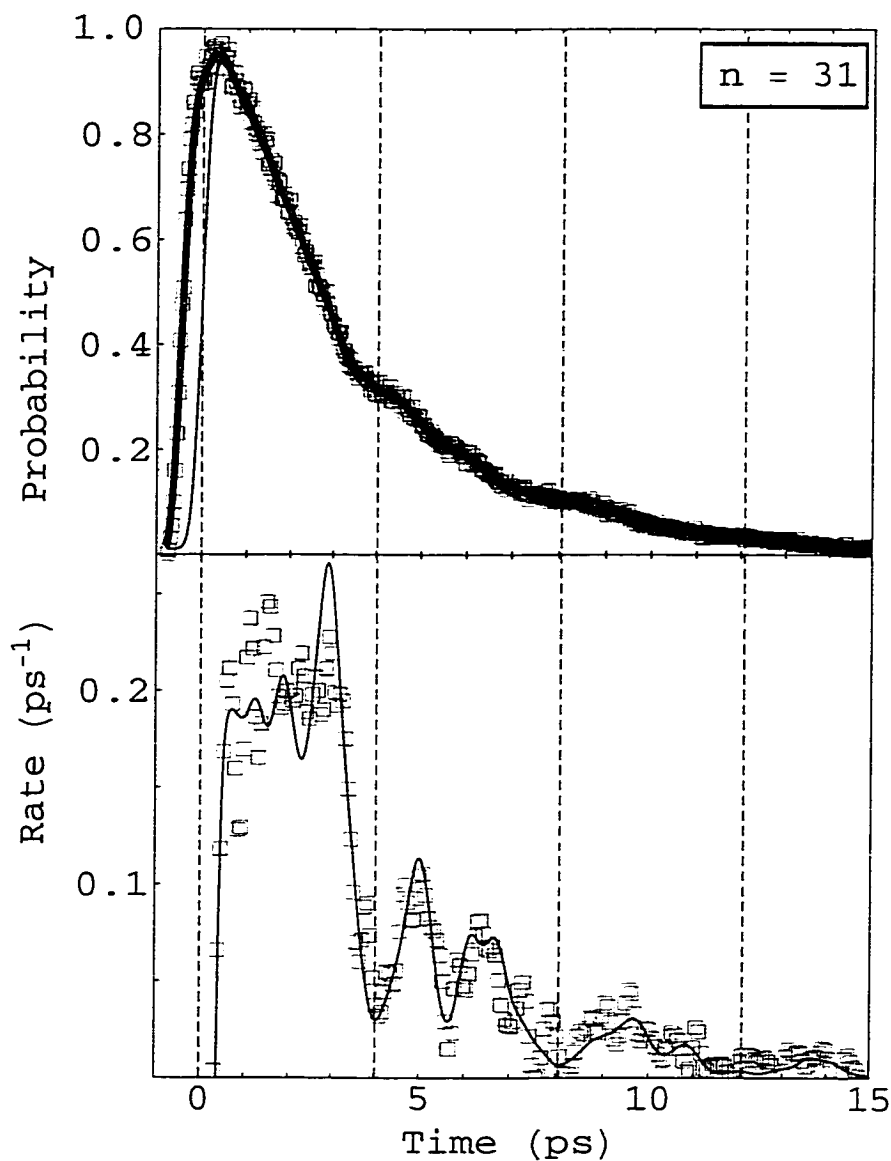


Figure 5.13

Measured decay of a Shock-wavepacket. **Upper plot: Bound State Survival Probability.** The boxes in the upper plot are the normalized electron yields. The thin line is a fit of the data to theory for a final state series quantum defect of $\delta = -0.19$, and scaled decay rate $\gamma = 0.21$ calculated in the Large- n limit taken to 2nd order in ν . The fat line is an interpolation of our data smoothed through convolution with a gaussian (FWHM=0.250ps). **Lower plot: Shock-wavepacket Decay Rate.** The boxes are produced by differentiating the smoothed curve above. The thin line is the calculated rate (in the 2nd order Large- n limit) with the same parameters as in the upper plot. This Large- n approximation matches the data significantly better than the linear approximation (Figure 5.12).

Shock-Wavepackets: Chapter 6 Another Point of View

In this chapter, we simulate the temporal evolution of a shock-wavepacket. When we introduced the shock-wavepacket concept in Chapter 4, we spoke of the orbital behavior of the shock-wavefront contained within. The simulation allows us to visualize and quantify this previously qualitative description. Finally, we show how the "wavepacket approach" leads to a different way of understanding the non-exponential, stair-step behavior of the decay rate.

6.1 The Wavepacket Approach

As an alternative to the Transition Moment formalism presented in Chapter 4, one may calculate the bound-state survival probability directly by explicitly constructing the shock-wavepacket, and evaluating the norm as a function of time. [28] With slight modifications to the notation from Chapter 2, the complete wavefunction of the autoionizing state is written as

$$\Psi_v[\mathbf{s}, \mathbf{r}] = A_v \phi_v[r] \chi^+[\mathbf{s}] + e^{i\alpha} \chi^o[\mathbf{s}] \phi_\epsilon[r], \quad (6.1)$$

where as before

$$A_\nu = \frac{\sqrt{\text{Sinh}[\pi \frac{\gamma}{2}]}{\text{Sin}[\pi(\nu + \delta + i \frac{\gamma}{2})]}, \quad (6.2)$$

and $\phi_\nu[r]$ is the radial wavefunction describing a Rydberg electron with energy $\mathcal{W}_\nu = -\frac{1}{2\nu^2}$.

$\chi[s]$ represents the product of the angular wavefunction for the Rydberg electron with the wave function for the remaining ionic core, with the vector \mathbf{s} representing all of the relevant coordinates and quantum numbers. χ^+ represents the ionic core with the second valence electron in an excited state, while χ^0 is the ionic core with the second valence electron in its ground state.

The Ψ_ν form a complete set, so we can write the shock-wavepacket as a linear superposition of these states.

$$\Psi[\mathbf{s}, r, t] = \int d\mathcal{W}_\nu c_\nu \psi_\nu[\mathbf{s}, r] e^{-i\mathcal{W}_\nu t} \quad (6.3)$$

The ICE pulse is sufficiently short (on the scale of the Kepler period of the initial Rydberg state) that we assume the radial wavefunction of the Rydberg electron to remain unchanged during the Isolated Core Excitation. This is the so-called "Sudden Approximation", and it allows us to write

$$\Psi[\mathbf{s}, r, 0] = \phi_{n^*}[r] \Phi^+[\mathbf{s}], \quad (6.4)$$

from which we can exploit the orthonormality of the ψ_ν to extract the values c_ν :

$$c_\nu = A_\nu^* O[\nu, n^*], \quad (6.5)$$

$$O[\nu, n^*] \equiv \int d\mathbf{r} r^2 \phi_\eta^*[\mathbf{r}] \phi_n[\mathbf{r}] = \frac{\text{Sin}[\pi(\nu - n^*)]}{\pi(\mathcal{W}_\nu - \mathcal{W}_{n^*})}. \quad (6.6)$$

The survival probability of the quasi-bound electron is then simply the norm of the SWP. Since the integrations over the \mathbf{s} coordinates are independent of time, we can suppress all reference to the core and angular wave functions, writing the shock-wavepacket as

$$\Psi[\mathbf{r}, t] = \int d\mathcal{W}_\nu |A_\nu|^2 O[\nu, n^*] \phi_\nu[\mathbf{r}] e^{-i\mathcal{W}_\nu t}. \quad (6.7)$$

We have used this formulation to simulate the evolution and decay of the shock-wavepacket initiating from the $n = 31$ state. The energy integral was taken as a sum over 398 evenly spaced values of ν , $20 < \nu < 40$ in steps of ≈ 0.056 . The radial wavefunctions $\phi_\nu[\mathbf{r}]$ were calculated in *Mathematica* using standard Numerov [29] techniques. To give an idea of the sort of "coverage" this affords us, we plot the "normalized" overlap function $O(\nu, n^*)/(\nu n^*)^{3/2}$ for $n = 30$ in Figure (6.1) below, with each dot representing a basis function used in our simulation.

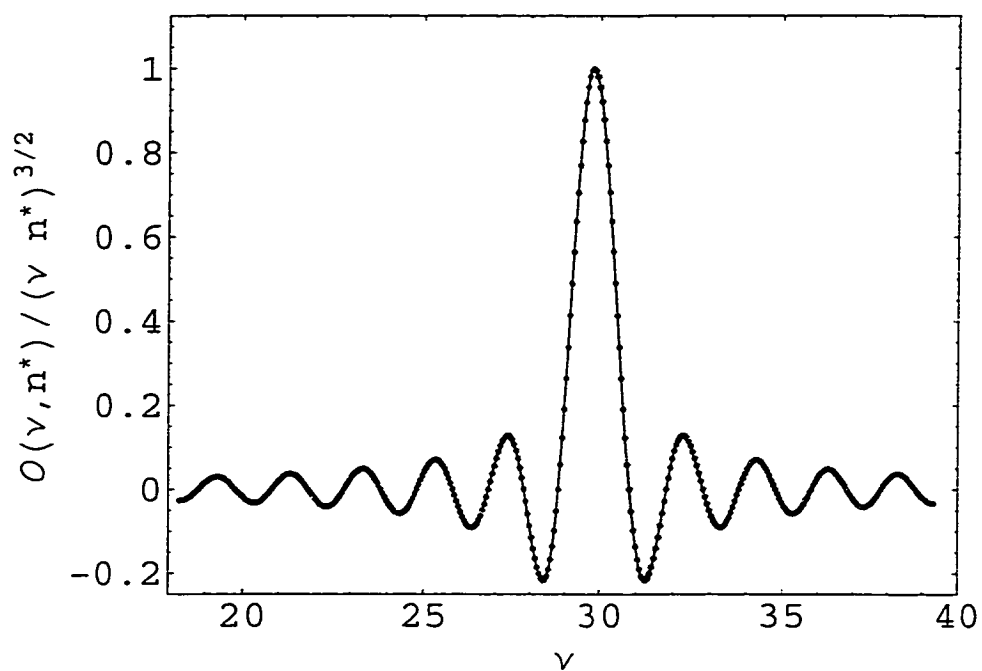


Figure 6.1

Basis functions used in Shock-wavepacket simulation. Each dot represents a basis function, with horizontal position corresponding to the function's effective principle quantum number v . The vertical position of each dot corresponds to the overlap of the basis function with the initial Rydberg State ($n = 31$), and indicates the amount of population transferred to a given final state by the ICE pulse. The thin line is just the normalized overlap function $O(v, n^*) / (v n^*)^{3/2}$ for continuous values of v .

The spacing between basis functions was taken to ensure that non-physical "returns" (discretation induced constructive interference) did not appear in our simulation. Any representation of the SWP by a finite set of basis functions will result in some sort of "returns" eventually occurring. This is easily seen in the large- n linear approximation introduced in Chapter 5. If we also measure time in terms of the Kepler period, the SWP is represented as

$$\Psi[r, \tau] \simeq \sum_k \left| A_{\nu_k} \right|^2 O[\nu_k, n^*] \phi_{\nu_k}[r] e^{-i 2 \pi \nu_k \tau}, \quad (6.8)$$

where

$$\nu_k = \nu_0 + k \Delta, \quad (6.9)$$

$\nu_0 \simeq n^*$, k is an integer, and Δ is the spacing between states. The time dependent terms in the sum are each of the form

$$\text{Exp}[-i 2 \pi \nu_k \tau] = \text{Exp}[-i 2 \pi \nu_0 \tau] \text{Exp}[-i 2 \pi k \Delta \tau] \quad (6.10)$$

Aside from an overall phase, the simulated SWP will return to its initial state whenever $\tau \Delta$ is equal to an integer

$$\left| \Psi\left[r, \tau = \frac{N}{\Delta}\right] \right| = \left| \Psi[r, 0] \right|. \quad (6.11)$$

Determining the condition for non-physical returns also shows us how to avoid them. For a given spacing, we are guaranteed to be return-free until at least $\tau = \frac{N}{2\Delta}$. Our SWPs are almost completely decayed inside of 4.5 Kepler periods. Just to be safe, we choose our spacing so that no returns occur until twice this time has passed; in other words, we set $\Delta = \frac{1}{18} \approx 0.056$.

In the plot below (Figure. 6.2), we display the probability amplitude as a function of position for a duration of 5 Kepler periods. The wavefunction was evolved in steps of $0.05 T_k$, and the wavefunctions were evaluated at 4096 evenly spaced radial positions. The trajectory of the shock-wavefront is easily distinguished (especially near $t = 0$), and is seen to resemble the orbit of a classical Rydberg electron with a Kepler period of $2\pi n^3$.

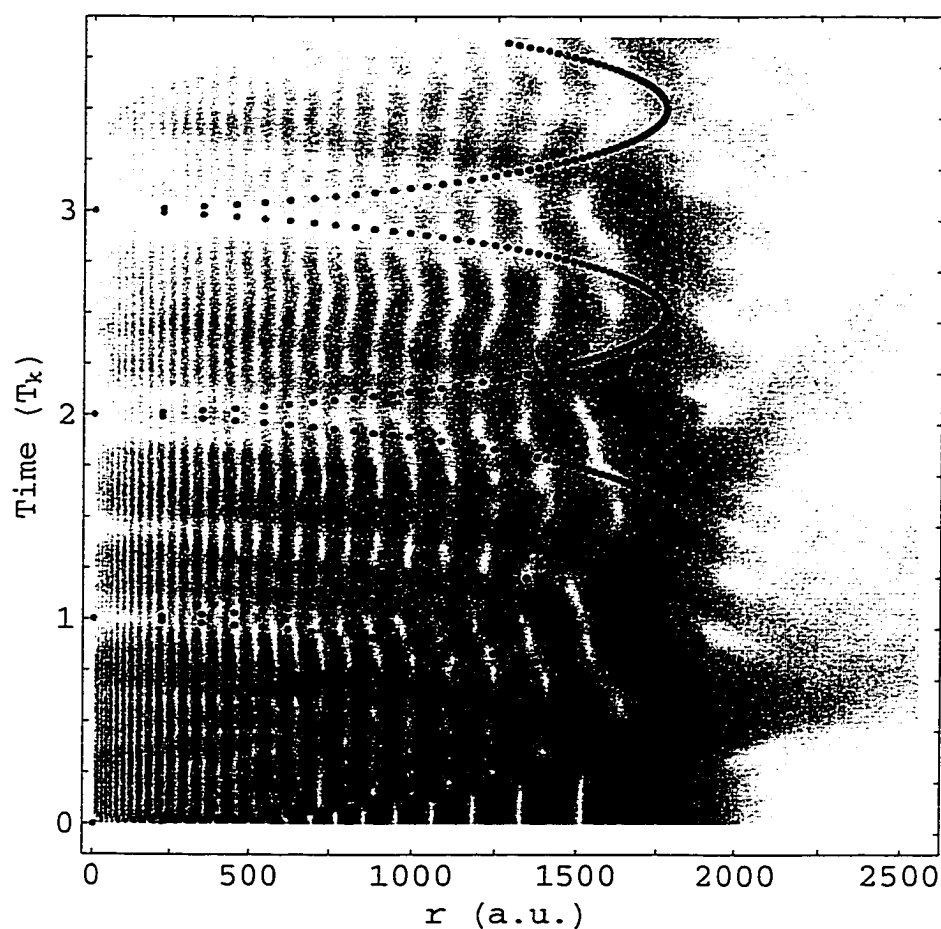


Figure 6.2

Radial distribution of Shock-wavepacket probability amplitude over the lifetime of the SWP. Time is measured in units of the Kepler period, The trajectory of a classical electron with the same energy as the initial Rydberg state is indicated by the dotted line.

We have extracted from our simulation 12 time "slices" of the probability amplitude squared for $0 \leq t \leq 1.1 T_k$, displaying them in "cartoon form" in Figure (6.3) on the next page (drawn as dark, dotted lines). For comparison, in each plot we have included a similar plot (thin, solid lines) for the $n = 31$ state. Note the progress of the "hole" as it leaves the core, only to return after a Kepler period, with the shock-wavepacket left in a greatly depleted semblance of its original state.

A second "discretation effect" effect can be seen in the $t = 0$ slice. Our simulated wavepacket does not adequately reproduce the $n = 31$ state for $r \leq 100$ au. This is unimportant in the overall scheme of things, since, as we have previously mentioned, *it is the large- r behavior that of the wavefunctions, and the small- r information "encoded" therein, that determines how the wavepacket decays.* In order to get a more accurate representation of the wavepacket near the origin, we would need to extend the range of ν -states used in our simulation. This situation is equivalent to the one in FFT calculations where it is necessary to increase the range of frequencies sampled in order to generate more accurate information about a signal's short-time behavior. Furthermore, our experimental resolution near the core is also limited -- by the time the ICE pulse is over, the shock-front is already a few hundred a.u. away from the core.

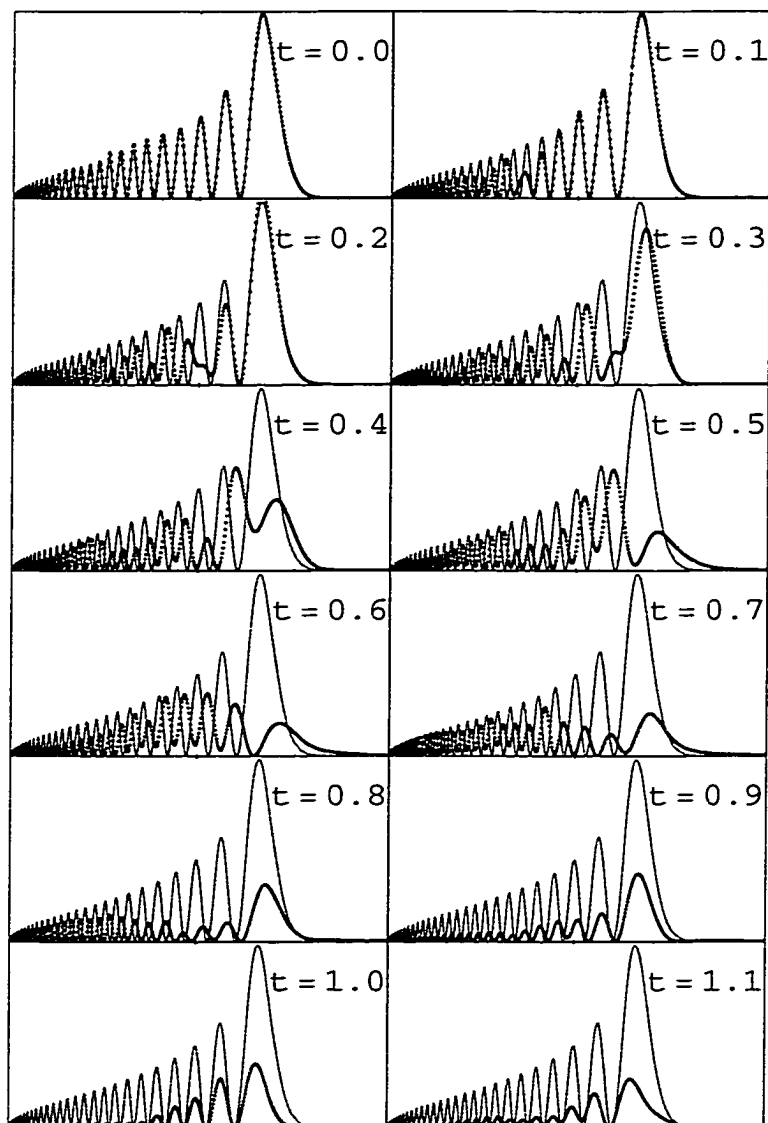


Figure 6.3

Radial distribution of Shock-wavepacket probability amplitude over the first Kepler period (black dots). For comparison, the initial state probability amplitude ($n = 31$) is overlaid on each graph (thin gray line). The Shock-wavefront is seen to travel out and back – reducing the probability amplitude as it goes. After one Kepler period, the wavefunction returns to a shrunken version of its original state.

Finally, we establish consistency between our two calculations by determining the decay rate for our shock-wavepacket simulation. The norm of the wavepacket is calculated numerically, then convoluted with two gaussians ($\tau_{FWHM1} = 212$ ps, $\tau_{FWHM2} = 400$ ps) to simulate our experimental resolution. The resulting rate is shown below (FIG. 8) as dark black dots. The square boxes are our rate "data", and the thin line is our theory curve described in the previous section.

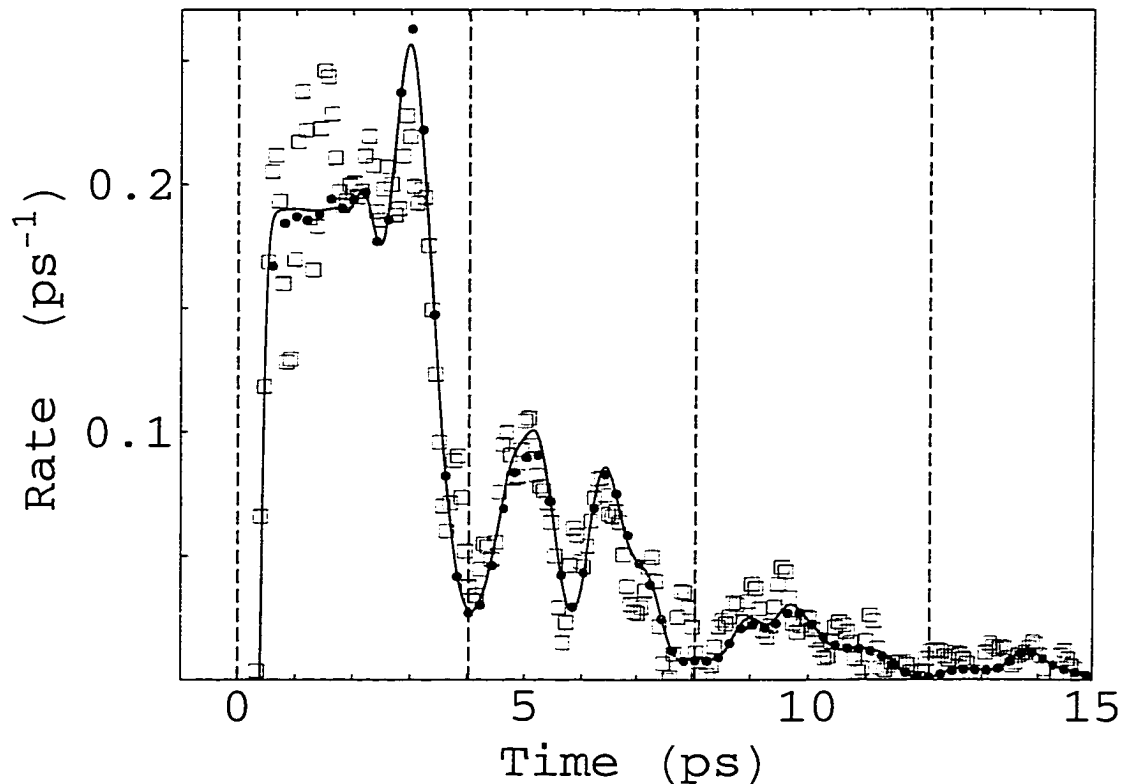


Figure 6.4

Decay Rate of SWP simulation(dots) compared to "data" (boxes) and direct calculation (thin line) presented in Chapters 4 and 5. The decay rate is the time derivative of the numerically integrate norm of the SWP, convoluted with the same gaussians used in our direct calculation.

The excellent agreement between the SWP norm and our previous calculation also serves to verify that our basis set "coverage" is sufficient.

Having satisfied ourselves as to the accuracy of our simulation, we can proceed to use the information contained in Figures (6.2) and (6.3) to enhance our physical understanding of the behavior of Shock-wavepackets. In the semi-classical picture presented in the Introduction, we followed a single "slice" of the outer "asteroid belt" as it entered the scattering region, interacted with the inner "belt" and continued along its orbit. After the first "slice" had completed one orbit, the outer "belt" was returned to its initial condition albeit with its population of asteroids greatly reduced. This is exactly analogous to what we observe in Figure (6.3). The first "slice" whose orbit we followed is replaced by a shock-wavefront that propagates throughout the radial wavepacket. In Figure (6.3) , the "orbits" of the shock-wavefront (starting from the origin at Time = 0, and returning at each classical Kepler period) are easily distinguished. Strikingly, these orbits, or points of maximal destructive interference, are *exactly* the orbits of a classical electron with total energy given by $\mathcal{W} = -\frac{1}{2n^2}$.

6.2 Stair-step Decay and Overlapping Resonances

In Chapter 2, we demonstrated how the spectral density could be represented as, and in fact thought of as an infinite sum of Lorentzians.

$$|A_\nu|^2 = \left| \frac{\sqrt{\text{Sinh}[\pi \frac{\gamma}{2}]}{\text{Sin}[\pi(\nu + \delta + i \frac{\gamma}{2})]} \right|^2 = \text{Sech}[\pi \frac{\gamma}{2}] \sum_{k=-\infty}^{\infty} \frac{\gamma}{2\pi} \frac{1}{(\nu + \delta - k)^2 + \frac{\gamma^2}{4}} \quad (6.12)$$

For small γ these lorentzians are separate from one another, and their behavior

Further we showed that the ICE cross sections were dominated by those few resonances that "peaked" for ν near n^* . The ICE cross sections were measured in the frequency domain; it would be interesting to see if our time-domain observations of shock-wavepackets can also be well-described by a finite sum of resonances. Thus, we re-write our SWP as

$$\Psi[r, t] \approx \frac{\gamma}{2\pi} \text{Sech}[\pi \frac{\gamma}{2}] \sum_{k \sim n^*} \int d\mathcal{W}_\nu \frac{O[\nu, n^*] \phi_\nu[r]}{(\nu + \delta - k)^2 + \frac{\gamma^2}{4}} e^{-i\mathcal{W}_\nu t}, \quad (6.13)$$

where the exact number of k -values in the region of n^* remains to be determined. In the figures that follow (6.5 and 6.6), we simulate the SWP decay rate for 1, 3, 5 and 7 resonances -- symmetrically distributed about $k \simeq n^*$.

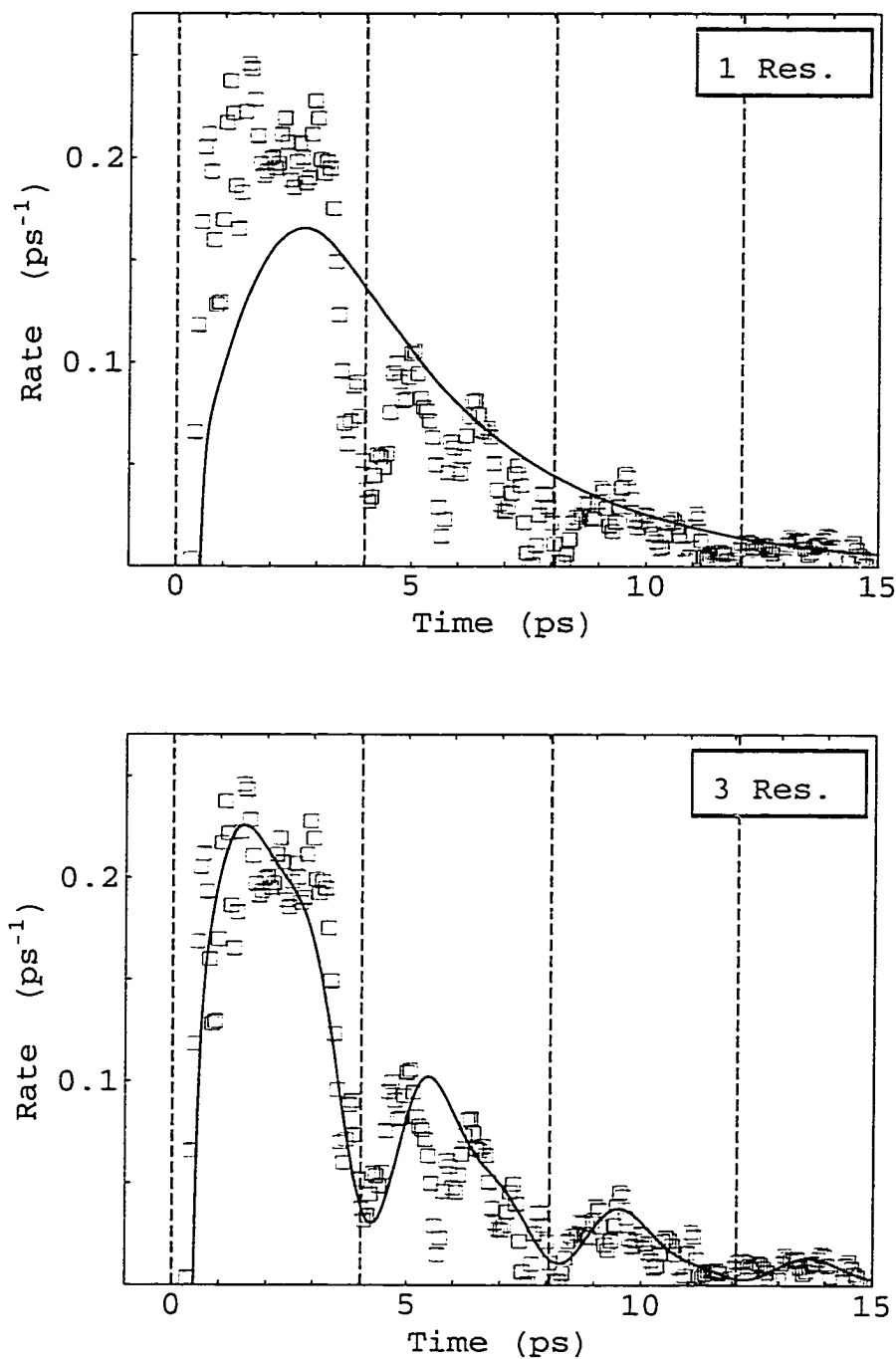


Figure 6.5

Decay Rate of a Shock-wavepacket. Both curves show the results of simulations where the spectral density was given by Equation (6.12). The upper plot results from A_v being represented by a single Lorentzian. For the lower plot, three Lorentzians were used.

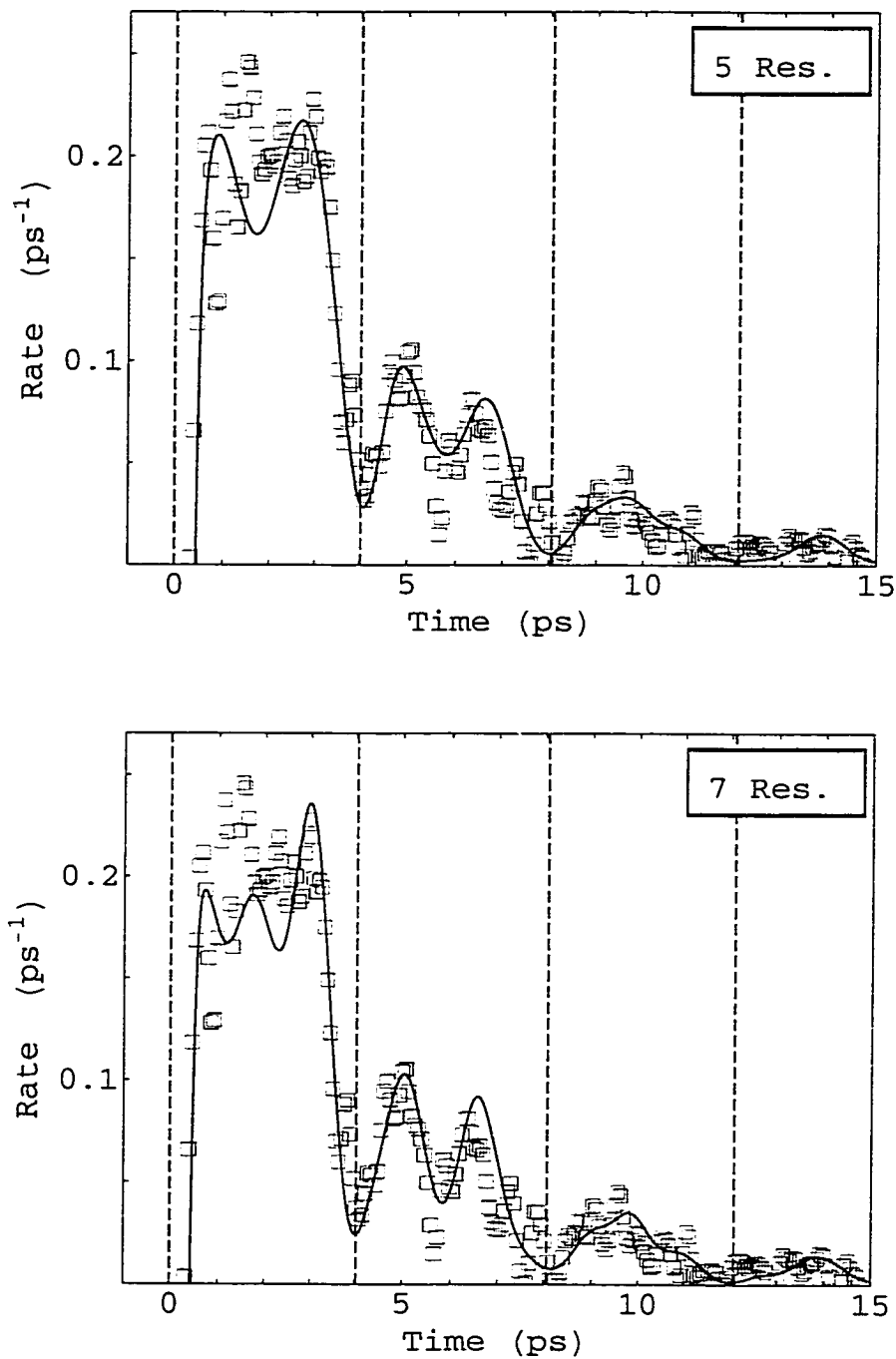


Figure 6.6

Decay Rate of a Shock-wavepacket. Both curves show the results of simulations where the spectral density was given by Equation (6.12). The upper plot results from A_v being represented by a sum of five Lorentzians. For the lower plot, seven Lorentzians were used.

We can gain some insight into these graphs if we think about them qualitatively in terms of Fourier transforms taken in the Large- n limit. Start with the single resonance case, and focus on the Lorentzian form of the resonance. The Fourier transform of a Lorentzian is a decaying exponential. Move on to the three resonance case, where these resonances are evenly spaced. All three resonances will have the same basic Fourier transform, since they have the same functional form. It is straightforward to show that spacing between the resonances results in relative phase shifts in their Fourier Transforms. These phase shifts manifest themselves as the oscillations in the rate. With three resonances, the period of oscillation is equal to the Kepler period. With five resonances, oscillations with periods of half a Kepler period appear. It appears that seven resonances are adequate to model the rate over most of the SWP's lifetime. The biggest error in limiting ourselves to seven resonances occurs in the short time (less than $\frac{1}{2}$ Kepler period) behavior of the rate. In our fits to the rate "data", this region is essentially flat. Just as many high frequency components are required to simulate a square wave, many fast oscillations would be required to produce this flat region, and would therefore require the inclusion of numerous resonances.

The key point though, is that Equations (6.12) and (6.13) allow us to understand the oscillations in the shock-wavepacket decay rate in terms of interference between a finite number of overlapping resonances.

Chapter 7 Conclusions

Starting from a singly excited Rydberg state in Calcium, we have used short-pulse ICE techniques to create and observe Shock-wavepackets. We have used two different time-dependent simulations to describe the dramatic, non-exponential, stair-step decay of these wavepackets. In both formulations, for several different initial Rydberg states, we are consistently able to model the decays in terms of two energy-independent multi-channel quantum defect parameters -- the scaled decay width γ , and the final state series defect δ . These time domain measurements provide a unique insight into the physics of autoionizing Rydberg wavepackets that could not be as easily obtained in the frequency domain.

Experimentally, we have demonstrated the practical use of a novel detection scheme. Using pump-probe short-pulse ICE techniques, we were able to change the time scale of our measurement process from the sub-picosecond range over which the autoionization process unfolds, to the more easily observed nanosecond range determined by the travel time to the detector of the high energy electrons. Such a detection scheme should be useful in monitoring time-dependent changes in

intermediate states of a multi-step excitation. In other words, one could use short-pulse ICEs to map out the dynamics of a quantum control experiment.

At the mention of quantum control, we find that we have come full circle -- returning to the topic which opened the introduction to this dissertation. Along these lines, we'd like to close with a suggestion for a quantum control experiment that follows naturally from the work recorded here.

We propose to initiate the shock-wavepacket from a bound-state Rydberg wavepacket instead of a single eigenstate; in particular a bound-state wavepacket consisting of three adjacent states.

$$\Psi[r, t] = \mathcal{N} (\beta_{n-1} \phi_{n-1}[r] e^{-i\mathcal{W}_{n-1} t} + \beta_n \phi_n[r] e^{-i\mathcal{W}_n t} + \beta_{n+1} \phi_{n+1}[r] e^{-i\mathcal{W}_{n+1} t}), \quad (7.1)$$

(where the β_i determine the relative amplitude for each state, and \mathcal{N} is a normalization constant). Following the "wavepacket approach" of Chapter 6, we see that a shock-wavepacket thus produced is written as a sum of similar terms -- each with a slightly different time-dependence. The beating between these terms should result in stair-steps in the *survival probability* instead of the decay rate.

Experimentally, we could make such a wavepacket if, for example, we replaced the narrow-band dye laser that drives the $4s4p \rightarrow 4snd$

transition with a pulse of doubled light from our ultra-fast laser ($\lambda \approx 393$ nm). This is where the quantum control would come in. Using the doubled ultra-fast light to produce our bound-state wavepacket, would allow us to precisely control the amount of time that passes between the wavepacket's creation, and the initiation of the short-pulse ICE. During this time, the bound-state wave packet would evolve -- presenting a somewhat localized probability distribution that would "orbit" the core at the Kepler period of the central n -state. By picking our time delay judiciously, we can change -- or control -- the time development of the shock-wavepacket. If the ICE is initiated as the wavepacket is near the core, we expect to autoionize the vast majority of the wavepacket. If on the other hand, the ICE is initiated just as the wavepacket is leaving the core, we expect to be able to delay the onset of autoionization for almost a full Kepler period; i.e., until the wavepacket returns to the core again.

We have simulated the evolution of such a multi-state shock-wavepacket starting from an initial state given by

$$\Psi[r, 0] = \mathcal{N}(\phi_{29}[r] + \phi_{30}[r] + \phi_{31}[r]), \quad (7.2)$$

and present the results in Figures (7.1) - Figures (7.4). Time is measured in units of the Kepler period for the $n = 30$ state, ΔT refers to

the delay between the formation of the bound-state wavepacket and the initiation of the ICE pulse, with $t = 0$ corresponding to the ICE onset.

For $\Delta T = 0$, our bound-state wavepacket is still at the core when the ICE pulse starts. Autoionization begins immediately, and then drops off somewhat after $\frac{1}{2}$ a Kepler period as the remnants of the wavepacket have escaped to the outer turning point..

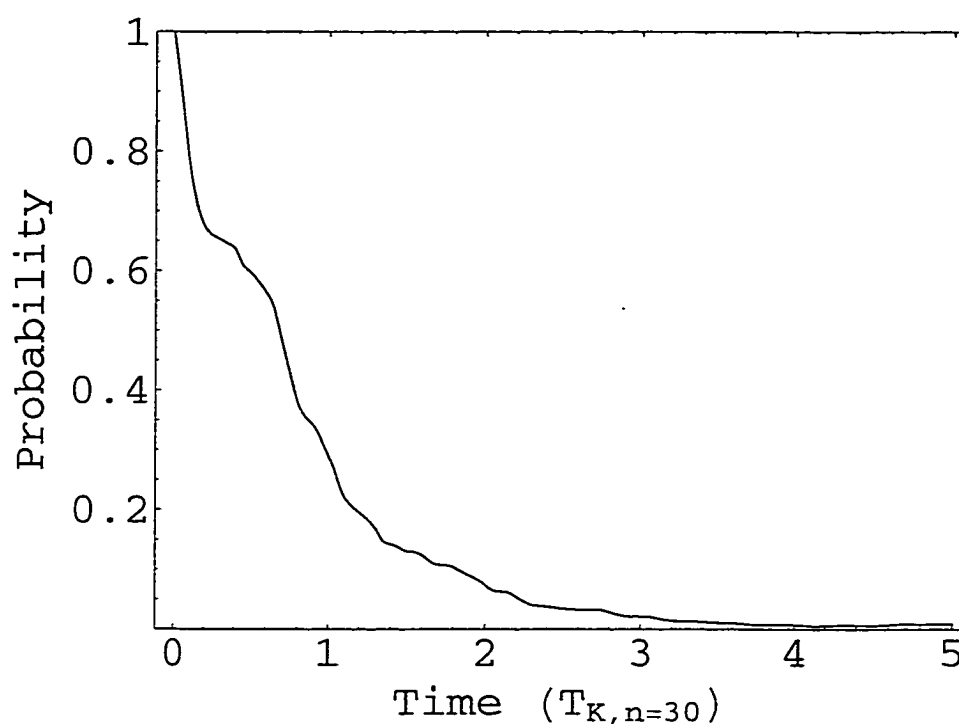


Figure 7.1

Simulated survival probability for a shock-wavepacket initiated from a bound-state wave packet consisting of equal portions of the $n = 29$, 30, and 31 Rydberg eigenfunctions. Time is measure in units of the Kepler period for the $n = 30$ state. The ICE pulse initiates cotemporally with the formation of the bound-state wavepacket.

For $\Delta T = 0.25 T_K$, our bound-state wavepacket is on its way *out* when the ICE pulse starts. The survival probability is similar to the $t = 0$ case, but the autoionization process is delayed for essentially an entire Kepler period.

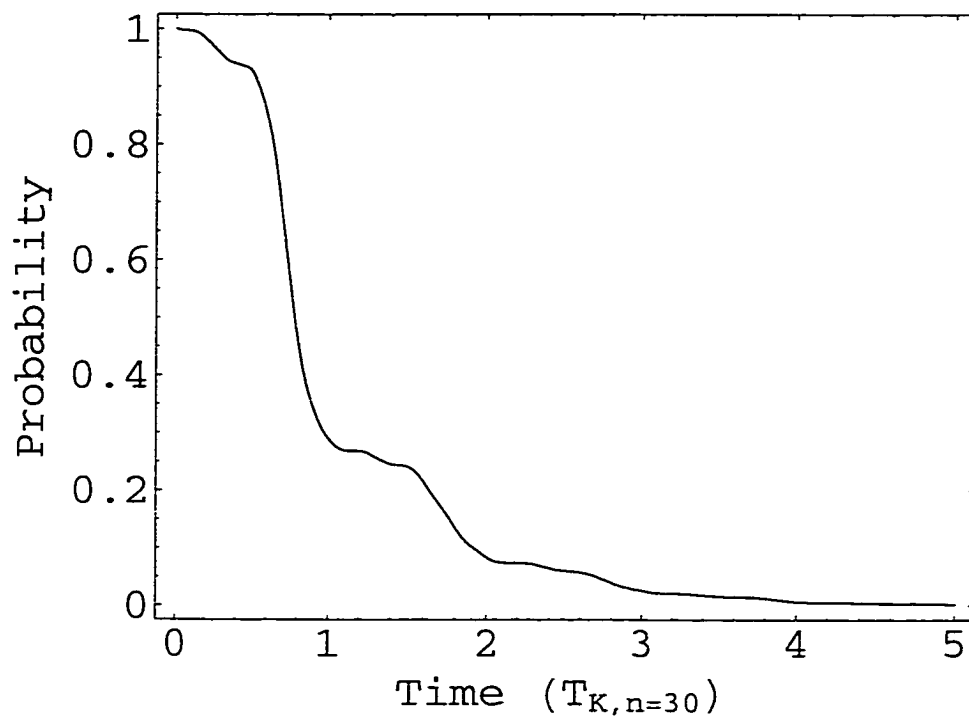


Figure 7.2

Simulated survival probability for a shock-wavepacket initiated from a bound-state wave packet consisting of equal portions of the $n = 29, 30,$ and 31 Rydberg eigenfunctions. Time is measure in units of the Kepler period for the $n = 30$ state. The wavepacket is allowed to evolve for $0.25 T_k$ before the ICE pulse fires.

For $\Delta T = 0.5 T_K$ our bound-state wavepacket is "found" at the outer turning point. Autoionization is delayed for the $\frac{1}{2}$ Kepler period required for the wavepacket to return to the core.

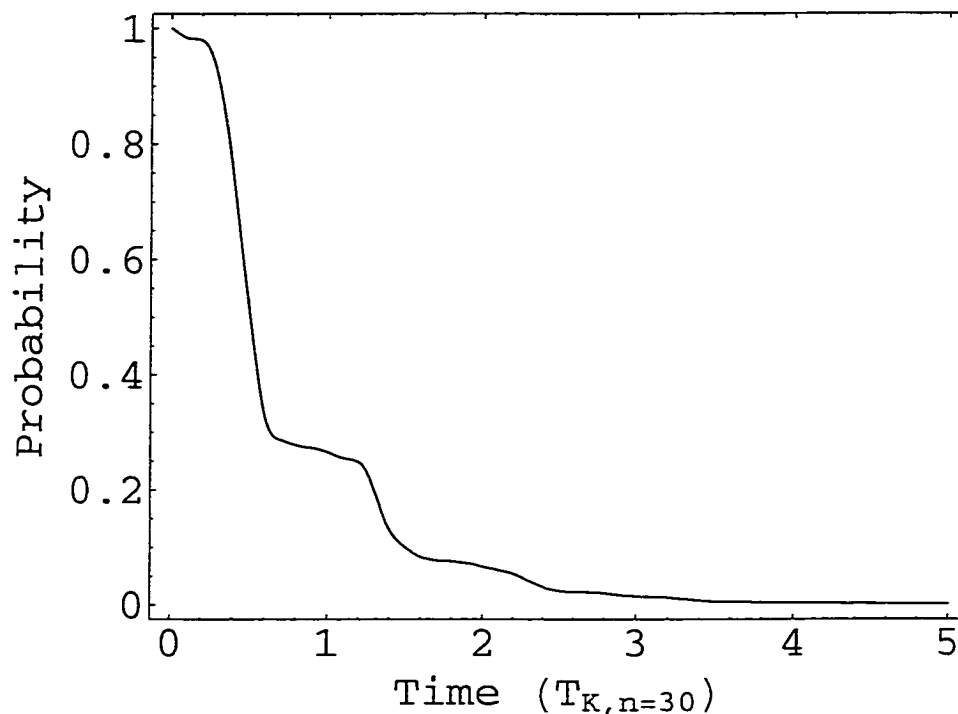


Figure 7.3

Simulated survival probability for a shock-wavepacket initiated from a bound-state wave packet consisting of equal portions of the $n = 29, 30,$ and 31 Rydberg eigenfunctions. Time is measure in units of the Kepler period for the $n = 30$ state. The wavepacket is allowed to evolve for $0.5 T_k$ before the ICE pulse fires.

For $\Delta T = 0.75 T_K$, our bound-state wavepacket is on its way in when the ICE pulse fires. The survival probability is similar to the last two cases, but the autoionization process starts sooner.

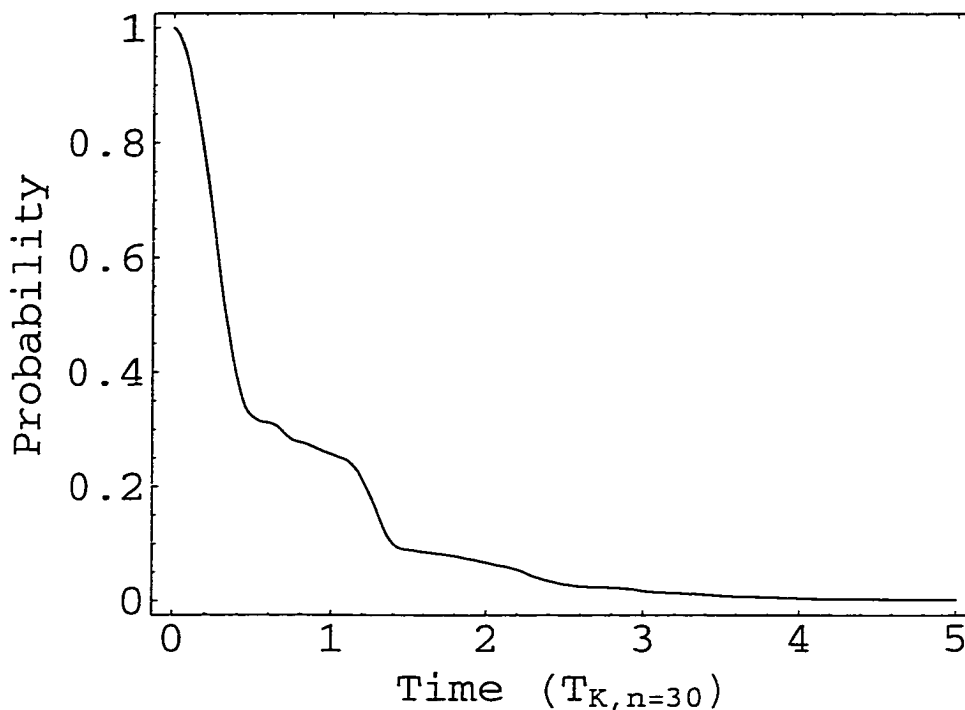


Figure 7.4

Simulated survival probability for a shock-wavepacket initiated from a bound-state wave packet consisting of equal portions of the $n = 29$, 30 , and 31 Rydberg eigenfunctions. Time is measure in units of the Kepler period for the $n = 30$ state. The wavepacket is allowed to evolve for $0.75 T_k$ before the ICE pulse fires.

Having now completed our return to the topic of quantum control, much like the shock-wavepacket in our experiments returned to the core after each orbit; it seems only fitting that we, like the shock-wavepacket should end our work here.

Atomic Units and Appendix 1 the Scaling of the TDSE

The transition from SI units to atomic units is easily made if we focus on the Time Dependent Schrödinger Equation for the hydrogenic atom.

Consider the simple case of a spinless electron in the coulomb potential of an infinitely heavy nucleus with charge $Z e$ -- the idealized hydrogenic atom. The Time Dependent Schrödinger Equation (in SI units) is simply:

$$-\frac{\hbar^2}{2m} \nabla^2 \Psi[\mathbf{x}, t] - \frac{1}{4\pi\epsilon_0} \frac{Z e^2}{|\mathbf{x}|} \Psi[\mathbf{x}, t] = i \hbar \partial_t \Psi[\mathbf{x}, t] . \quad (\text{A1.1})$$

The first step in making the transition to Atomic units is to scale all of our lengths to some appropriate size. Empirically, one finds that almost all measurements of lengths in atomic systems fall within a few orders of magnitude of the Bohr Radius,

$$a_0 \equiv \frac{4\pi\epsilon_0 \hbar^2}{m e^2} = 5.29177249 \times 10^{-11} \text{ Meter}, \quad (\text{A1.2})$$

so this is a natural length-scale to use.

We will thus make the change of variables $\mathbf{x} \rightarrow a_0 \mathbf{r}$.

$$-\frac{\hbar^2}{2 m a_0^2} \nabla^2 \Psi[\mathbf{r}, t] - \frac{1}{4 \pi \epsilon_0} \frac{Z e^2}{a_0 |\mathbf{r}|} \Psi[\mathbf{r}, t] = i \hbar \partial_t \Psi[\mathbf{r}, t] \quad (\text{A1.3})$$

From our definition of the Bohr radius, it is obvious that we can write

$$\frac{1}{4 \pi \epsilon_0} = \frac{\hbar^2}{a_0 m e^2}, \quad (\text{A1.4})$$

so that the Coulomb potential can also be re-written, leading to

$$-\frac{\hbar^2}{2 m a_0^2} \nabla^2 \Psi[\mathbf{r}, t] - \frac{\hbar^2}{m a_0^2} \frac{Z}{|\mathbf{r}|} \Psi[\mathbf{r}, t] = i \hbar \partial_t \Psi[\mathbf{r}, t]. \quad (\text{A1.5})$$

Inspection of Equation (A1.5) presents us with a natural choice for the atomic unit of energy,

$$\begin{aligned} \mathcal{E}_{\text{au}} &\equiv \frac{\hbar^2}{m a_0^2} \\ &= \left(\frac{1}{4 \pi \epsilon_0} \right)^2 \frac{m e^4}{\hbar^2} = \left(\frac{1}{4 \pi \epsilon_0} \frac{e^2}{\hbar c} \right)^2 m c^2 = \alpha^2 m c^2 \\ &= 4.35975 \times 10^{-18} \text{ J} \\ &= 27.2114 \text{ eV} \\ &= 219474.63 \text{ cm}^{-1} \\ &= 2 \text{ Rydberg} \end{aligned} \quad (\text{A1.6})$$

Assume that we can write down a stationary state solution to the TDSE above, i.e. a wave function where the time dependence is given by $e^{-\frac{i}{\hbar} \epsilon t}$. If we proceed to make the replacement $\epsilon \rightarrow E \mathcal{E}_{\text{au}}$, the most natural way to keep time dependence simple, is to simultaneously make the replacement $t \rightarrow t \frac{\hbar}{\mathcal{E}_{\text{au}}}$. Thus, the atomic unit for time is

$$\begin{aligned}\tau_{\text{au}} &\equiv \frac{m a_0^2}{\hbar} = (4 \pi \epsilon_0)^2 \frac{\hbar^3}{m e^4} \\ &= 0.0241888 \text{ fs}\end{aligned}\tag{A1.7}$$

The TDSE now possesses the same constant energy factor in front of each term,

$$\begin{aligned}-\frac{\hbar^2}{2 m a_0^2} \nabla^2 \Psi[\mathbf{r}, t] - \frac{\hbar^2}{m a_0^2} \frac{Z}{|\mathbf{r}|} \Psi[\mathbf{r}, t] = \\ i \frac{\hbar^2}{m a_0^2} \partial_t \Psi[\mathbf{r}, t],\end{aligned}\tag{A1.8}$$

which can be removed to yield

$$-\frac{1}{2} \nabla^2 \Psi[\mathbf{r}, t] - \frac{Z}{|\mathbf{r}|} \Psi[\mathbf{r}, t] = i \partial_t \Psi[\mathbf{r}, t].\tag{A1.9}$$

In our work so far, we have effectively chosen mass to be measure in units of the electron's mass. Units for other quantities of physical have also been implicitly defined by the choices we've already made, for example:

$$\begin{aligned}p &\equiv m v, \\ \Rightarrow p &= m \frac{a_0}{\tau_{\text{au}}} = \frac{\hbar}{a_0} = \frac{m e^2}{4 \pi \epsilon_0 \hbar} = 1.99285 \times 10^{-24} \text{ Kg M/s},\end{aligned}\tag{A1.10}$$

$$\begin{aligned}f &\equiv 1/\tau_{\text{au}} = \frac{\hbar}{m a_0^2} = \frac{1}{(4 \pi \epsilon_0)^2} \frac{m e^4}{\hbar^3} \\ &= 4.13414 \times 10^{16} \text{ Hertz}.\end{aligned}\tag{A1.11}$$

Comparison of our initial and final forms for the TDSE reveal that the electric potential is measured in units of the hydrogenic potential at one Bohr radius,

$$\frac{1}{4\pi\epsilon_0} \frac{e}{a_0} = \frac{\hbar^2}{m e a_0^2} = 27.2114 \text{ V}. \quad (\text{A1.12})$$

The units for the electric field follow simply from this

$$\frac{1}{4\pi\epsilon_0} \frac{e}{a_0^2} = \frac{\hbar^2}{m e a_0^3} = 5.14221 \times 10^9 \text{ V/cm}. \quad (\text{A1.13})$$

The canonical list of Atomic Units is given in [3].

Appendix 2 Rydberg Wavefunctions

A2.1 Numerov Method -- Numerical Wavefunctions

The TISE for the radial Rydberg wavefunctions is given by

$$-\frac{1}{2} \partial_{r,r} u_v[r] + \left(\frac{\ell(\ell+1)}{2r^2} - \frac{1}{r} \right) u_v[r] = -\frac{1}{2\nu^2} u_v[r] \quad (\text{A2.14})$$

We will construct solutions to this equation using the Numerov method.

We rearrange Equation (A2.1) to be

$$\partial_{r,r} u_v[r] = \left(\frac{\ell(\ell+1)}{r^2} - \frac{2}{r} + \frac{1}{\nu^2} \right) u_v[r], \quad (\text{A2.15})$$

so that it has the general Numerov form of [44]

$$\partial_{x,x} Y[x] = g[x] Y[x]. \quad (\text{A2.16})$$

The Numerov approach is based upon the Equation [44]

$$\begin{aligned} (1 - T[x+h]) Y[x+h] + \\ (1 - T[x-h]) Y[x-h] = (2 + 10 T[x]) Y[x] + O[h^6], \end{aligned} \quad (\text{A2.17})$$

where

$$T[x] = \frac{h^2}{12} g[x], \quad (\text{A2.18})$$

and h is the stepsize, or separation between successive $Y[x]$ values to be calculated. Knowing $Y[x]$ at any two of the locations $(x-h, x, x+h)$ allows one to calculate it at the third. Since the error in this method is on the order of h^6 , it is clear that one desires to have h as small as possible, and certainly less than 1. On the other hand, we desire values for our wave function out to several thousand Bohr Radii. The smaller h is, the more points we need to calculate, and the longer it will take to produce a given wavefunction. There is an additional complication as well. Consider the solution of Equation (A2.2) for $\nu = 30$.

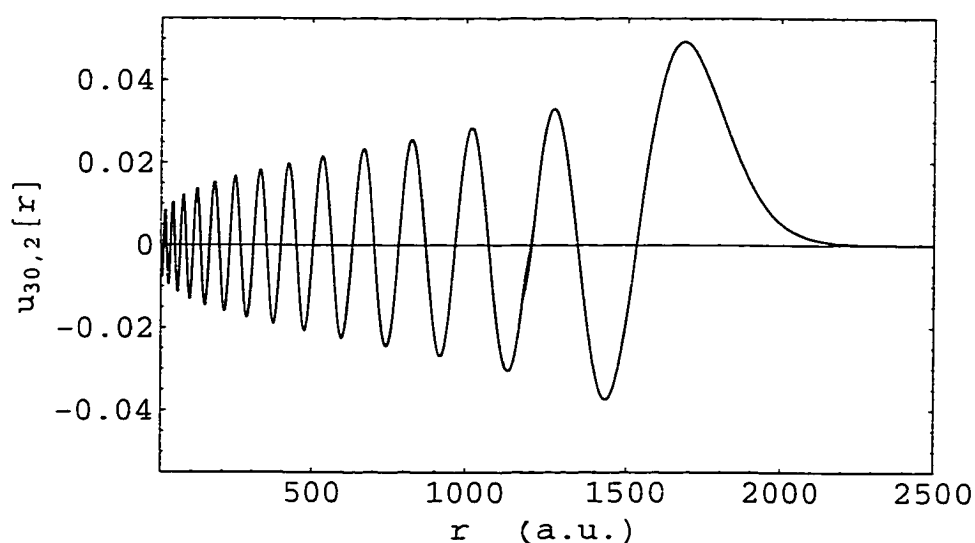


Figure A2.1

Radial wavefunction for hydrogen with $\nu = 30$, $\ell = 2$. The changing wavelength of this solution makes it numerically "inconvenient" to calculate Equation (A2.2) with a fixed step size method. This difficulty exists for all large values of ν .

The wavelength of this bound solution is constantly changing over the whole range of r . A value for h chosen appropriately for the small- r

region, would result in a waste of time in the large- r region by calculating far more points than were required. Conversely, a value of h chosen for economy in the Large- r region would likely lead to errors by over-stepping lobes in the small- r region.

We circumvent these problems by following Bhatti[24], and making the definitions

$$\xi = \sqrt{r}, \quad (\text{A2.19})$$

$$\begin{aligned} u[r] &= r^{1/4} \chi[\sqrt{r}] = \sqrt{\xi} \chi[\xi] \\ \Rightarrow \chi[\xi] &= \frac{u[r]}{r^{1/4}} = \frac{u[\xi^2]}{\sqrt{\xi}} \end{aligned} \quad (\text{A2.20})$$

The TISE is now given by

$$\chi''[\xi] = \left(-8 + \frac{\frac{3}{4} + 4l(1+l)}{\xi^2} + \frac{4\xi^2}{v^2} \right) \chi[\xi] \quad (\text{A2.21})$$

This is still an equation in the Numerov form, but with these changes comes a useful transformation.

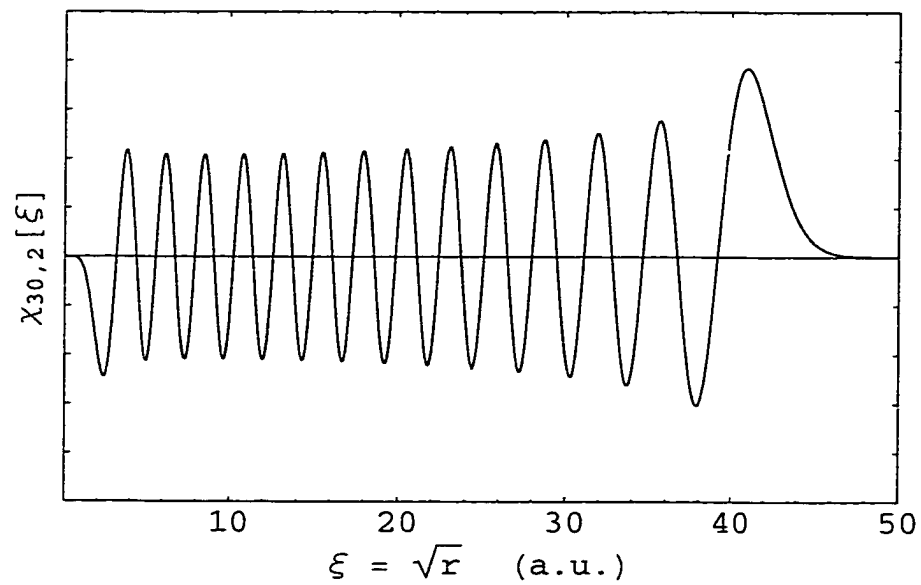


Figure A2.2

Radial wavefunction for hydrogen with $\nu = 30$, $\ell = 2$, in the $\xi = \sqrt{r}$ representation of Bhatti[24]. The function $\chi[\xi]$ is a solution to Equation (A2.8). The almost constant wavelength of bound state solutions in this representation makes it numerically ideal for a fixed step approach.

In ξ -space, the wavelength is essentially constant throughout all space, this means that a single h value can be chosen for the entire range.

A2.1.1 Numerov Routines

Below we present a version of the Numerov Algorithm for calculating bound state wavefunctions implemented in *Mathematica*. We start well beyond the outer turning point (3.5 times further out), and obtain our starting values from those of the nearest hydrogenic radial wavefunction at this point (e.g., if we are to calculate $\chi[\xi]$ for $\nu = 30.2$, we take our starting values from $\chi_{30}[\xi]$). This is completely arbitrary -- our choice was made because of the relative ease with which the hydrogenic functions can be evaluated. In practice, any two numbers on the order of Machine Epsilon, chosen so that $\chi[\xi] > \chi[\xi + h] > 0$ will do. NvStep is the workhorse; given $\{\xi, \chi[x]\}$, it returns $\{\xi - h, \chi[\xi - h]\}$. NvStep is called by Nv until the stopping point has been reached. We found that 60% of the classical inner turning point worked well for a stopping point (i.e. $\xi_{\text{stop}} = \sqrt{0.6 \frac{\ell(\ell+1)}{2}}$). The output is in the form of a *Mathematica* List. In this implementation, we chose to convert $\chi[\xi]$ back to $u[r]$ and return the radial eigenfunction -- very minor changes would be needed to return $\chi[\xi]$ instead. For clarity, the letter h was replaced by the variable StepSize. For simplicity and speed, we have inserted Equation (A2.5) into Equation(A2.4) before encoding.

These routines could easily be modified to calculate continuum functions. Explicit references to the effective principle quantum number would be replaced by appropriate terms involving the energy. The integration scheme would require an additional step. Starting at the origin with initial values drawn from a hydrogenic wavefunction of the same energy, we would first integrate out to a large ξ point at which the coulomb potential can be ignored. Introducing a phase shift of $\pi\delta$ *towards* the origin produces the correct asymptotic wave function from which to draw our starting values for our integration in towards the core. Normalization would be determined by fixing the asymptotic amplitude to be $\sqrt{\frac{\pi}{2k}}$, where k is found from $\mathcal{W} = \frac{k^2}{2}$. [10]

<<NumericalMath`ListIntegrate`

$$c[n_, \ell_, \mathcal{Z}_, x_] := (-1)^{n+1+\ell} x \left(\frac{2\mathcal{Z}}{n}\right)^{3/2} \sqrt{\frac{(n-\ell-1)!}{2n(n+\ell)!}} \left(2\frac{\mathcal{Z}x}{n}\right)^\ell \\ \text{LaguerreL}\left[n-\ell-1, 2\ell+1, 2\frac{\mathcal{Z}x}{n}\right] e^{-\mathcal{Z}x/n}$$

$$g[\xi_, \eta_, \ell_: 2, \mathcal{Z}_: 1] := 8 \left(\frac{\mathcal{Z}^2}{2\eta^2} \xi^2 - \mathcal{Z} + \frac{(\ell + \frac{1}{4})(\ell + \frac{3}{4})}{2\xi^2} \right)$$

```
NvStep[{xi_, Thispsi_}, eta_, ell_: 2, Z_: 1, StepSize_: 2^-9] := Module[{},
  Nextg = g[xi - StepSize, eta, ell, Z];
  Nextpsi = (((1 - StepSize^2/12) Prevg) Prevp - 2 (1 + 5 StepSize^2/12 Thisg) Thispsi) /
    (-1 + StepSize^2/12 Nextg);
  Prevp = Thispsi;
  Prevg = Thisg;
  Thisg = Nextg;
  Return[{xi - StepSize, Nextpsi}]
```

```
Nv[eta_, ell_: 2, Z_: 1, StepSize_: 2^-9] := Module[{Psi, delta, n},
  (* assumes that eta=n-delta, where delta<=0 *)
  xi0 = Sqrt[3.5 eta^2/Z];
  n = Floor[eta];
  delta = eta - n;
  Prevp = c[n, ell, Z, (xi0 + StepSize)^2] / (xi0 + StepSize)^{1/4};
  Prevg = g[xi0 + StepSize, eta, ell, Z];
  Thisg = g[xi0, eta, ell, Z];
  Psi = Reverse[NestList[NvStep[#, eta, ell, Z, StepSize]&,
    {xi0, c[n, ell, Z, xi0^2] / (xi0)^{1/4}}, Floor[xi0/StepSize]];
  Psi = Map[{#[[1]]^2, If[#[[1]] > Sqrt[0.3 ell(ell+1)/Z], #[[2]] * Sqrt[#[[1]], 0.0]}&, Psi];
  Norm = Sqrt[ListIntegrate[Map[{#[[1]], #[[2]]^2}&, Psi];
  Psi = Map[{#[[1]], #[[2]]/Norm}&, Psi];
  Return[Psi]
```

References

- [1] X. Wang and W.E. Cooke, *Phys. Rev. Lett.* **67**, 976 (1991).
- [2] J.C. Slater, *Quantum Theory of Atomic Structure*, vol. II, McGraw-Hill, New York, 1960. Chapter 17.
- [3] H. A. Bethe and E. A. Salpeter, *Quantum Mechanics of One and Two Electron Atoms*, Academic Press, New York, 1975.
- [4] L.D.Landau and E.M.Lifshitz, *Quantum Mechanics : Non-Relativistic Theory*, 3rd Edition, Pergamon Press, New York, 1977, p. 254.
- [5] H. Goldstein, *Classical Mechanics*, Second Edition, Addison-Wesely Publishing Company, Reading, 1980, p. 70.
- [6] Thomas Joseph Bensky, *Classical Rydberg Electron Interactions with Half Cycle Pulses*, Ph.D. Thesis, University of Virginia, 1998.
- [7] George Arfken, *Mathematical Methods for Physicists*. 3rd edition, Academic Press, Boston, 1985, p. 752.
- [8] Leonard I. Schiff, *Quantum Mechanics*, Third Edition, McGraw-Hill, New York, 1968, Chapter 4, Section 14.
- [9] Eugen Merzbacher, *Quantum Mechanics*, Third Edition, John

- Wiley and Sons, 1998, Chapter 12.
- [10] Thomas F. Gallagher, *Rydberg Atoms*, Cambridge University Press, New York, 1994, Chapter 2.
- [11] Leonard I. Schiff, *Quantum Mechanics*, 3rd Edition, McGraw-Hill, New York, 1968, Chapter 4, Section 16.
- [12] Thomas F. Gallagher, *Rydberg Atoms*, Cambridge University Press, New York, 1994, p. 25.
- [13] Thomas F. Gallagher, *Rydberg Atoms*, Cambridge University Press, New York, 1994; and in *Atomic, Molecular, and Optical Physics Handbook*, Edited by G. W. F. Drake, AIP Press, New York, 1996, Chapter 14.
- [14] H. Friedrich, *Theoretical Atomic Physics*, Chapter 2. Springer-Verlag, New York, 1990.
- [15] *Atomic, Molecular, and Optical Physics Handbook*, Edited by G. W. F. Drake, AIP Press, New York, 1996, p. 185.
- [16] Friedrich, *Theoretical Atomic Physics*, Chapter 2. Springer-Verlag, New York, 1990.
- [17] W. E. Cooke, T.F. Gallagher, S. A. Edelstein, and R. M. Hill, *Phys. Rev. Lett.* **40**, 178 (1978).
- [18] R.R. Jones, *Electron Correlation in Double Rydberg Autoionizing States of Barium*, Ph.D. thesis, University of Virginia, p. 23.

- [19] M.J. Seaton, *Rep. Prog. Phys.* **46**, 167 (1983).
- [20] W.E. Cooke and C.L. Cromer, *Phys. Rev. A* **32**, 2725 (1985).
- [21] U. Fano *Phys. Rev. A* **2**, 353 (1970).
- [22] W. Eissner, H. Nussbaumer, H. E. Sarah, and M. J. Seaton, *J. Phys. B* **2**, 341 (1969).
- [23] Thomas F. Gallagher, *Rydberg Atoms*, Cambridge University Press, New York, 1994, p. 418.
- [24] S.A. Bhatti, C.L. Cromer and W.E. Cooke, *Phys. Rev. A* **24**, 161 (1981)
- [25] R. R. Jones, *Phys. Rev. A* **58**, 2608 (1998)
- [26] R. R. Jones, *Phys. Rev. A* **57**, 446 (1998)
- [27] Gentile, Hughey, and Kleppner, *Phys. Rev. A* **42**, 440 (1990).
- [28] X. Wang and W.E. Cooke, *Phys. Rev. A* **46**, 4347 (1992).
- [29] Thomas F. Gallagher, *Rydberg Atoms*, Cambridge University Press, New York, 1994, Chapter 2 and references therein.
- [30] T. W. Hansch, *App. Opt.* **11**, 895 (1972).
- [31] Richard C. Powell in *Atomic, Molecular, and Optical Physics Handbook*, Edited by G. W. F. Drake, AIP Press, New York, 1996, p. 797.
- [32] Coherent Laser Group, *Innova 310/320 Series Ion Laser Operator's Manual*, Santa Clara, 1990.

- [33] Jean-Claude Diels & Wolfgang Rudolph. *Ultrashort Laser Pulse Phenomena: Fundamentals, Techniques, and Applications on a Femtosecond Time Scale*. Academic press. San Diego, 1996, p. 79.
- [34] Richard C. Powell in *Atomic, Molecular, and Optical Physics Handbook*, Edited by G. W. F. Drake, AIP Press, New York, 1996, p. 800.
- [35] Jean-Claude Diels & Wolfgang Rudolph. *Ultrashort Laser Pulse Phenomena: Fundamentals, Techniques, and Applications on a Femtosecond Time Scale*. Academic press. San Diego, 1996, p.212.
- [36] Thomas Joseph Bensky, *Classical Rydberg Electron Interactions with Half Cycle Pulses*, Ph.D. thesis, University of Virginia, 1998.
- [37] Jean-Claude Diels & Wolfgang Rudolph. *Ultrashort Laser Pulse Phenomena: Fundamentals, Techniques, and Applications on a Femtosecond Time Scale*. Academic press. San Diego, 1996, p.336.
- [38] Jean-Claude Diels & Wolfgang Rudolph. *Ultrashort Laser Pulse Phenomena: Fundamentals, Techniques, and Applications on a Femtosecond Time Scale*. Academic press. San Diego, 1996, p.

321.

- [39] Miles V. Klein and Thomas E. Furtak, *Optics*, John Wiley and Sons, New York, 1986, p. 282.
- [40] Murray R. Spiegel, *Schaum's Outline of Theory and Problems of Complex Variables*, McGraw-Hill, Inc., New York, 1993, p. 175.
- [41] Kohler et. al., *Phys. Rev. Lett.* **74**, 3360 (1995), and references 1-8 therein.
- [42] Eugen Merzbacher, *Quantum Mechanics*, 3rd Edition, John Wiley and Sons, 1998, p. 266.
- [43] Jean-Claude Diels & Wolfgang Rudolph. *Ultrashort Laser Pulse Phenomena: Fundamentals, Techniques, and Applications on a Femtosecond Time Scale*. Academic press. San Diego, 1996, p.134.
- [44] Thomas F. Gallagher, *Rydberg Atoms*, Cambridge University Press, New York, 1994, p. 24.
- [45] William H. Press , Saul A. Teukolsky, William T. Vetterling, Brian P. Flannery, *Numerical Recipes in C: The Art of Scientific Computing*, 2nd Edition, Cambridge University Press, New York, 1995, p. 690.
- [46] J. G. Story, D. I. Duncan, and T. F. Gallagher *Phys. Rev. Lett.* **71**,3431 (1993).